SAND77-2042
Unlimited Release
NRC-3

Exploratory Study of Molten Core Material/Concrete Interactions July 1975 - March 1977

POOR ORIGINAL

Dana A. Powers, Dirk A. Dahlgren, James F. Muir, Walter D. Murfin

Sandia Laboratories

SF 2900 Q(7-73)

1570 096

7912140 . 499

1570 097

EXPLORATORY STUDY OF MOLTEN CORE MATERIAL/CONCRETE INTERACTIONS JULY 1975 - MARCH 1977

Dana A. Powers
Chemical Metallurgy Division 5831

Dirk A. Dahlgren
James F. Muir
Walter D. Murfin*
Reactor Safety Studies Division 5411

Sandia Laboratories
Albuquerque, New Mexico 87115

ABSTRACT

An experimental study of the interaction between high-temperature molten materials and structural concrete is described. The experimental efforts focused on the interaction of melts of reactor core materials weighing 12 to 200 kg at temperatures of 2800 to 1700°C with calcareous and basaltic concrete representative of that found in existing light-water nuclear reactors. Observations concerning the rate and mode of melt penetration into concrete, the nature and generation rate of gases liberated during the interaction, and heat transfer from the melt to the concrete are described. Concrete erosion is shown to be primarily a melting process with little contribution from mechanical spallation. Water and carbon dioxide thermally released from the concrete are extensively reduced to hydrogen and carbon monoxide. Heat transfer from the melt to the concrete is shown to be dependent on gas generation rate and crucible geometry. Interpretation of results from the interaction experiments is supported by separate studies of the thermal decomposition of concretes, response of bulk concrete to intense heat fluxes (28-280 W/cm^2), and heat transfer from molten materials to decomposing solids.

The experimental results are compared to assumptions made in previous analytic studies of core meltdown accidents in light-water nuclear reactors.

A preliminary computer code, INTER, which models and extrapolates results of the experimental program is described. The code allows estimation of the effect of physical parameters on the nature of the melt/concrete interaction.

---

*Presently located in Karlsruhe, F.R.G., Germany, as US NRC Resident Scientist.

CONTENTS

ILLUSTRATIONS

TABLES

EXPLORATORY STUDY OF MOLTEN CORE MATERIAL/CONCRETE
INTERACTIONS JULY 1975 - MARCH 1977

Introduction

The extremely high standards maintained in the design, construction, and operation of nuclear power reactors has minimized the probability of core meltdown accidents. Nevertheless, to assess the public risk associated with reactor operation, a realistic evaluation of postulated core meltdown accident sequences is required. This was highlighted by the Reactor Safety Study,[1] which found that core meltdown accidents were the dominant contributors to the risk. This provides motivation for further investigation of physical phenomena that may influence the consequences of postulated core meltdown accident sequences.

The accident sequences developed by the Reactor Safety Study for light water reactors indicated that the interaction of molten core materials with concrete was important because it affects two primary modes of release of radioactive materials from the containment building. The overpressurization release occurs when the containment atmospheric pressure is increased to containment failure pressure by the added heat and water vapor during blowdown plus additional heat from fission product decay. This release mode can be directly affected by the gas release and heat flow from the melt/concrete interaction. The molten core materials interacting with the concrete base produces an erosion of the concrete which can lead to fission product release to the soil. The detailed phenomena of the melt/concrete interaction determine if and how fast this release mode can occur. For both release types, the interaction affects the radioactive release source term.

To investigate the experimental basis of fuel-melt accident analyses, a comprehensive review[2] was performed at Sandia Laboratories from September 1974 to early 1975. The results of that study indicated the data base concerning the core/concrete interaction was sparse. The phenomenological uncertainties identified include the possibility of spall-dominated erosion and the magnitude, time dependence and direction of the erosion. Uncertainties in the behavior of concrete under severe thermal attack included the melting characteristics, the temperature dependence of concrete decomposition, the identification of released gas species, and the heat transfer and mass transfer of gases and water within concrete. The flow of CO_2 and H_2O through the melt upon leaving the concrete were not well-known. The effect of this gas flow on the energy partioning in the melt was unknown as was the effect of melt reduction of the gases to CO and H_2. Depending on the temperature, mixing, and species present, the gas leaving the melt could include H_2O, H_2, CO_2, CO, CH_4, C_2H_4, C_2H_6, C, etc, some of which could affect containment integrity through burning or explosivity. The heat flux partition can be affected by crust formation, layering phenomena, solubilities, and interface vapor blanketing as well as gas flow. Gas flowing through the melt could also affect the fission product release and aerosol generation from the melt.

7

Under the sponsorship of the Reactor Safety Research Division of the United States Nuclear Regulatory Commission, a program titled Molten Core-Concrete Interactions Study[3] was initiated in July 1975 to investigate phenomena associated with the interaction of molten core materials with structural concrete. The program was primarily a qualitative, scoping study of the macroscopic phenomena involved in these interactions. Attempts were also made to identify the important physical and chemical processes influential in the material interactions, and to quantify the phenomena where possible and required. The longer term objectives include making improved measurements of the dominant phenomena and providing an adequate interaction model for use in the risk assessment.

The emphasis of the experimental program was placed on the observation of the generation of gases, penetration of melt into the concrete, nature of generated gases, aerosols and fission product, removal, and heat flux partitioning.

The program was divided into five components:

1. Simulant experiments of melt/concrete interface phenomena

2. Concrete thermal decomposition analysis (Appendix A)

3. Prototypic melt-concrete interactions (Appendices B and C)

4. Response of bulk concrete to heat flux on one surface (Appendix D)

5. Analysis and model development (Appendix E).

These components are described in detail in the indicated appendices.

The focus of the experimental effort was on tests in which prototypic core melt constituents were brought into contact with concrete representative of that found in existing light-water reactors. The experimental techniques emphasized relatively large-scale experiments with appropriate instrumentation. The melt temperatures were as prototypic as possible, ranging from $1700^{\circ}C$ to $2800^{\circ}C$. The behaviors of concretes made with basaltic and calcareous aggregates were compared throughout the experimental program.

Interpretations of the results from the prototypic experiments were supported by investigations of the simulated melt/concrete interface, the thermochemistry of concrete, and the response of bulk concrete to heat fluxes of magnitudes expected in a hypothetical fuel-melt accident. The interface studies were intended to provide some preliminary data concerning the nature of the interface between a melt and a decomposing solid. Simulant materials were used so information could be obtained in a short time using visual techniques. The concrete thermal decomposition studies produced a description of the stoichiometry and rate of gas release from concrete as a function of temperature and heating rate. The heat flux experiments defined the mode and rate of erosion as well as the bulk thermal behavior of concrete.

8

The final element of the program was analysis and modeling of the melt/concrete interaction. The short-term objective was to utilize the experimental data obtained to produce a preliminary model for use in sensitivity studies. The model was also to be used in developing a rational basis for future experimental tasks.

The expected application of the results of this program are in establishing:

- The contribution of the melt/concrete interaction to containment pressurization.

- The composition of the containment atmosphere.

- The rate of removal of nonvolatile fission products from the melt by sparging and aerosol effects on the fission product release source term.

- Heat and mass transfer mechanisms in the concrete and the melt.

- The penetration of the concrete by the core melt.

Results of Study

Results from the diverse elements of the Molten Core -Concrete Interactions Study are drawn together below in a brief description of the behavior of molten, reactor core materials in contact with structural concrete. The series of large-scale tests in which 200-kg steel melts were teemed onto concrete proved to be the most useful source of data concerning the qualitative nature of the melt/concrete interaction. The size and relative nonviolence of these tests made phenomena pertinent to nuclear reactor safety questions easily observed and readily recorded photographically. Simulant tests, thermal analysis of concrete decomposition reactions, and exposure of bulk concrete to intense heat fluxes yielded quantitative data of aid in deciphering the complexities in phenomena observed during the large-scale tests. Small-scale tests extended the range of phenomenological observations to temperature ranges perhaps more typical of those expected in a hypothetical reactor core-meltdown accident. Detailed descriptions of both the experimental methods and results are to be found in the appendices to this document and in progress, topical, and other reports generated during the course of this study (see following listing).

SUMMARY OF MOLTEN CORE MATERIAL
CONCRETE INTERACTION PUBLICATIONS

1. D. A. Powers, Molten Core/Concrete Interactions Project Description, 189 No. A-1019, Sandia Laboratories, 1975.

2. Nuclear Fuel Cycle Safety Research Department, Light Water Reactor Safety Research Program Quarterly Report - July-September 1975, SAND75-0632, Sandia Laboratories, Albuquerque, NM, Dec 1975.

3. Nuclear Fuel Cycle Safety Research Department, Light Water Reactor Safety Research Program Quarterly Report - October-December 1975, SAND76-0163, Sandia Laboratories, Albuquerque, NM, April 1976.

4. D. W. Larson and D. O. Lee, Fluid-Mechanic/Thermal Interaction of a Molten Material and a Decomposing Solid, SAND76-0240, Sandia Laboratories, Albuquerque, NM, Dec 1976.

5. Nuclear Fuel Cycle Safety Research Department, Light Water Reactor Safety Research Program Quarterly Report - January-March 1976, SAND76-0369, Sandia Laboratories, Albuquerque, NM, Sept 1976.

6. H. J. Sutherland and L. A. Kent, Acoustic Wave Velocity Measurements in Curing Reactor-Grade Concrete, SAND76-0416, Sandia Laboratories, Albuquerque, NM, Sept 1976.

7. A. J. Mulac and R. A. Hill, Visible Emission Spectra of Ablating Concrete, SAND76-0565, Sandia Laboratories, Albuquerque, NM, Sept 1976.

8. D. A. Dahlgren, D. A. Powers, J. F. Muir, and B. M. Butcher, "Experimental Results of the Interaction of Molten Core Materials with Concrete," Proceedings of Specialist Meeting on The Behavior of Water Reactor Fuel Elements under Accident Conditions (Spating, Norway, Sept 1976), CSNI Report No. 13, March 1977.

9. J. F. Muir, D. A. Powers, D. A. Dahlgren, "Studies on Molten Fuel/Concrete Interactions," Proceedings of the International Conference on Fast Reactor Safety and Related Physics (Chicago, Oct 1976), CONF-761001, Volume IV, Aug 1977.

10. H. J. Sutherland, G. A. Carlson and L. A. Kent, "Acoustic Diagnostic Techniques for Post-Accident Heat Removal Experiments," Proceedings of the Interntational Conference on Fast Reactor Safety & Related Physics, (Chicago, Oct 1976), CONF-761001, Volume IV, Aug 1977.

11. H. J. Sutherland and L. A. Kent, "Erosion Rate Measurements Using an Acoustic Technique," Review of Scientific Instruments, 48, 110, Aug 1977.

12. Nuclear Fuel Cycle Safety Research Department, Light Water Reactor Safety Research Program Quarterly Report - April-June, 1976, SAND76-0677, Sandia Laboratories, Albuquerque, NM, Feb 1977.

13. Nuclear Fuel Cycle Safety Research Department, Light Water Reactor Safety Research Program Quarterly Report - July-September, 1976, SAND77-0214, Sandia Laboratories, Albuquerque, NM, March 1977.

14. Nuclear Fuel Cycle Safety Research Department, Light Water Reactor Safety Research Program Quarterly Report - October-December, 1976, SAND77-0944, Sandia Laboratories, Albuquerque, NM, July 1977

15. W. B. Murfin, A Preliminary Model for Core/Concrete Interactions, SAND77-0370, Sandia Laboratories, Albuquerque, NM, Aug 1977.

16. D. A. Powers, "Empirical Models for the Thermal Decomposition of Concrete," Trans. Am. Nucl. Soc., 26, 400 (1977).

17. D. A. Powers, "Large-Scale Melt/Concrete Interactions Tests," Trans. Am. Nucl. Soc., 26, 400 (1977).

18. J. F. Muir, "Response of Concrete to High Heat Fluxes," Trans. Am. Nucl. Soc., 26, 399 (1977).

19. K. L. Goin, 2-MW Plasmajet Facility Thermal Tests of Concrete, SAND77-0952, Sandia Laboratories, Albuquerque, NM, July 1977.

20. D. A. Dahlgren, L. D. Buxton, J. F. Muir, W. B. Murfin, L. S. Nelson, and D. A. Powers, "Molten LWR Core Material Interactions with Water and with Concrete," Proceedings of the Topical Meeting on Thermal Reactor Safety (Sun Valley, ID, July-August, 1977).

Qualitative, experimental results are summarized in Table I. This summary is cast as a comparison between experimental observation and assumptions concerning the melt/concrete interactions made in previous analytic studies as embodied by the Reactor Safety Study.[1] This comparison demonstrates where experimental data are now available to confirm, refute, and expand upon these previous assumptions. Qualitative data in the table apply equally well to melt interactions with either basaltic or calcareous aggregate concretes. Responses of the two types of concrete used throughout the experimental studies described here differed only in some of their quantitative features.

The large-scale tests began with contact between a high-temperature melt and concrete which initiated an interaction marked by gas evolution, flames, melt ejection, concrete erosion, and aerosol formation. The intensity of phenomena generated by the melt/concrete interaction increased with the temperature of the melt. Melt temperatures were not controlled in either the large- or small-scale experiments. Once in contact with the concrete, the melts were allowed to naturally cool without the application of additional heat from external sources.

The melt in contact with concrete underwent immediate and extensive evolution. Density differences between the metallic melt ($\rho = 6$-7 g/cm^3) and molten oxides produced from either decomposed concrete or aluminum oxide and decomposed concrete ($\rho = 2.5$-3.2 g/cm^3) caused the melt to rapidly stratify into two distinct layers. The large density difference between oxide and metallic melts kept this stratification rather strictly enforced throughout the test. The oxide and metallic melts behaved quite differently in the tests. In situations where the oxide and metal have more nearly equal densities, the stratification might not be so stable nor so permanent.

TABLE I

Qualitative Data from Experimental Program Compared with
Assumptions in the Reactor Safety Study (1)

Phenomenon	Assumption	Experimental Observation
A. Melt Behavior		
1. Stratification	No	Two distinct melt layers.
2. Agitation	Natural convection	Gas-induced forced convection.
3. Surface crust formation	Yes	Only on the surface of oxide melt.
4. Precipitation	Yes	Only in metal; not observed in oxide melt.
B. Concrete Thermal Penetration		
1. Spallation	Significant first 1 m	Not significant; only to 3-5 mm.
2. Erosion rate	180 cm/hr at steady state	Depends on heat flux or melt temperature; 25 to 135 cm/hr.
3. Directional dependence	Two models: $\frac{h*}{d} < 1$ and $\frac{h*}{d} = 1$	$h*/d < 1$.
4. Heat disposition	All into concrete	Depends on gas generation rate, 21 to 32% into concrete.
5. Reinforcing steel	No significant effect	No significant effect.
C. Concrete Thermal Behavior		
1. Melting	$2200^{\circ}C$ melting point	Melting range $1100\text{-}1400^{\circ}C$.
2. Decomposition	Thermodynamic: dehydration at $500^{\circ}C$; decarboxylation, $770\text{-}890^{\circ}C$	Kinetic-dependent on both temperature and heating rate; dehydration, $25\text{-}500^{\circ}C$; decarboxylation, $550\text{-}1000^{\circ}C$.
D. Gas Production		
1. CO_2 and H_2O	Composition and amount proportional to concrete eroded	Neither composition nor amount proportional to concrete erosion depends on heat transfer in concrete.
2. CO and H_2	No; gases by-pass melt	Yes; gases extensively reduced as they percolate through the melt.
3. Hydrocarbons	No	Hydrogenation of CO produces methane, ethene, etc.
4. Gas ignition	No; flammability limits for well-mixed gases	Yes; diffusional limits seem applicable.
E. Aerosol generation	Yes	Yes; significant particle size, $< 10\mu$.
F. Concrete cracking	No	Thermally induced tensile stresses cause extensive cracking. No melt penetration of the cracks observed.

*h/d = horizontal/downward

The molten metal was quite fluid and, until solidification was complete, presented no significant barrier to gases produced in the test. Simulation experiments have shown that a crust can form between a decomposing solid and a melt which does form a barrier to evolved gases.[4] The criterion for formation of this crust, expressed by the equation

$$\frac{T_I - T_s}{T_L - T_I} = \left[\frac{(K\rho c)_L}{(K\rho c)_s}\right]^{1/2}$$

where

T = temperature (K)

K = thermal conductivity

ρ = density

c = heat capacity

L, s, I = liquid, solid, and interface, respectively.

is not satisfied by the steel melt/concrete system. The gases readily percolated through the melts, which caused them to be vigorously agitated. This gas-induced agitation completely obscured effects of natural convection or forced convection brought about by liquid or solid migration in the melt. As a first approximation, the metallic melt could be considered an isothermal mass with sharp thermal gradients at its perimeters.

Oxide melts were more viscous and less thermally conductive than the metallic melts. Exposed surfaces of the oxide cooled rapidly and formed a relatively hard crust, while the interior of the melt remained fluid. The oxide melt therefore presented some barrier to the escape of gas. Preferred, gas-escape pathways often developed. The oxide melt was not well stirred by the gas.

Solidification of the metallic melts was marked by a sharp drop in the melt cooling rates when temperatures reached the liquidus boundary and the heat of solidification began to compensate for other heat losses from the system. Rapid cooling resumed once solidification was complete. The oxide melts, on the other hand, were glassy and could not be characterized by a solidification temperature or temperature range. Cooling in these phases was smooth and marked only by the increasing viscosities of the melt rather than precipitation of solids.

Concrete erosion was primarily caused by metallic portions of the melt. The superior heat transfer from metal to concrete dominated the affects of wetting and dissolution which would be expected to contribute to concrete erosion by oxide melts. Solid decomposition products of concrete are quite insoluble in the metallic melt and are not wetted effectively by the melt. Erosion by the metal is then strictly a heat-transfer phenomenon which could take the form of spallation or melting. Spallation was found to be an insignificant aspect of erosion that occurred only at the surface of 3 to 5 mm of virgin, formed concrete. Erosion below this surface material erosion was caused by melting.

Melting in concrete is a complex process, occurring over a range of temperatures as would befit the heterogeneous nature of the material. The concrete types used in the study began to melt at about $1100 \pm 20^{\circ}$C within their cementitious phases. Complete liquefaction occurred at temperatures of about $1400 \pm 50^{\circ}$C, depending on the precise chemical makeup of the concrete. The product of melting was a light-green glass.

Quantification of the dependence of erosion rate on heat flux was obtained by exposing concrete samples to nominal heat fluxes of 28 to 280 W/cm^2 provided by plasmajet or radiant sources (see Appendix D). The heat flux necessary to initiate melt erosion of concrete was found to be 10 to 50 W/cm^2. At each given heat flux, erosion was marked by a brief initial transient period followed by a constant movement of the concrete interface as shown in Figure 1. Tests at various applied heat fluxes showed that the rate of erosion was approximately linearly dependent on the heat flux actually deposited in the concrete. As shown in Figure 2, variables such as aggregate size, aggregate type, heat source, or the presence of reinforcing steel had little influence on the erosion, within the uncertainties of the tests.
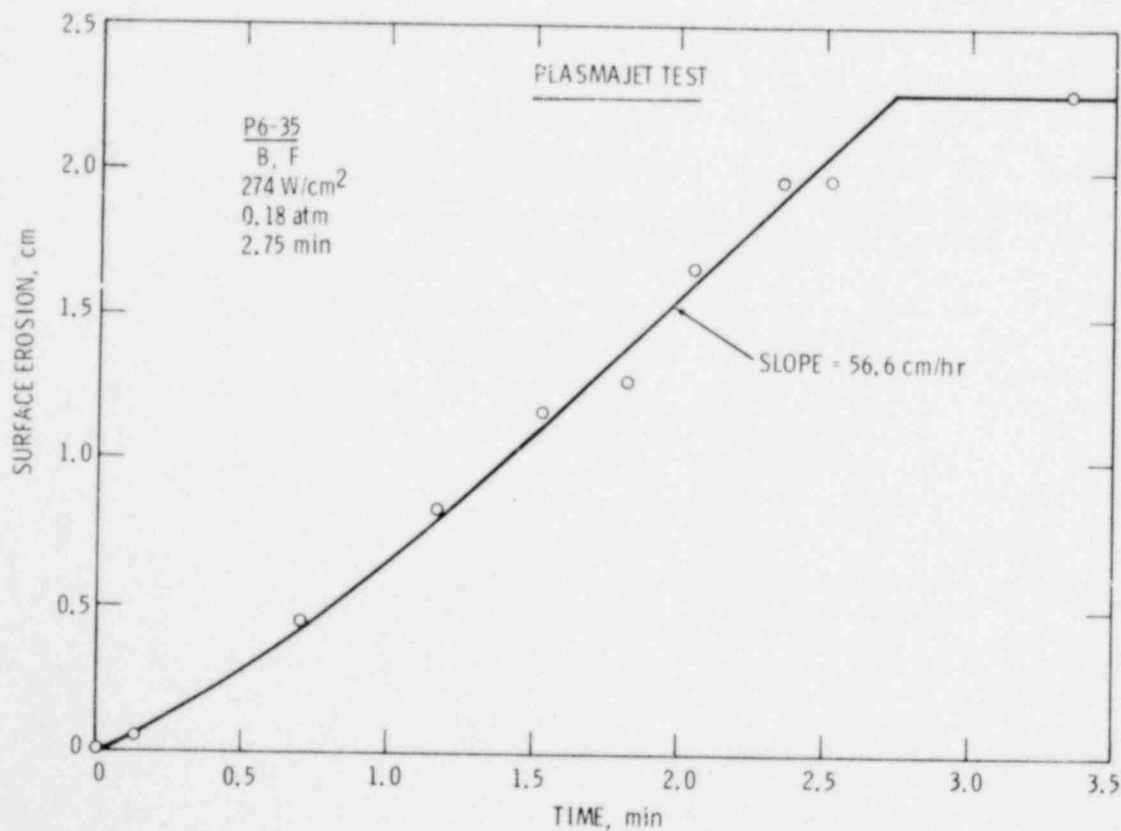

Figure 1. Erosion of Concrete vs Time When Exposed to an Intense Heat Flux
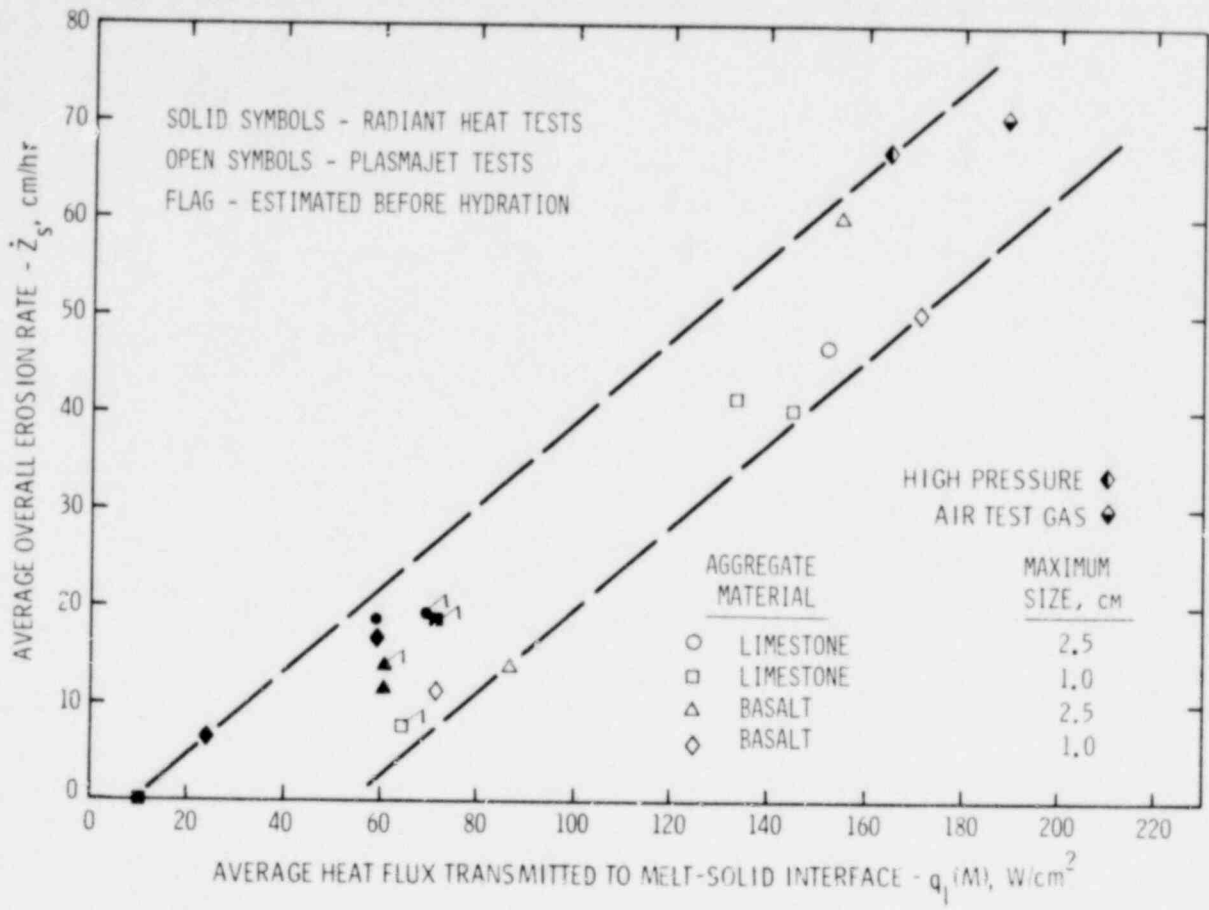
14

Figure 2. Overall Erosion Rate vs Net Heat Flux to Melting Concrete

Erosion rates observed in tests of the melt/concrete interaction were decidedly dependent on melt temperature. They varied between 25 ± 15 cm/hr in the large-scale tests with melts initially at 1700°C and 130 ± 50 cm/hr in small-scale tests with melts initially at temperatures near 2800°C. No significant variation in erosion rate with concrete type could be detected. The extent of erosion was dependent on aggregate type. The volume of concrete eroded in tests with basaltic crucibles was about 1.8 times the volume eroded when calcareous concrete was exposed to the melt.

The relative independence of the erosion rate of aggregate type observed in both the heat flux tests and the melt/concrete tests may be rationalized if it is asserted that the erosion rate is controlled by melting in the cementituous phases of the concrete. These phases were nearly identical in the two concretes, and thermal analysis of concrete melting has been explained in terms of melting beginning in these phases. The overall extent of erosion in the transient tests is, of course, controlled by the thermodynamics of the eroding material and heat transfer effects.

Among heat transfer phenomena which influence melt erosion of concrete are those caused by gases thermally liberated from the concrete. Simulant tests have shown that gases generated at the interface between a melt and a decomposing solid can impede heat transfer. The most

efficient heat transfer in such a system develops when the liquid is in intimate contact with the solid. The imposition of a gas bubble between these two phases causes a sharp reduction in the local heat transfer. It is believed that a combination of this gas shielding of the concrete from the melt and circulation in the melt by gases escaping through it led to the nonuniform concrete erosion observed in the tests. The observed horizontal to downward erosion ratios of 0.9 to 0.4 are consistent with enhanced gas shielding of the cavity sidewalls.

Gas shielding also has an effect on the absolute magnitude of concrete erosion by inhibiting heat transfer from the melt into the concrete relative to upward heat transfer. Ratios of the heat flux into the concrete to upward heat flux were 0.2 and 0.3 for calcareous and basaltic concretes, respectively. Basaltic and calcareous concretes contain nearly equal amounts of water, but calcareous concrete contains an additional source of gas in the form of its aggregate. Trends in the heat-flux ratios for the two concretes paralleled; then, the gas generation rates were as expected when the concretes were heated. The heat flux ratios increased and converged in tests with partially dehydrated and decarboxylated concrete in which gas generation was less extensive.

Gases produced during the tests came from the thermally induced decomposition of concrete. Concrete, regardless of type, undergoes decomposition reactions yielding volatile products in three temperature ranges. Evaporable water amounting to 2.3 to 3 weight percent of the concrete is lost over the temperature range of 30 to 250°C. Chemically constituted water which makes up 1.5 to 2.0 weight percent of the concrete is lost between 380 and 500°C. Both loss of evaporable water and loss of chemically constituted water are the result of decomposing species in the cementituous phases of the concrete. The quantitative and qualitative features of these reactions are quite similar in calcareous and basaltic aggregate concrete. The final decomposition reaction of concrete is decarboxylation of both cementituous species and concrete aggregate. This reaction, which becomes significant at temperatures as low as 550°C, involves a weight loss of about 23 weight percent in the case of calcareous concrete but only about 1 weight percent in the case of basaltic concrete.

Kinetic investigations of these reactions have shown that the dehydration processes can be described in terms of first-order activated transformations. The reversible decarboxylation reaction can be described by a 2/3-order model of the form

$$\frac{d\alpha}{dt} = K_o \exp(-E/RT)(1 - \alpha)^{2/3} \left(1 - \frac{P_{CO_2}}{P_{eg}}\right) ,$$

where

α = fractional loss of carbon dioxide

t = time

T = absolute temperature

K_0, E = kinetic parameters.

16

P_{CO_2} = partial pressure of CO_2, atm

P_{eg} = 1.84×10^7 exp($-39000/RT$) atm

Parameters derived for the decomposition reactions are listed in Table II. A comparison between calculated weight losses based on the above model of first order and 2/3 order reactions and experimentally observed weight losses in heated calcareous concrete is shown in Figure 3.

TABLE II

First Order Rate Constants for Weight-Loss Events in Concrete and Cement Paste

Reaction	Parameters[*]		
	k_o(min^{-1})	E(Kcal/mole)	R[**]
Basaltic Concrete			
a. Evaporable water loss	$(6.8 \pm 3.5) \times 10^8$	12.4 ± 1.5	0.9317
b. Chemically bound water loss -I $(Ca(OH)_2)$ -II	$(2.8 \pm 0.9) \times 10^{11}$	38.4 ± 5.3	0.9317
c. Decarboxylation	$(8.7 \pm 7.5) \times 10^5$	44.0 ± 6.9	0.9745
Calcareous Concrete			
a. Evaporable water loss	$(7.2 \pm 4.2) \times 10^9$	11.0 ± 1.7	0.9241
b. Chemically bound water loss	$(4.0 \pm 0.3) \times 10^{16}$	40.8 ± 1.1	0.9879
c. Decarboxylation	$(3.8 \pm 2.2) \times 10^{11}$	38.5 ± 7.5	0.9763
Cement Paste			
a. Evaporable water loss	$(5.8 \pm 3.1) \times 10^6$	12.3 ± 1.4	0.9680
b. Chemically bound water loss - I	$(2.7 \pm 1.5) \times 10^8$	26.4 ± 4.6	0.9514
c. Chemically bound water loss - II $Ca(OH)_2$	$(3.9 \pm 0.5) \times 10^9$	33.5 ± 3.6	0.9729

[*] Errors are standard deviations of parameters derived from linear fit.

[**] R is the linear correlation coefficient of plots of $\ln \beta/T_M^2$ vs $1/T_M$ where β is the heating rate.
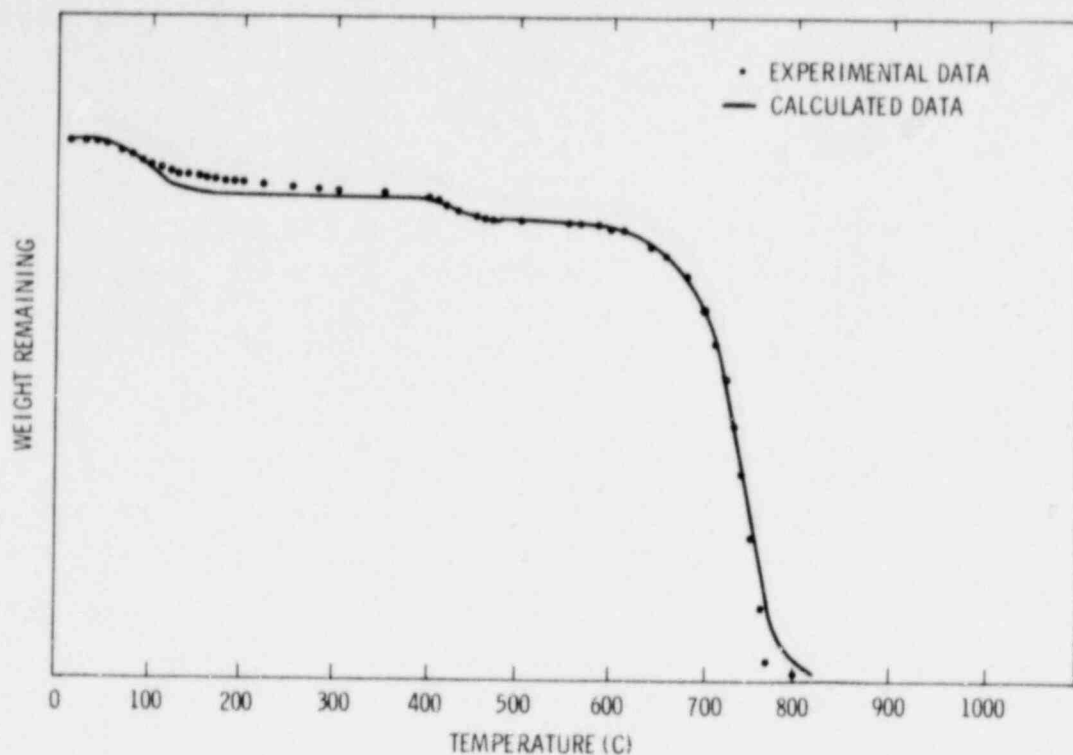
Figure 3. Comparison of Thermogravimetric Data with
Calculated Results

As water and carbon dioxide generated by the thermal decomposition of concrete pass up through the metallic melt, they are reduced to hydrogen and carbon monoxide according to the reactions:

$$xM + yH_2O \rightleftharpoons M_xO_y + yH_2$$

$$xM + yCO_2 \rightleftharpoons M_xO_y + yCO$$

The product gases of these reductions may react further according to equilibria such as:

$$xCO + yH_2 \rightleftharpoons C_xH_{2(y-x)} + xH_2O .$$
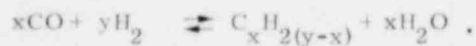
These hydrogenation equilibria are driven to the right only at relatively low temperatures. Less than 1 weight percent of methane and only traces of ethene or higher hydrocarbons were detected in tests described here (see Table III).

18

TABLE III

Equilibrium Compositions for Restored Analysis of Gas
900°C to 1700°C (Mole %)

Sample 1

Species	900°C	1100°C	1300°C	1500°C	1700°C
H_2	22.15	19.79	18.12	16.91	16.01
CO	47.01	49.38	51.05	52.24	53.11
CH_4	0.003	---	---	---	---
CO_2	19.31	16.94	15.27	14.07	13.18
H_2O	11.53	13.90	15.56	16.76	17.64
H	---	---	---	0.01	0.05

Sample 2

Equilibrium Compositions for Restored Analysis of Gas
900°C to 1700°C (Mole %)

Species	900°C	1100°C	1300°C	1500°C	1700°C
H_2	15.79	13.11	11.31	10.06	9.14
CO	32.50	35.18	36.98	38.23	39.12
CH_4	---	---	---	---	---
CO_2	32.00	29.32	27.53	26.27	25.37
H_2O	19.70	22.38	24.18	25.43	26.31
H	---	---	0.001	0.009	0.04

The reduced gas stream emerging from the top of the iron and steel melts used in the tests readily ignited when they came into contact with air. These flames behaved in a diffusional rather than a mixed fashion.

Compositions of gas streams generated during the tests did not mimic well the atomic composition of volatile species available in the concrete. In most cases gas samples extracted from the streams had H_2/C ratios much higher than the ratio in the concrete. Reactions which produce gases in the melt/concrete interaction do not take place at the concrete interface with the melt but at distances from this interface dictated by the temperature profile developed in the concrete by the presence of the melt. This profile was explored in the heat-flux tests described above

(see Appendix D) and found not be a step function. Temperature data above $150^{\circ}C$ within the exposed concrete samples could be explained in terms of a conductive model using the similarity variable, $\frac{Z - Z_s}{\sqrt{t}}$, where t = time and $Z - Z_s$ = distance from the interface as shown in Figure 4. This model, as well as the gas data, indicate that the distance into the concrete over which the dehydration is complete grows much more rapidly than does the extent of complete decarboxylation. As a consequence, the gas streams produced in a melt/concrete interaction, even when the exposed concrete is of the calcareous variety, are quite rich in hydrogen (see Table III).

Aerosol emissions accompanied gas emissions especially in the high-temperature, small-scale tests. Quantitative data concerning the concentration and composition of these aerosols are still quite sparse. Aerosol densities were at least $0.06 \ g/m^3$. The aerosols were composed of iron, silicon, and aluminum oxides as well as carbon (possibly precipitated from the gas phase). Though fission product mocks MoO_3, SrO, UO_2, ZrO_2, CeO_2, and La_2O_3 were included in the small-scale melts, none of these species were detected in the aerosol, possibly because of the limited sensitivity of methods used to analyze the powders. The aerosols were multimodel in their particle-size distribution as would befit their heterogeneous composition. Particle sizes within the respirable range ($\sim 10\mu$) made up a significant proportion of the aerosol (see Figure 5).
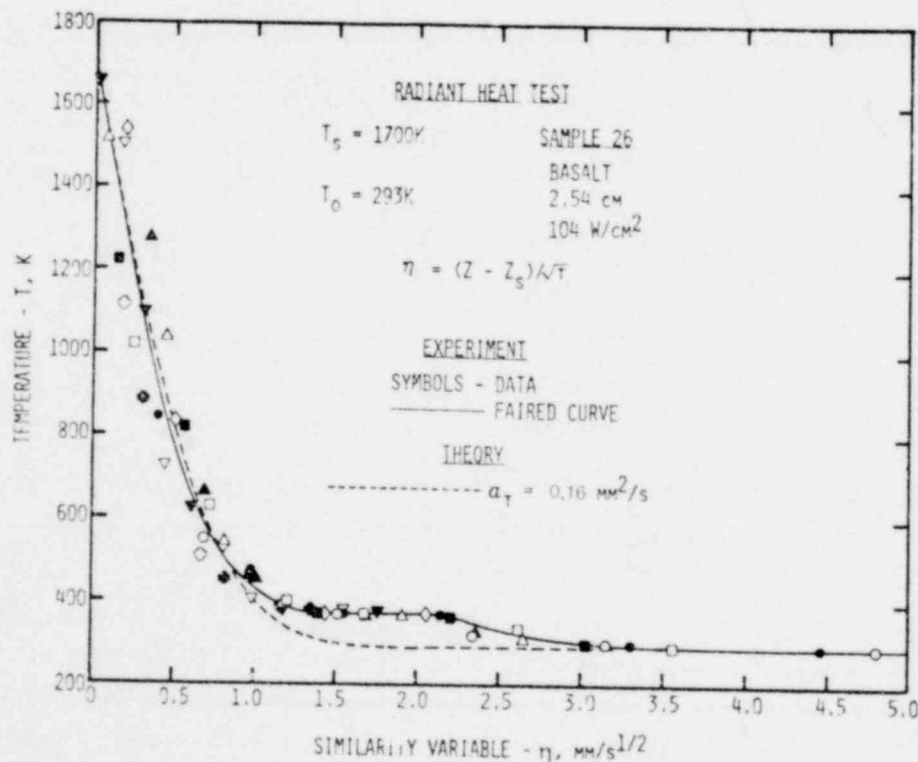

Figure 4. Calculated and Experimentally Determined Thermol Response of Concrete

20

PARTICLE SIZE DISTRIBUTION
OF THE AEROSOL FROM TEST SSL-1

CUMULATIVE NO. %

0.01
0.05
0.1
0.2
0.5
1
2
5
10
20
30
40
50
60
70
80
90
95
98
99
99.8
99.9
99.99

1.0   2.0   3.0   4.0

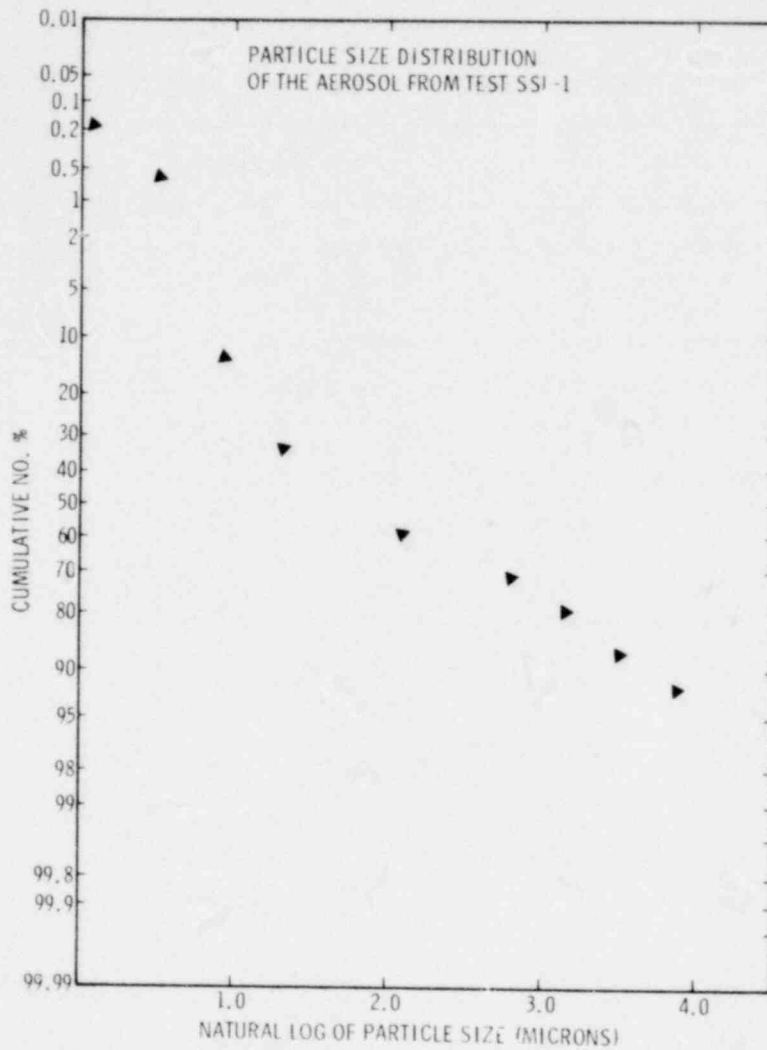NATURAL LOG OF PARTICLE SIZE (MICRONS)

Figure 5.   Particle Size Distribution of the Aerosol from Test SSL-1

Extensive cracking was observed in all the concrete crucibles used in both the large- and small-scale tests. These cracks were initiated quite early in the tests at the top of the crucible and propagated downward. The cracks were interaggregate fissures that passed deeply into the body of the crucible. In all respects these cracks were consistent with thermally-induced tensile failure of the concrete.

While melt was present in the crucibles, the cracks grew to widths of up to 0.8 mm. However, in no case was it observed that melt penetrated into these cracks. Liquid water did enter the cracks and migrated along them to the external walls of the crucible. This liquid water was believed to be evaporable water driven ahead of the thermal wave generated in the concrete by the melt.

Though experiments in the Molten Core - Concrete Interactions Study were sizable, the amounts of concrete and melt involved in these tests were small compared with the amounts that would be involved in a core meltdown reactor accident. Extrapolation of the experimental results to predict the nature of a meltdown accident must be cautiously done. Factors making scale-up of the experimental results difficult are not easily quantified, but the following generalizations may be considered:

1. Concrete decomposition and melting chemistry are insensitive to experimental scale and may be effectively studied in small tests, provided attention is given to careful sampling.

2. Gas reduction by the melt is scale dependent, but the tests reported here were large enough that useful results are available.

3. Concrete erosion is well defined by tests in which total erosion amounts to at least one or two characteristic aggregate dimensions.

4. Heat and mass flow behavior in and about the melt is both scale and geometry dependent.

5. Extrapolation of mechanical behavior of concrete is not comfortably done from the available test results.

Gas flow within the melt has a direct effect on the nature and extent of concrete erosion. It has particular influence on the horizontal-to-downward erosion ratio. The crucible cavities used in the tests were quite confined and, as a consequence, the gas flow effects on erosion may have been accentuated. The confinement may also influence convection in the melt.

Cracking of the concrete crucibles was observed in every test of the experimental program whether large or small in scale. Whether this cracking would also occur in very large concrete fixtures remains an open question. Spallation of the concrete surface, however, ought not be dependent on experimental scale.

The extent of reduction of water and carbon dioxide passing through the melt is dependent, at a given temperature, on the time the gases are in contact with the melt. Observed gas data show that reduction of water was nearly complete in the test so that increased melt masses would not affect these results. Reduction of carbon dioxide was not so complete, though gas equilibrium effects may be responsible for the observed CO/CO_2 ratios.

Data generated in the experimental phases of the Molten Core-Concrete Interactions Study have been used as a basis for a model of the melt/concrete interaction called INTER. Phenomena observed in the experimental studies which are considered in the INTER code are listed as follows:

1. Separate oxide and metallic layers with average density, conductivity, specific heat, and thermal profiles

2. Decay heating by fission products dissolved in either layer

3. Dissociation of specific concrete types

4. Heat conduction in the concrete

5. Radiation from the melt top surface

6. Flow of gases through the melt and their heat transport from the melt

7. Material flow, especially oxides

8. Reactions between gases flowing through the melt and the melt

9. Reactions between nonvolatile concrete decomposition products and melt constituents

10. Dissolution of decomposition products in the melt

11. Melt/concrete interface heat transfer

12. Geometry of the melt

13. Water in the reactor cavity

The computation starts with an initial melt composition and temperature and the properties and composition of concrete. The rate of advance of the decomposition front, and hence the rate of mass addition of each concrete species to the melt, is computed. Gases can react with metals and the appropriate heats of reactions are included. The flows of heat between the melt layers, from the layers to the concrete, and radiated from the melt surface are computed. These heat flows are combined with the decay heat, heats of reaction, and the enthalpy of entering and leaving materials to compute a new temperature. Mass flows and reactions are used to compute new compositions and masses.

The position of the decomposition front is monitored at several points, and a limited number of geometric figures is fitted to the advancing decomposition front.

The running time of the code varies with the type of problem, but, for a typical LWR core melt problem, 10 sec of CDC6600 computer time per hour of problem time is typical.

At present, INTER is a very empirical code and there exists great uncertainty in many of the parameters utilized in its computational routines. For this reason, the code serves best to determine the sensitivities of the output to modifications in the input data. In this, INTER is a useful tool for guiding the direction and focus of experimental studies of the melt/concrete interaction. The code is not yet sufficiently refined to provide reliable predictions of the course of meltdown accidents in nuclear reactors.

Summary

This research program has succeeded in producing a substantial increase in understanding of molten core materials/concrete interaction and the resulting effects important to containment analysis. A qualitative understanding of the molten metal/concrete interaction has been obtained, and quantitative data have been obtained on many specific phenomena. It is likely that all significant phenomena that might be present in a core meltdown accident have been identified in this program. This work has produced an experimental technology which will shortly allow a determination of the phenomenological behavior of the interaction of UO_2 containing melts with concrete utilizing sizable experiments and prototypic temperatures.

A preliminary model has been developed. It is comprehensive, but significant approximations and simplifications are required for some phenomena. It has been distributed to a number of interested organizations and is presently being used for sensitivity studies and risk analysis.

Results from the Molten Core - Concrete Interaction Study have been widely distributed (page 10 includes a list of publications). The information in this report should supersede other previously reported data when any conflicts are noted.

References

1. U. S. Nuclear Regulatory Commission, Reactor Safety Study, An Assessment of Accident Risks in U. S. Commercial Nuclear Power Plants, Main Report, N. Rasmussen, Ed., WASH-1400, NUREG-75/014, Oct 1975.

2. Nuclear Fuel Cycle Safety Research Department, Core Meltdown Experimental Review, SAND74-0382, NUREG-0205, Sandia Laboratories, Albuquerque, NM, March 1977.

3. D. A. Powers, Molten and Core/Concrete Interactions Project Description, 189 No. A-1019, Sandia Laboratories, 1975.

4. D. W. Larson and D. O. Lee, Fluid-Mechanic/Thermal Interaction of a Molten Material and a Decomposing Solid, SAND76-0240, Sandia Laboratories, Albuquerque, NM, Dec 1976.

APPENDIX A

CONCRETE CHARACTERIZATION

APPENDIX A

CONCRETE CHARACTERIZATION

1. Introduction

Experimental phases of the Molten Core - Concrete Interactions Study employed concrete representative of that found in existing light-water nuclear reactors.[1] Two generic categories of concrete are typically encountered in these existing facilities:

a. Concrete based on calcareous or dolomite aggregate.

b. Concrete based on basaltic or silaceous aggregate.

Differences would be expected in the high-temperature behavior of these concrete types. Both concrete types are susceptible to dehydration at elevated temperatures. Calcareous concretes are also susceptible to decarboxylation and produce substantially more gas per cubic centimeter at elevated temperatures then basaltic concretes. Composition differences would be expected to introduce more subtle variations in the melting behaviors of the concretes.

The differences in high-temperature behaviors of the concrete provide an excellent basis for the qualitative evaluations of the melt/concrete interaction sought in the experimental program. Differences in gas generation at elevated temperatures are especially important since noncondensible gases produced during a meltdown accidents are particularly pertinent to questions of nuclear reactor safety. Therefore, test matrices developed for the experimental tasks were designed so that the behaviors of basaltic and calcareous concrete could be compared. These concrete types used in the experiments described in Appendices B-D are characterized here in terms of their bulk properties, chemical compositions, and thermochemical behaviors.

2. Concrete Fabrication

Concrete fixtures used in the experimental program were prepared by the Civil Engineering Research Facility operated by the University of New Mexico. To the extent possible, the concrete samples were representative of concrete found in existing light water reactors. Specifications for the concrete were drawn from descriptions provided by Bechtel Power Corporation[2], safety analysis reports for reactors at Turkey Point, Florida (Units 3 and 4)[3], and consultations with personnel of the Nuclear Regulatory Commission[4]. These specifications are summarized in the following list.

Concrete Specifications*

1. Compressive strength after curing 90 days is to be 4000 lb/in^2 minimum.

2. Slump is 2 inches.

3. Cement is to be American Type II Portland Cement.

4. Air content is to be 3 to 5 percent by volume.

5. Air entraining agent specified by reference 5.

6. Composition of the cement mix is specified by reference 6.

7. Aggregate sizes and size distributions are specified by reference 7.

8. Water reducing agent is specified by reference 5.

9. Mixing, forming, and placing to conform, where possible, to recommendations set forth in the applicable sections of references 6 through 9.

Mixed compositions of the two concrete types prepared with two sizes of aggregate used in the study are listed in Table A-I. Sources of the mix constituents are listed in Table A-II. Comparisons between the specified and actual size distributions of aggregates and sand used in the concrete samples are shown in Tables A-III and A-IV, respectively. The coarse limestone aggregate in the as-received condition failed to meet the required size specifications. Coarse and fine limestone rock were mixed to form distribution used in the fixtures. The basaltic aggregate was quite zeolite rich. The powdered zeolite prevented satisfactory bonding between the aggregate and the cement. Only after very careful and extensive washing of the aggregate could a satisfactory concrete be made with the basaltic aggregate. All test fixtures made with the basaltic aggregate were made with the washed rock. However, some testing cylinders were made with the unwashed aggregate.

3. Bulk Characterization

Density and compressive strength measurements were made with standard 6-in. dia., 12-inch long concrete testing cylinders. Density data are shown in Table A-5. Compressive strength data were taken after the concrete samples had cured for 7, 28, and 90 days. These data for the coarse basaltic and limestone concretes are shown in Figures A-1 and A-2, respectively. Mean strengths and standard errors for all classes of concrete are listed in Table A-VI. In all cases the mean strength exceeded 4000 psi after the samples had cured for 90 days. The rather large errors associated with data for basaltic concrete are due to the inclusion of data from specimens made with unwashed aggregate.

---

*Drawn from descriptions provided by Bechtel Power Corporation.[2]

TABLE A-I

Compositions of Concrete Mixes

Concrete Type	Cement (lb)	Water (lb)	Sand (lb)	Coarse Aggregate (lb)	Fine Aggregate (lb)	AEA[*] (oz)	WRA[**] (oz)
Coarse limestone	94	42	205	187	93	3/4	0
Fine limestone	94	41	200	0	160	3/4	0
Coarse basalt	54	45	230	205	0	3/4	1
Fine basalt	54	41	173	0	134	3/4	1

[*] Air Entraining Agent

[**] Water Reducing Agent

TABLE A-II

Sources of Materials

Product	Supplier
Cement	Ideal Portland Cement Co.
Air Entraining Agent	Burke Concrete Accessories, Inc.
Water Reducing Agent	Sika Chemical Corp. (Plastimet)
Curing Compound	Carter-Waters Co.
Mold Release	(Common chassis grease)
Aggregate } Sand	Albuquerque, New Mexico

TABLE A-III

Comparison Between Observed and Specified Aggregate Size and Size Distributions

(A) <u>COARSE AGGREGATE</u>

Screen Opening Size (inch)	Specified Weight % Passing Through Screen	Observed Weight % Passing Through Screen		
		As received Limestone	Basalt	Mixed Limestone
1.0	95-100	100	100	100
0.75	90-100	39.5	98.9	59.6
0.5	25-60	4.1	52.5	36.0
0.375	20-55		20.8	33.3
0.19	0-10		1.0	6.7
0.09	0-5		0	0.07

(B) <u>FINE AGGREGATE</u>

Screen Opening Size (inch)	Specified Weight % Passing Through Screen	Observed Weight % Passing Through Screen	
		Limestone	Basalt
0.5	100	100	100
0.375	85-100	100	99.4
0.19	10-30	20.1	32.6
0.09	0-10	0.2	1.1
0.047	0-5	0	0.5

TABLE A-IV

Size Distribution of Concrete Sand

Size (in.)	Weight % Passing Through This Screen	
	Specified	Observed
0.375	100	100
0.19	95-100	95.2
0.09	80-90	82.2
0.047	55-75	70.6
0.023	30-60	52.2
0.012	12-30	18.5
0.006	2-10	3.0
0.003	---	0.8

1570 122

TABLE A-V

Density of Concrete After 90 Days of Cure

Concrete Type	Density (lb/ft^3)
Coarse limestone	146
Fine limestone	145
Coarse basalt	141
Fine basalt	142

TABLE A-VI

Mean Observed Compressive Strengths at Various Cure Times for Samples of Concrete Used in the Program

	Time of Cure[*]		
Sample	7 Days	28 Days	90 Days
Coarse limestone aggregate concrete	2872±384	3805±382	4319±437
Coarse basalt aggregate concrete	3085±601	4266±766	4752±942
Fine limestone aggregate concrete	2726±36	3396[**]	4308[**]
Fine basalt aggregate concrete	2976±28	3781±113	4917[**]

[*] Error assigned to the mean strength values is

$$error = \left[\sum_{i=1}^{N} (X_i - <S>)^2 / (N - 1) \right]^{1/2}$$

where N = number of observations, S_i is the observed strength, and $<S>$ is the mean observed strength.

[**] Insufficient numbers of samples examined to compute a meaningful error.
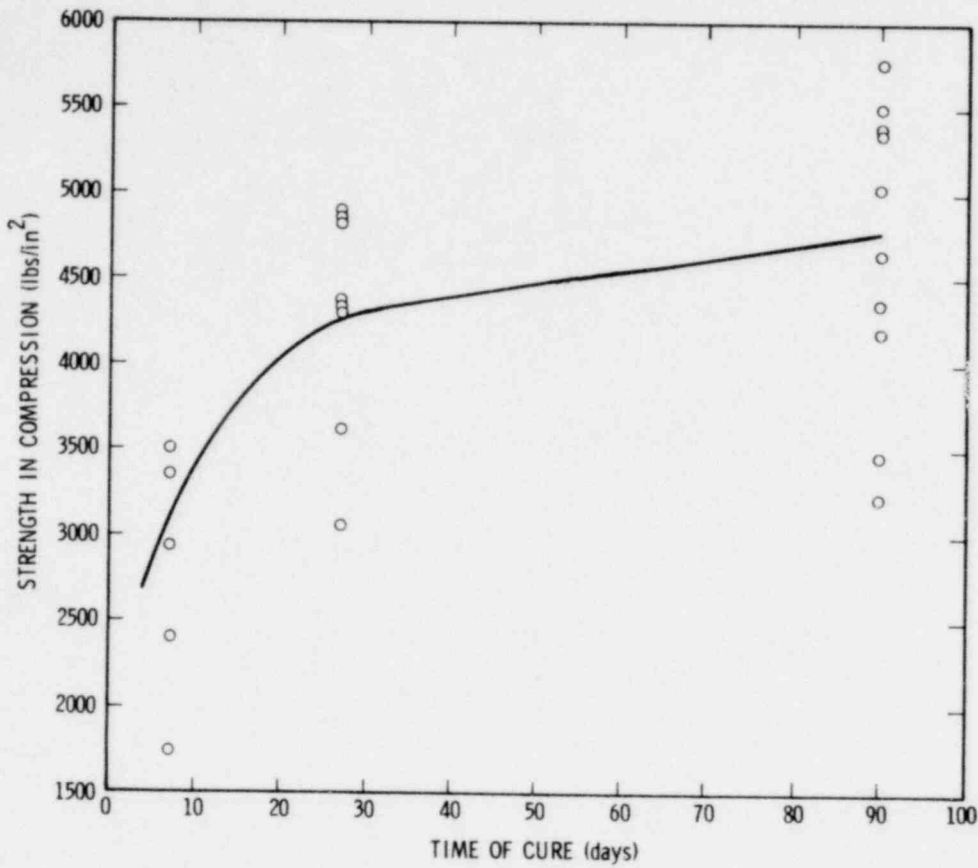
Figure A-1. Comprehensive Strength Data for Coarse Basaltic Concrete Samples
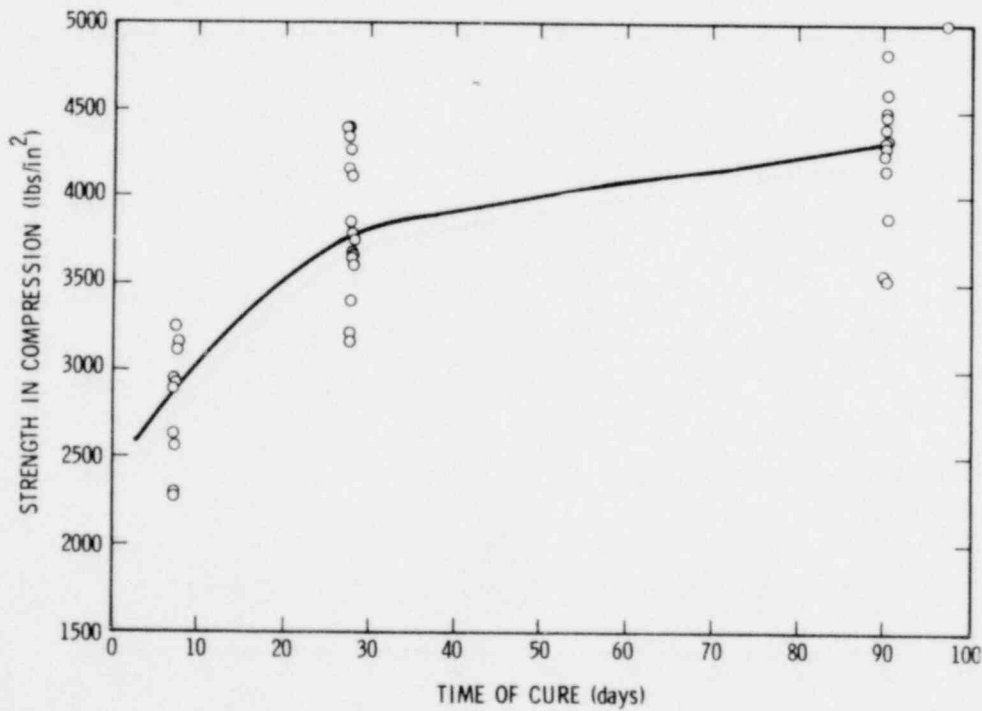
Figure A-2. Comprehensive Strength Data for Coarse Limestone Concrete Samples

1570 124

4. Chemical Composition of Concrete

Chemical analysis of concrete is a most demanding chore. Complete dissolution of all minerals is essential if accurate results are to be obtained. The complexity of the elemental composition raises the possibility of interferences in the analyses of many of the components. The following procedure, a modification of a method used to analyze geological specimens, proved satisfactory for the dissolution of concrete.

A sample 100 to 150 mg in size was weighed to the nearest 0.01 mg and placed in a Teflo crucible of a Parr Acid Dissolution Bomb. One milliliter of an acid mixture, containing one p concentrate nitric acid and three parts concentrated hydrochloric acid by volume, was added o this sample. The crucible was loosely capped and periodically agitated for 1 hr. Three milliliters of concentrated hydrofluoric acid were then added to the slurry. The crucible was sealed in the bomb and heated to 110°C for 1-1/2 hrs. After cooling, the crucible contents were transferred into polyethylene bottles with the aid of 5 to 7-ml distilled water. The sample was treated with 2.8-g boric acid and diluted to 40 ml with distilled water. The mixture was allowed to stand with intermittent agitation until all solids had dissolved. The solution was diluted tc 100.0 ml with distilled water and stored in polyethylene bottles.

Atomic absorption was satisfactory for most analyses. Superior analyses for aluminum and calcium were obtained when cesium or lanthanum salts were added to the sample solutions to suppress oxidation in the containment flame. These problems were circumvented when induction coupled plasma techniques were used for analysis of the samples. This latter method was the only technique satisfactory for the analysis of titanium. Silicon analyses were confirmed by the well-known perchlorate dehydration method. Differences in results between this wet method and the results from instrumental measurements never amounted to more than 0.2 weight percent (w/o) silicon. Results of the analyses along with estimates of the total probable error in the results are shown in Table A-VII.

5. High-Temperature Behavior of Concrete

Melting and thermally initiated decomposition reactions which yield volatile products are the aspects of high-temperature concrete chemistry pertinent to questions of reactor safety. The chemical heterogeneity of concrete greatly complicates investigation of either of these facets of concrete chemistry. Most features of interest, however, arise in the cementituous phases of the concrete.

TABLE A-VII

Chemical Composition of Concrete Samples and Concrete Constituents

Sample	CaO	SiO_2	Al_2O_3	FeO	Na_2O	K_2O	MgO	TiO_2	MnO
Basaltic concrete	9.63	55.6	8.05	ND	1.95	3.60	3.96	1.05	ND
Basaltic aggregate	6.73	51.1	10.20	ND	2.08	4.00	4.33	1.38	ND
Calcareous concrete	32.38	36.4	4.03	ND	0.81	1.17	0.79	0.08	ND
Calcareous aggregate	45.56	10.6	1.25	ND	0.15	0.30	0.80	0.05	ND
Sand	1.0	80.5	7.8	1.8	1.93	2.56	0.22	0.20	0.04
Cement	61.6	21.3	3.6	3.8	0.24	0.46	1.59	0.20	0.1
Cement Paste	46.	16.3	2.4	2.8	0.18	0.29	1.22	0.14	0.1
Total Probable Error as % of Observed Value	2	5	1	3	1	2	4	5	3

ND = not determined

Material prepared just as were the concrete specimens except no aggregate was incorporated in the mix.

The cementitious phases are formed by the hydration reactions depicted in Table A-VIII. Any of the underlined product species in this table may be present in the cementitious phase. Their concentrations are often time dependent. These product species are characterized in Table A-IX. All of these species are subject to thermally initiated dehydration reactions which yield water as a product. Dehydration of these species together with the decarboxylation of carbonates present in the concrete are the reactions which yield noncondensable gases when concrete is exposed to elevated temperatures.

Sufficiently vigorous heating of gypsum will yield sulfur oxide gas. This reaction has been neglected in this document. The concentration of calcium sulfate is small in concrete. Also, if molten iron is present, sulfur oxide gases are completely absorbed into this melt.

TABLE A-VIII

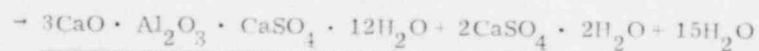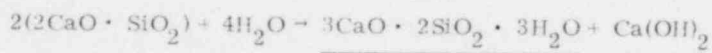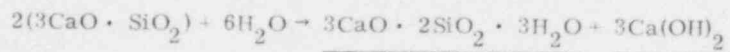Hydration Reactions of Principal Constituents of Portland Cement

$$2(3CaO \cdot SiO_2) + 6H_2O \rightarrow 3CaO \cdot 2SiO_2 \cdot 3H_2O + 3Ca(OH)_2$$

$$2(2CaO \cdot SiO_2) + 4H_2O \rightarrow 3CaO \cdot 2SiO_2 \cdot 3H_2O + Ca(OH)_2$$

$$4CaO \cdot Al_2O_3 \cdot Fe_2O_3 + 2Ca(OH)_2 + 10H_2O \rightarrow 6CaO \cdot Al_2O_3 \cdot Fe_2O_3 \cdot 10H_2O$$

$$\rightarrow 3CaO \cdot Al_2O_3 \cdot 6H_2O + "3CaO \cdot Fe_2O_3 \cdot nH_2O" + (4 - n)H_2O$$

$$3CaO \cdot Al_2O_3 + 6H_2O \rightarrow 3CaO \cdot Al_2O_3 \cdot 6H_2O$$

$$3CaO \cdot Al_2O_3 + 3(CaSO_4 \cdot ZH_2O) + 25H_2O$$

$$\rightarrow 3CaO \cdot Al_2O_3 \cdot 3CaSO_4 \cdot 31H_2O$$

$$\rightarrow 3CaO \cdot Al_2O_3 \cdot CaSO_4 \cdot 12H_2O + 2CaSO_4 \cdot 2H_2O + 15H_2O$$

$$3CaO \cdot Al_2O_3 \cdot CaSO_4 \cdot 12H_2O \rightarrow 3CaO \cdot Al_2O_3 \cdot 6H_2O + CaSO_4 \cdot 2H_2O + 4H_2O$$
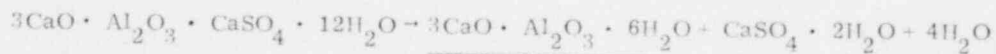
TABLE A-IX

Structures of Concrete Hydration Products

Common Formula	Structurally Significant Name	Structure
$Ca(OH)_2$	$Ca(OH)_2$	CdI_2 structure; OH groups for hexagonal close-pack layers with Ca^{2+} ions in holes between alternate layers along c-axis. Dipolar bonding between adjacent OH layers and ionic bonding between metal ion and the anions. Hexagonal a = 3.58, c = 4.909Å. Reference 10.

Common Formula	Structurally Significant Name	Structure
$3CaO \cdot 2SiO_2 \cdot 3H_2O$	$Ca_3[SiO_3OH] \cdot 2H_2O$	Monoclinic a = 16.27, b = 5.63, c = 13.23 β = 134°48', Z = 4. Space Group Cc. Three distinct Ca^{2+} ions are present.
		Ca(I) has triagonal biprismic coordination sphere made up of two OH groups and 4 oxygens.
		Ca(II) has approximate seven-fold coordination by 2 OH groups, a water molecule and 4 oxygens.
		Ca(III) has six-fold coordination by four OH groups and two water molecules. Reference 11.
$3CaO \cdot Al_2O_3 \cdot 6H_2O$	$Ca_3[Al(OH)_6]_2$	Cubic; a = 12.56 Å; Z = 4. Space group Ia_3d. Aluminum ions located within an octahedral coordination sphere of OH groups. Reference 12.
$3CaO \cdot Al_2O_3 \cdot$ $3CaSO_4 \cdot 31 H_2O$	$Ca_{12}Al_4(OH)_{24}(SO_4)_6 \cdot$ $50 H_2O$	Hexagonal; a = 11.10, c = 21.58 A. A = 2; Space group $C\bar{3}_1c$.
		4 calcium ions have 7-fold coordination, and 8 have 6-fold coordination. Aluminum is located within an octahedral array of OH groups. Forty-eight molecules are in channels parallel to the 1 axis and are readily lost at 100-110°C. Two water molecules are tightly held within the structure and are lost at ~160°C. $Al(OH)_6$ breaks down at ~300°C. References 13, and 14.
$CaSO_4 \cdot 2H_2O$ (gypsum)		$1\frac{1}{2}$ molecules H_2O lost at 128°C $\frac{1}{2}$ molecule H_2O lost at 163°C
$5CaO \cdot 6SiO_2 \cdot nH_2O$ (Tobermorite)	$Ca_5(Si_6O_{16}(OH)_2) \cdot$ $(n - 1)H_2O$	A number of such species have been described, usually in terms of the d-spacing of the 002 reflection in their powder diffraction patterns.

36

Common Formula	Structurally significant Name	Structure	
		d_{002}	n
		14.3	9
		11	5
		9.3	1
		12.6	?
		10	?

All structures are related to that for 11 Å tobermorite, which is:

Triclinic (?) a = 11.3, b = 7.3, c = 22.6 Å. Layers of $Ca(OH)_2$ are flanked by kinked, SiO_3 chains. Kinks in the chains leave cavities for the remaining Ca^{2+} ion and water molecules. References 15 and 16.

Melting and thermal decomposition reactions in concrete types used in this study have been investigated using the techniques of classical thermal analysis: thermogravimetric analysis, differential thermal analysis, and differential scanning calorimetry.

Differential thermograms of basaltic and calcareous concrete are shown in Figures A-3 and A-4, respectively. Melting endotherms for both of these species begin at temperatures slightly less than 1100°C. Melting is complete for both at temperatures between 1350 and 1400°C. Comparison of the magnitude of the endotherms with that of CaF_2 (mp = 1360°F) suggests that the enthalpy of melting of concrete is approximately 100 cal/g (20 cal/g). The endotherms, due to dehydration of calcium hydroxide and the $\alpha \rightarrow \beta$ phase change of SiO_2, may be seen in Figure A-3. The endotherm due to decarboxylation of limestone in the calcareous concrete is shown in Figure A-4.

Weight losses from calcareous and basaltic concrete as functions of temperature are shown in Figures A-5 and A-6, respectively. Weight loss in both concrete types consist of three distinct events: loss of evaporable water (30 to 250°C), loss of chemically-constituted water (400 to 550°C), and loss of carbon dioxide (550 to 800°C). Loss of evaporable water is due to vaporization of molecular water from species such as Tobermorite, Ettringite, and $3CaO \cdot 2SiO_2 \cdot 3H_2O$. The weight loss assigned to chemically-constituted water is caused mainly by dehydration of $Ca(OH)_2$. Dehydration of $3CaO \cdot Al_2O_3 \cdot 6H_2O$ may also contribute to this weight loss. The decarboxylation weight loss in the thermogram of basaltic concrete is due to thermal decomposition of $CaCO_3$ formed in the cementituous phase during concrete fabrication. Decarboxylation weight loss in the thermogram of calcareous concrete is, of course, principally the result of thermal decomposition of the aggregate.

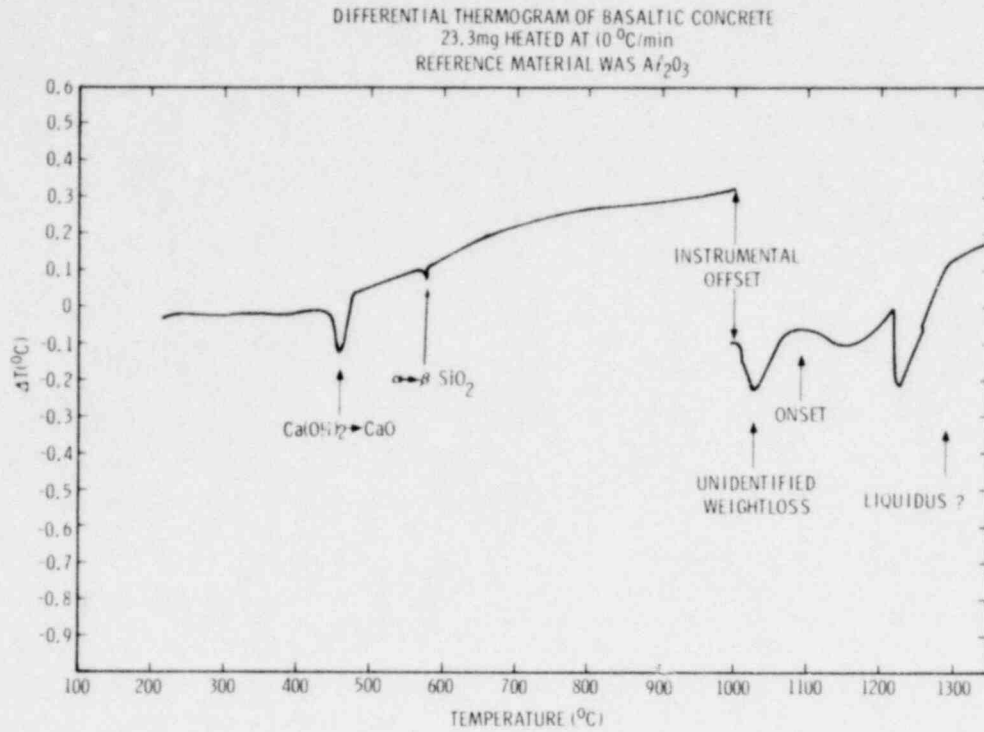DIFFERENTIAL THERMOGRAM OF BASALTIC CONCRETE
23.3mg HEATED AT 10 °C/min
REFERENCE MATERIAL WAS Al₂O₃

Figure A-3. Differential Thermogram of Basaltic Concrete (23.3 mg Heated at 10°C/min, Reference Material was Al_2O_3)

DIFFERENTIAL THERMOGRAM OF CALCAREOUS CONCRETE
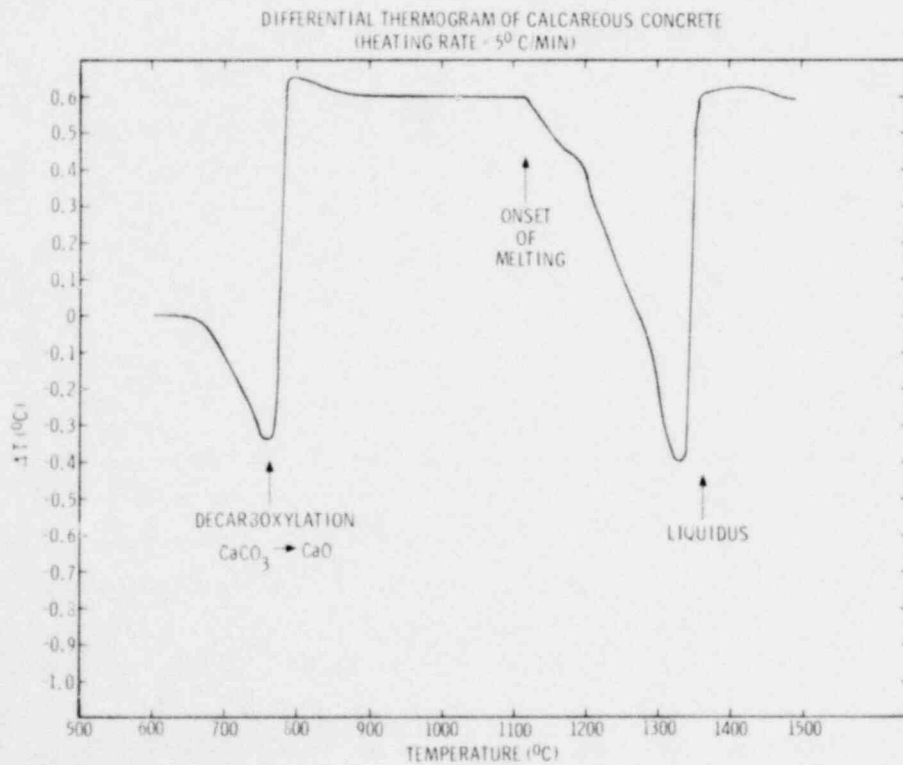(HEATING RATE - 5⁰ C/MIN)

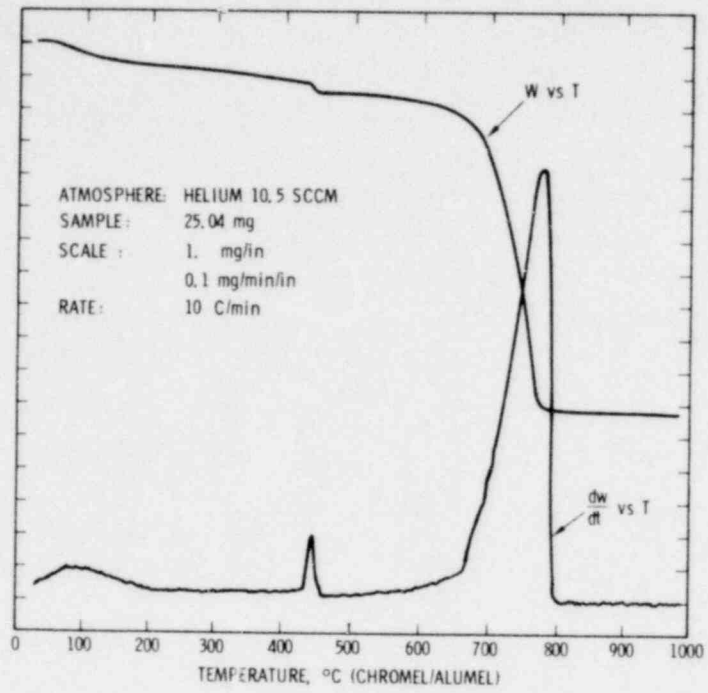Figure A-4. Differential Thermogram of Cancareous Concrete (Heating Rate = 5°C/min

1570 130

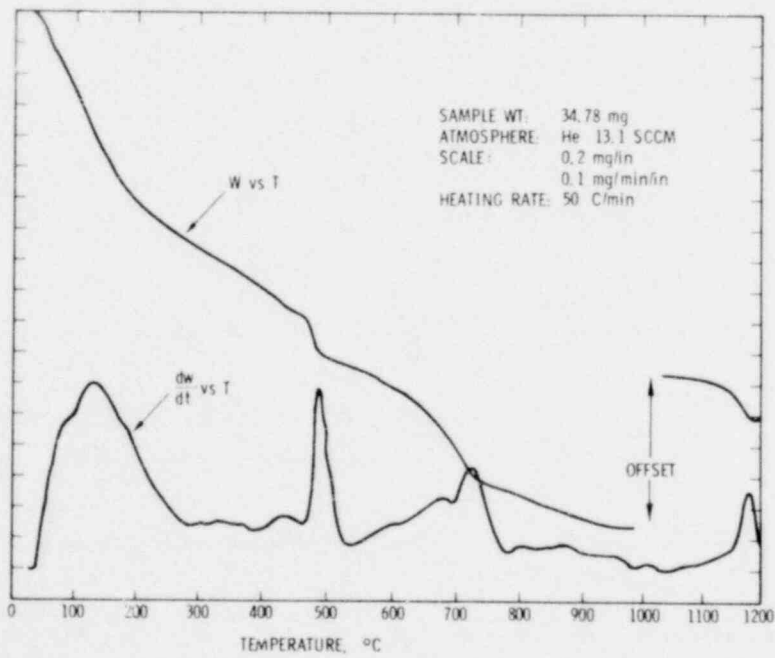Figure A-5. Weight Losses from Calcareous Concrete Shown as a Function of Temperature

Figure A-6. Weight Loss from Basaltic Concrete Shown as a Function of Temperature

Dynamic thermograms such as those in Figures A-5 and A-6 are satisfactory for determining the stoichiometry of weight losses for reactions occurring at temperatures greater than $150^{o}C$. Crushing of concrete to the powder size necessary for these dynamic experiments causes release of some of the evaporable water in the concrete. The stoichiometry of this type of weight loss is best determined with bulk samples of at least 1 kg.

Results of such determinations of evaporable water losses for calcareous and basaltic concrete are shown in Figure A-7.
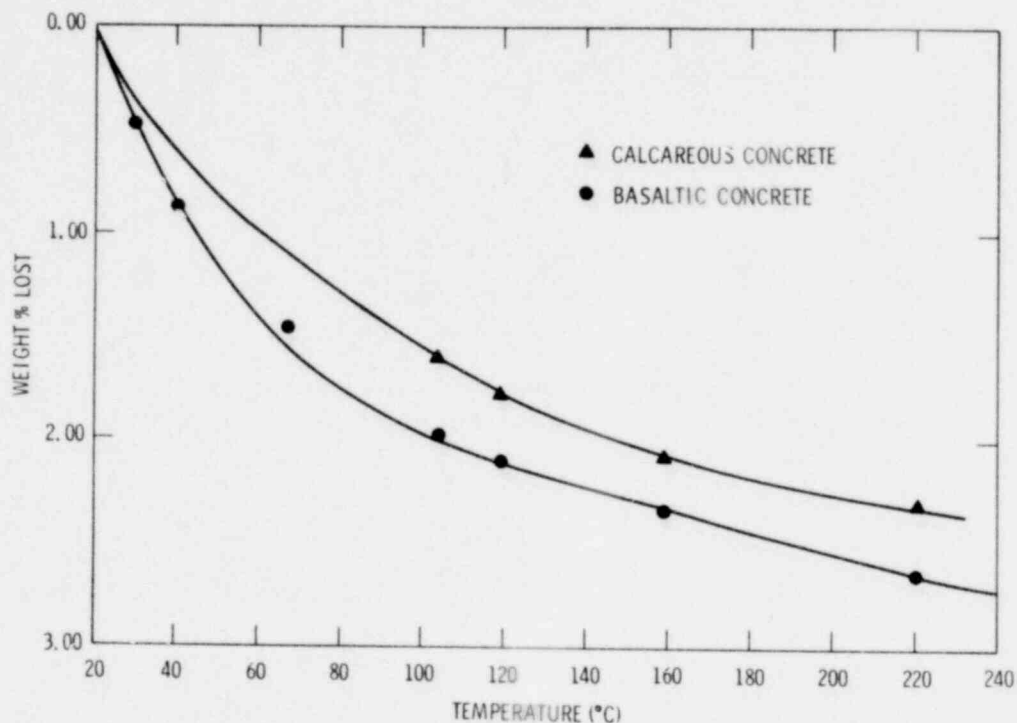
Figure A-7. Bulk Weight Loss from Concrete Exposed to a Static Heating Environment

6. Empirical Models of the Kinetics of Concrete Decomposition Reactions

It is quite clear that many of the important phenomena associated with the interaction between concrete and a high-temperature melt depend on the nature of heat transfer within the concrete.

If water migration other than vaporization is neglected, the equation governing heat transfer within the concrete is:

$$\frac{\partial T}{\partial t} = \frac{\partial}{\partial s} \alpha(T) \frac{dT}{\partial s} - \sum_{i=1}^{N} \frac{\gamma_i h_i}{C_p(T)} \quad .$$

40

where

T = temperature

t = time

$\alpha(T)$ = thermal diffusivity

$Cp(T)$ = heat capacity

h_i = enthalpy of the ith reaction

r_i = rate of the ith reaction

N = number of pertinent reactions

The right-hand side of this equation consists of a familiar thermal conductivity term and a term due to chemical reactions within the concrete.

Evaluation of the kinetics of chemical reaction in a complex mixture such as concrete is a formidable problem. Determination of mechanistically correct kinetic expressions for each of the three weight-loss events recorded in the thermograms of concrete would necessitate a major research effort not in keeping with the goals of this study. Empirical kinetic expressions devoid of any mechanistic meaning may well be satisfactory for determining heat transfer within concrete.

To derive empirical kinetic expressions for the decomposition reactions in basaltic and calcareous concretes, the following assumptions were made:

1. Each of the three weight-loss events observed in the thermograms of the concrete samples corresponds to the decomposition of a single species.

2. The three decomposition events are independent reactions.

3. Each of the reactions behaves kinetically as an activated, Arrhenius, first-order process

The first of these assumptions is manifestly incorrect. Concrete is made up of a large number of thermally decomposable species, each of which reacts according to its own unique kinetics. Experimental limitations prevent resolution of weight loss in concrete into steps assignable to individual species. Consequently, all reactions taking place in concrete are lumped into one of three "average" reactions.

The second assumption was made out of necessity, since coupling data for the reactions would be most difficult to acquire.

The assumption of first-order behavior provides the mathematic simplicity necessary to make the problem tractable. Certainly, in chemically meaningful mechanistic terms, many of the decomposition reactions of concrete would be better described in terms of nucleation and

growth models. Errors introduced by the first-order assumption may be partially compensated by the empirical adjustment of the kinetic rate parameters. Such adjustments of first-order rate parameters have often yielded satisfactory kinetic representations of complicated reactions.[18]

First-order rate processes obey the kinetic expression:

$$-\ln(1 - \alpha) = K_o \exp(-E/RT)t \qquad (1)$$

where:

α = fraction of reactive species decomposed

K_o = Arrhenius frequency factor

E = Arrhenius activation energy

R = Universal gas constraint

T = Absolute temperature

t = time

Differentiation of Equation (1) with respect to time yields:

$$\frac{d\alpha}{dt} = K_o \exp(-E/RT)(1 - \alpha) \quad . \qquad (2)$$

If the reactive sample is exposed to a linear temperature ramp, then the temperature rate of change of α is given by:

$$\frac{d\alpha}{dT} = \frac{K_o}{\beta} \exp(-E/RT)(1 - \alpha) \quad , \qquad (3)$$

where β is the linear rate of temperate increase.

Differentiation of Equation (3) with respect to temperature yields:

$$\frac{d^2\alpha}{dT^2} = \frac{K_o}{\beta} \exp(-E/RT) \left[\frac{E}{RT^2} (1 - \alpha) - \frac{K_o}{\beta} \exp(-E/RT)(1 - \alpha) \right] \quad . \qquad (4)$$

Consequently, the rate of reaction will reach a maximum at a temperature T_M where:

$$\frac{\beta}{T_M^2} = \frac{RK_o}{E} \exp(-E/RT_M) \quad . \qquad (5)$$

Kinetic parameters for the first-order rate process (K_o and E) may then be found by observing the temperature of maximum reaction rate in samples exposed to a variety of heating rates. The parameters are derived by fitting plots of $\ln \frac{\beta}{T_M^2}$ versus $1/T_M$ to a straight line.

1570 134

Examples of such plots for the reactions of calcareous concrete examined at heating rates of 1 to 100°C/min are shown in Figure A-8. As may be seen in this figure, the linearity is quite good for loss of chemically-constituted water. Deviations from linearity arise in the plot for loss of evaporable water for several reasons, not the least of which is the presence of several chemical species participating in the reaction. Large errors arise in the kinetic parameters for the decarboxylation reaction because this reaction is not in reality a first-order reaction. In spite of these small quibbles, the plots are quite useful for determining the rate constants for the reactions. Once the rate constants are in hand, the rates of reactions for arbitrary heating histories may be found from the expression:

$$\frac{d\alpha_i}{dT} = \frac{d\alpha_i}{dt} \cdot \frac{dt}{dT} \quad .$$

Rate constants for calcareous and basaltic concretes as well as cement paste are summarized in Table A-X.
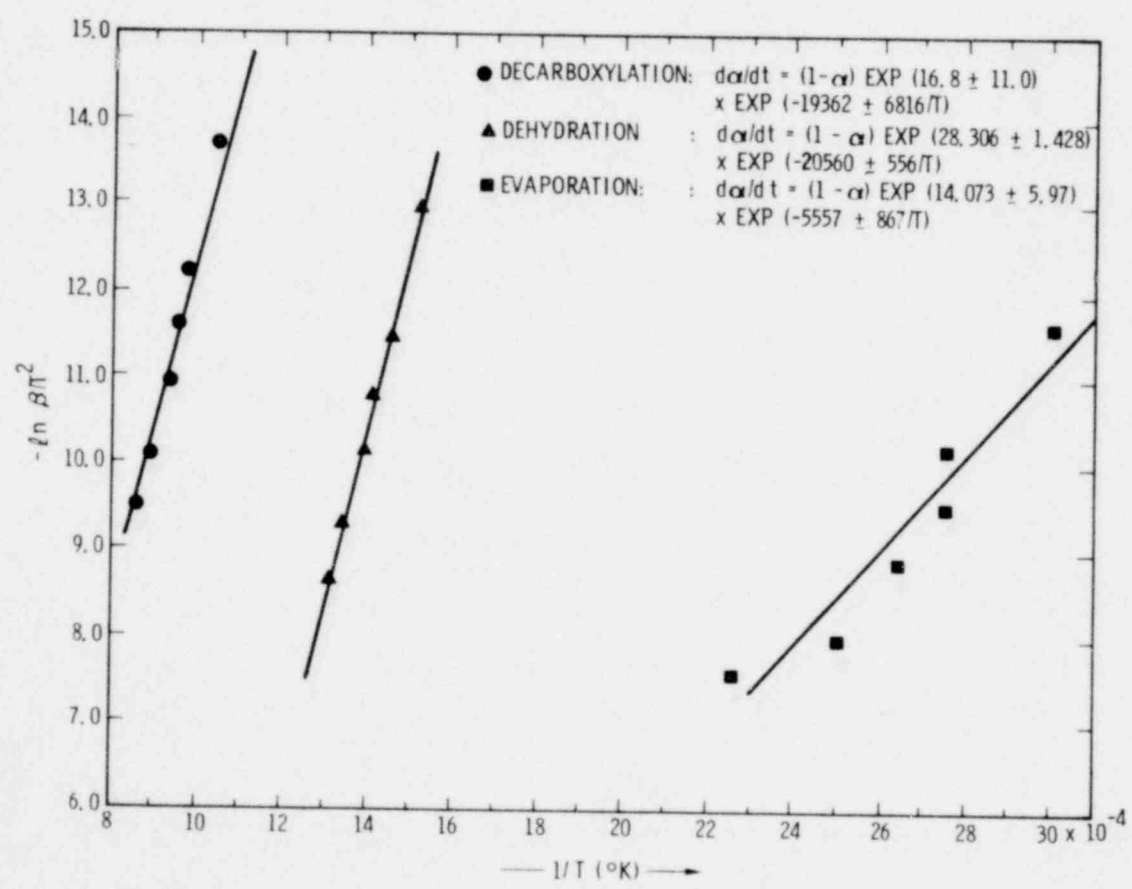
Figure A-8. Examples of Plots Showing Reactions of Calcareous Concrete Examined at Heating Rates of 1 to 100°C/min

1570 135

43

Fractional Order Rate Constants for Weight-Loss Events in Concrete
and Cement Paste

Reaction	Parameters*		
	k_o (min^{-1})	E(cal/mole)	R**
Basaltic Concrete			
a. Evaporable water loss	$(6.78 \pm 3.51) \times 10^8$	12,421±1522	0.9317
b. Chemically-bound water loss - I $(Ca(OH)_2)$ - II	$(2.78 \pm 0.93) \times 10''$	38,422±5290	0.9317
c. Decarboxylation	$(8.66 \pm 7.51) \times 10^5$	44,026±6913	0.9745
Calcareous Concrete			
a. Evaporable water loss	$(7.19 \pm 4.18) \times 10^9$	11,042±1723	0.9241
b. Chemically-bound water loss	$(4.04 \pm 0.31) \times 10^{16}$	40,853±1125	0.9879
c. Decarboxylation	$(3.83 \pm 2.15) \times 10^{11}$	38,472±7543	0.9763
Cement Paste			
a. Evaporable water loss	$(5.80 \pm 3.13) \times 10^6$	12,348±1436	0.9680
b. Chemically-bound water loss - I	$(2.71 \pm 1.50) \times 10^8$	26,354±4606	0.9314
c. Chemically-bound water loss - II $Ca(OH)_2$	$(3.92 \pm 0.51) \times 10^9$	33,503±3563	0.9729

---

*Errors are standard deviations of parameters derived from linear fit.

**R is the linear correlation coefficient of plots of $\ln \beta / T_M^2$ vs $1/T_M$.

The quality of the results may be seen by integrating the rate equation and attempting to reproduce the thermogram. This integration:

$$\int_o^\alpha \frac{d\alpha}{1 - \alpha} = \frac{K_o}{\beta} \int_{T_o}^T \exp(-E/RT) \, dT$$

44

cannot be done in closed form. A variety of approximations are available[19,20] as are numerical solutions[21]. Using the coates-Redfern approximation[19], the concrete thermogram is described by the equation:

$$W(T) = \sum_{i=1}^{3} W_i^o \exp\left\{\left[\frac{-K_i RT^2}{E_i \beta} \left(1 - \frac{2RT}{E_i}\right) \exp(-E_i/RT)\right]\right\}$$

$$+ \sum_{i=1}^{3} W_i^o \left\{\left[\frac{+K_i RT_o^2}{E_i \beta} \left(1 - \frac{2RT_o}{E_i}\right) \exp(-E_i/RT_o)\right]\right\} .$$

where

W = weight remaining

W_i^o = is the weight of material which may be volatilized during the ith reaction

A comparison between the calculated and experimental thermogram of calcareous concrete is shown in Figure A-9. Small deviations are observed in this figure in the region of evaporable water loss. Serious differences develop between calculated and observed thermograms during the decarboxylation reaction. Errors in this region cause underprediction of weight losses.

The description of the decarboxylation weight loss may be improved by assuming that this reaction is a 2/3-order rate process:

$$\frac{d\alpha}{dt} = K \exp(-E/RT) (1 - \alpha)^{2/3} .$$

Kientic parameters appropriate for this reaction in calcareous concrete are:

$K = (3.6 \pm 2.9) \times 10^7 \min^{-1}$

$E = 37.0 \pm 8.2 \ kcal/mole .$

A comparison of experimental data with that calculated from the fractional order and the 2/3-order models for the decarboxylation reaction is shown in Figure A-10. For weight losses corresponding to 10 to 99% of the available carbon dioxide, the 2/3-order model provides an excellent description of ae reaction.
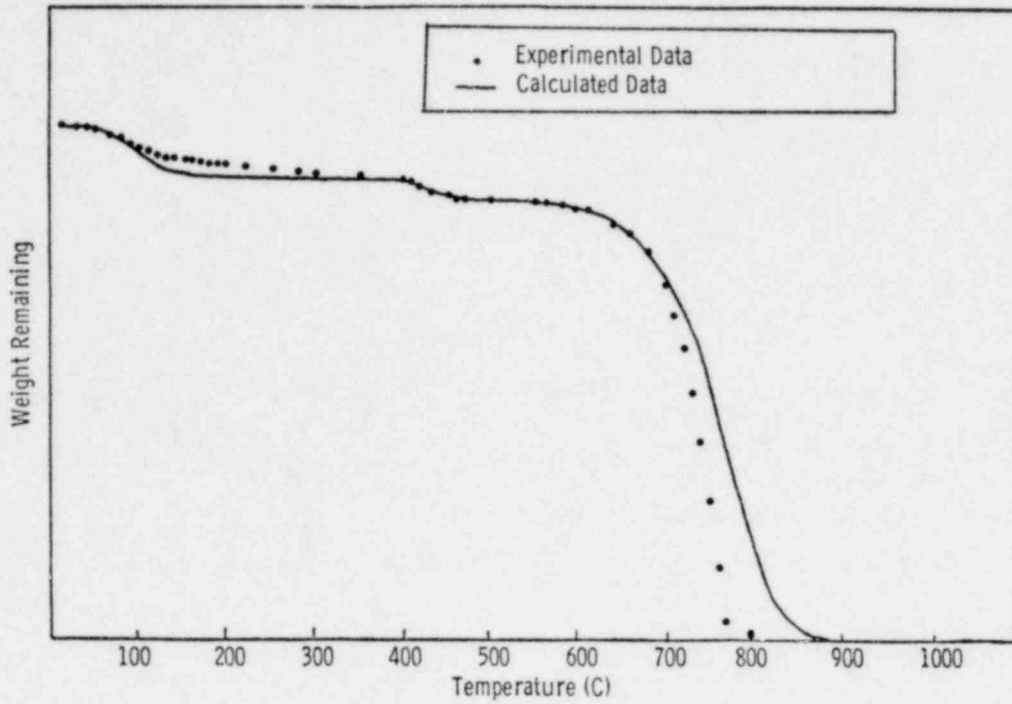
Figure A-9. Comparison of Thermogravimetric Data with Calculated Results
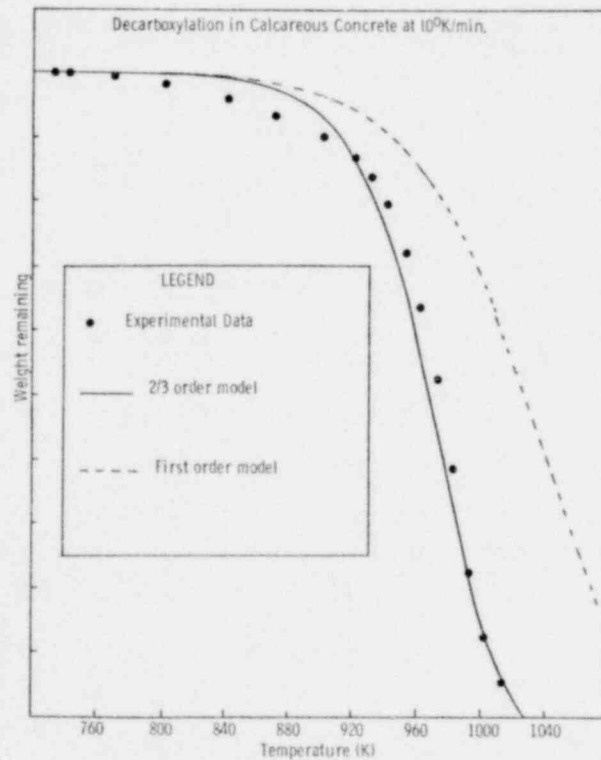of the First-Order Model

Figure A-10. Comparison of 2/3-Order and First-Order Models to Experimental
Data for the Decarboxylation Reaction

46

Decarboxylation of calcium carbonate is a reversible reaction whose kinetics are dependent on the partial pressure of carbon dioxide surrounding the reactive material. This aspect of the kinetics may be easily incorporated in the model to create the kinetic rate equation:

$$\frac{d\alpha}{dt} = K_o \exp(-E/RT)(1-\alpha)^{2/3}\left[1 - \frac{P_{CO_2}}{P_{eq}}\right],$$

where

P_{CO_2} = the partial pressure of CO_2 present in the atmosphere (atm)

P_{eq} = $1.84 \times 10^7 \exp(-39000/RT)$

References

1. Light Water Reactor Safety Research Program Quarterly Report January-March 1976, SAND76-0369, D. A. Dahlgren, Ed., Sandia Laboratories, Albuquerque, NM, Sept 1976.

2. Specification 5853-C-23, 5853-C-21, 5833-C-32 for the Fast Flux Test Facility Test Facility at Richland, Wash., Bechtel Power Corporation, San Francisco, CA.

3. Safety Analysis Report for Turkey Point Units 3 and 4, Vol. 1-3, Cocket 50250-12, 13, 14, 15, Florida Power and Light Co., 1969.

4. L. Shao, Nuclear Regulatory Commission, Washington, DC.

5. ASTM C-494-71 Standard Specification for Chemical Admixtures for Concrete, American Society for Testing and Materials, Philadelphia, PA.

6. ACTI 211. 1-74, Recommended Practices for Normal and Heavy Concrete, American Concrete Institute, Detroit, MI.

7. ASTM 33-74, Standard Specifications for Concrete Aggregates, American Society for Testing and Materials, Philadelphia, PA.

8. ACI 347-68, Recommended Practice for Working Concrete, American Concrete Institute, Detroit, MI.

9. ACI 315-74 Detailing Manual American Concrete Institute, Detroit, MI.

10. G. R. Levi, G. Chim. Inc. Appl. 6, 333 (1924).

11. H. D. Megaw Acta Cryst 2, 419 (1953); 5, 447 (1952).

12. E. Brandeberger, Schwizer Arch. Angew, Wiss, Tech 2, 45 (1936).

13. F. A. Bannister, Minerological Mag. 14, 324 (1936).

14. G. L. Kalousck, G. L. Davis, and W. E. Schmerz, Proc. Am. Conc. Inst. 45, 693 (1949).

15. W. H. F. Taylor, Symp. on the Chemistry of Cements, Tokoyo, Japan, 1968, Cement Association of Japan, Tokoyo, Japan, 1968.

16. H. Bercchem, Disertation Eidg. Tech. Hochschule, Zurick, Germany, 1963.

References (cont)

17. Light Water Reactor Safety Research Program Quarterly Report April-June 1976, SAND76-0677, D. A. Dahlgren, Ed., Sandia Laboratories, Albuquerque, NM, Feb 1977.

18. J. M. Criado and J. Morales, Thermochimica Acta 16, (1976) 382.

19. A. W. Coats and J. P. Redfern, Nature 201, 68 (1964).

20. V. M. Gorbacher, J. Thermal Analysis 8, 349 (1975).

21. J. Sestak, V. Satava, and W. W. Wendlandt, Thermochimica Acta 7, 333 (1973)

APPENDIX B

LARGE-SCALE MELT/CONCRETE INTERACTIONS TESTS

APPENDIX B

LARGE-SCALE MELT/CONCRETE INTERACTIONS TESTS

1. Introduction

In this appendix, experiments are described in which steel melts weighing up to 200 kg and at temperatures of about 1700°C were teemed into concrete crucibles. By these experiments the behaviors of basaltic and calcareous concretes in contact with the high-temperature melts were qualitatively compared in terms of those phenomena pertinent to questions of nuclear reactor safety. These experiments also proved to be of immense value for the identification of chemical and physical processes which are particularly influential in the development of these pertinent phenomena during the melt-concrete interactions.

The tests were conducted with masses of materials far in excess of those feasible for laboratory experimentation. It was hoped that phenomena revealed in these large-scale tests would be relatively free of "scale-effects" which might detract from laboratory-scale experimental results. The phenomena would, therefore, be more representative of phenomena associated with a hypothetical nuclear-reactor core-meltdown accident. Comparison of results from the large-scale experiments with experiments conducted on a smaller scale, such as those described in Appendix C, should indicate phenomena or processes which are particularly sensitive to the experimental scale.

A final objective of the tests was the identification of aspects of the melt/concrete interaction which merited quantification and the instrumental techniques suitable for gathering such quantitative data.

2. Experimental

Furnace-prepared melts used in these tests were formed in air with a 165-kW, 1000-Hz induction furnace, custom manufactured by Cheston, Inc. The furnace crucible material was a magnesium oxide based ceramic. Temperatures of the melt during its formation were monitored with Leads and Northrup "Dip-Tips" - Type S thermocouples sheathed in silica. When the melt temperature exceeded 1700°C, hydraulic systems were used to teem the furnace contents into an awaiting concrete crucible. A photograph of the furnace and a concrete crucible is shown Figure B-1.
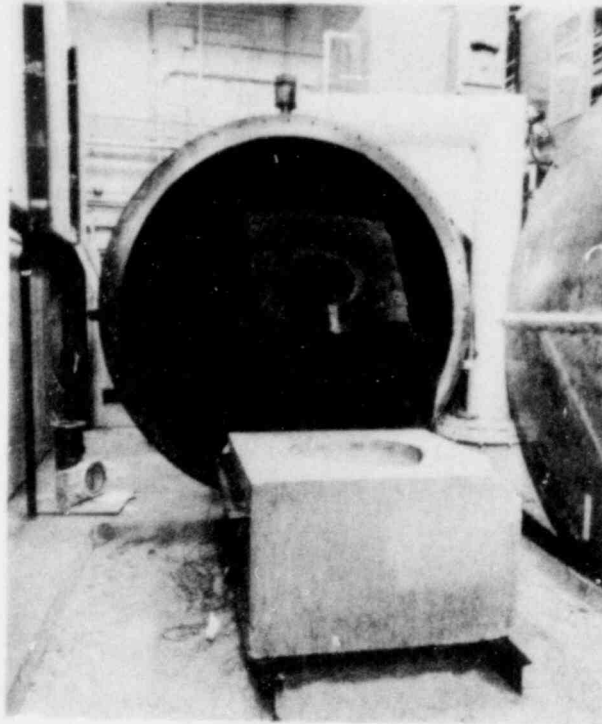
Figure B-1. Photograph of Furnace and Concrete Crucible Used in
Large-Scale Melt/Concrete Interaction Gests

Crucibles used in the tests were 42- x 42- x 26-in. concrete blocks with hemispherical cavities 12 in. in radius capped with 1.97 in. high cylinders. The concrete was reinforced with steel bar located as shown in the schematic diagram in Figure B-2. The reinforcing bar was well removed from the cavity to minimize its influence on the melt/concrete interactions. The thick walls (9 in. minimum) also served to minimize spurious cracking of the concrete due to features of the test aside from the melt/concrete interaction. Total weight of the crucibles amounted to about 3700 lbs.

The crucibles were equipped with nine Type K, bare junction, thermocouples located at various distances from the crucible cavity surface as indicated in Table B-1. The sensors served to monitor the penetration of the melt into the concrete and the thermal response of the concrete to the presence of the melt.

The gages were located 10.2 and 33.0 cm below the top of the crucible. Wall thicknesses at the gage locations were 23.3 and 41.3 cm, respectively.
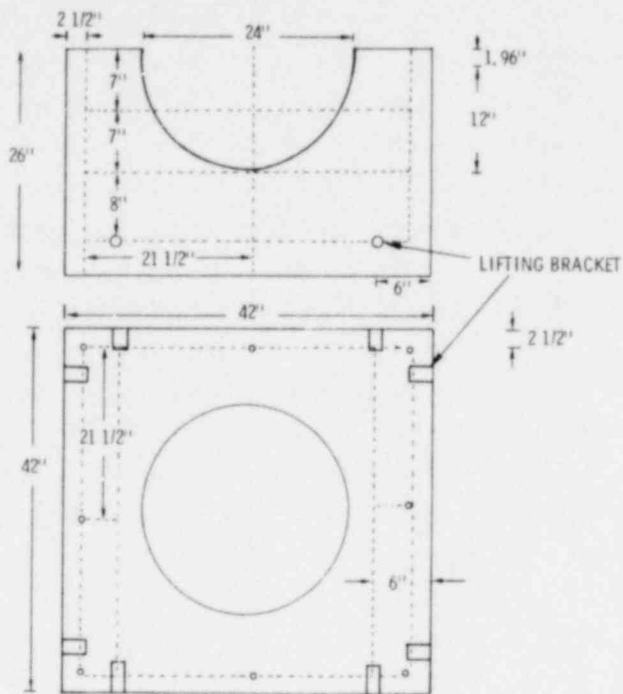
Figure B-2. Schematic Drawing of Crucibles

TABLE B-I

Vertical Thermocouple Location in the Large-Scale Tests

Thermocouple	Location Relative to the Crucible Cavity (cm)
1	3.05
2	3.56
3	4.06
4	4.57
5	4.06
6	4.57
7	4.57
8	3.05
9	3.56

NOTE: The first six of these thermocouples were located on a 12.7-cm circle concentric to the axis of the crucible cavity. Thermocouple 7 was located in the center of this ring. The remaining thermocouples were located along the crucible wall at the indicated depth.

Gas sampling apparatus used in some of the tests consisted of a 3/4-in. mild-steel probe extending over the crucible cavity to its center. The probe was connected by a 1/8-in. 304 stainless-steel tube to two Hoke, electrically-actuated, five-way valves. Each of these valves was equipped with three 150-cm^3-capacity steel bottles. Connecting lines were continuously purged by a Gast air pump. At selected times, gas bottles were opened and aliquots were extracted from the gas stream generated by the melt-concrete interaction. The samples were analyzed by gas chromatography, using a Poropak Q column temperature programmed from -50 to 120°C.

Melt/temperatures in some of the tests were monitored with immersion thermocouples identical to those used to monitor furnace preparation of the melt. Attempts were made to locate a thermocouple permanently within the melt. These attempts have been described elsewhere;[1,2] they met with little success. The combination of mechanical shock, thermal shock, and the chemical aggressiveness of the melt failed in situ sensors within seconds of the start of a test.

Attempts were made to use a scanning thermovision system to monitor heat transmission through the concrete.

Events of the tests were recorded on motion pictures taken at rates of 24 and about 400 frames per second. High-speed motion pictures were taken with negative image, which greatly assisted interpretation of the melt behavior during the tests.

Test procedure consisted of teeming the melt into the concrete crucible, observing the interaction, and then removing the solidified melt from the crucible cavity. The melt/concrete interface was then carefully mapped. In some cases thermally altered concrete materials were removed and the cavity surface remapped. The crucible was then used in other experiments. Crucibles were thus exposed as often as four times to the melts.

The procedure of repetitive testing was used to mimic, approximately, the melt/concrete behavior that would occur if the melts were sustained at temperature for prolonged periods. The procedure also allowed investigation of the influence of gas evolution rates on the rate of melt attack. Tests with virgin concrete produced partial dehydration and some decarboxylation of the bulk concrete. Consequently, concentrations of species which may be thermally decomposed to yield volatile products were less and the gas evolution rates less in tests with "used" crucibles.

Maps of the crucible cavities were made by measuring the depth of the cavity surface from the crucible top on a 1-inch grid. The resulting 576 node map could be mathematically or graphically manipulated to show the downward penetration or the penetration normal to the concrete surface by the melt.

1570 146

3. Results

A summary of the tests conducted in this program is shown in Table B-II. Descriptions of the test results are presented below in three sections: phenomenological descriptions of the test events, instrumental results, and posttest analyses of the test fixtures. Experimental results and discussions of the these results are freely mixed in these sections. In general, observations described here are applicable to tests with both calcareous and basaltic concrete except where the contrary is specifically noted.

TABLE B-II
Summary of Large-Scale Melt/Concrete Tests

Test Designation	Concrete Type	Melt	Remarks
LSL-1	Calcareous	Initially 200 kg mild steel; 170 kg after test	Virgin Concrete
LSB-1	Calcareous	Initially 200 kg mild steel; 140 kg after test	Virgin Concrete
LSB-2	Basaltic	200 kg mild steel	Virgin Concrete
LSL-2	Calcareous	200 kg mild steel	Repour into LSL-1 crucible
LSL-3	Calcareous	200 kg mild steel	Repour into LSL-1 crucible
LSL-4	Calcareous	200 kg mild steel	Repour into LSL-1 crucible
LSB-3	Basaltic	200 kg mild steel	Repour into LSB-2 crucible
LSB-4	Basaltic	200 kg mild steel	Repour into LSB-2 crucible

Events of the Tests

A sequence of photographs taken from the motion picture record of test LSL-1 is shown in Figure B-3. This test was representative of all tests conducted in the experimental program.

Contact between the high-temperature melts and concrete initiated a brilliant pyrotechnic display. Flames leaped 6 ft into the air. Molten droplets 1/8 to 1/2 in. in diameter were sprayed from the crucible. The molten pool itself was vigorously agitated and splashed about by gases released from the decomposing concrete. As the melt cooled, it passed successively through these stages:

1570 147

a. The molten pool has the appearance of a vigorously boiling liquid.

b. The molten pool has the appearance of a smoothly boiling liquid; a coherent slag begins to form.

c. The slag layer begins to cool well below the pool temperature. Gases cause the edges of the pool to froth. Occasional gas bubbles escape up through the body of the pool.

d. The slag layer has formed a fairly hard crush though the interiors of the oxide and slag melts remain molten. Gases visibly escape around the perimeter of the pool. Gases escaping through the body of the pool cause the slag layer to billow up.

e. Solidification of the melt is complete; flame jets still visible at the surface of the pool.

All of these stages were observed in all of the tests conducted in this program. The duration and intensity of activity of a given stage, however, varied from test to test.
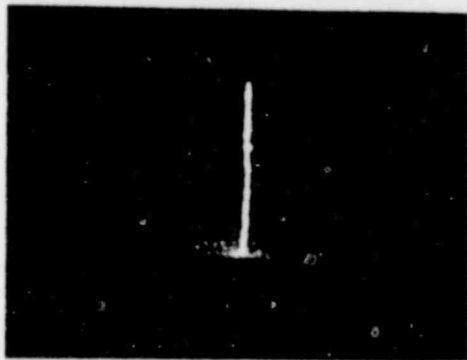
t = 1.49

t = 2.79

t = 12.79
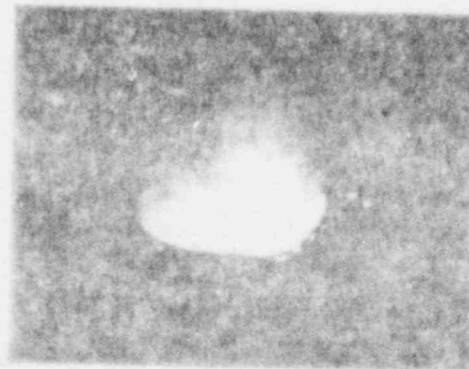
t = 17.67

Figure B-3. Sequence of Events in Test LSL-1 Taken From Camera (a) Record (Times in seconds after start of teem)

56

t = 18.32

t = 30.62
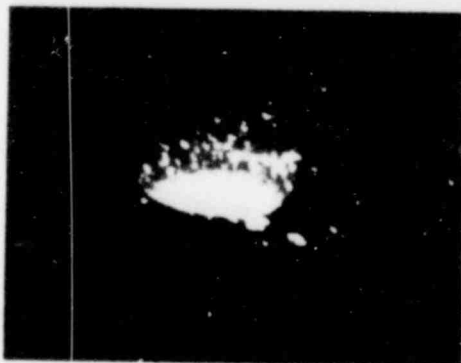
t = 56.50

t = 93.0

Figure B-3 (Cont)

Throughout those phases of the melt/concrete interaction in which melt was present, gases passed freely up through the body of the melt. A solidified layer between the melt and concrete either did not exist or was of no structural significance. Photographic records of the tests show that at times the melt may have been entirely levitated from the concrete by the pressure of the concrete decomposition gases. Levitation was, however, a rare event. Usually the photographic data suggested that a given portion of the metal at the melt/concrete interface spends time both in intimate contact with the concrete and separated from the concrete by gas bubbles. No data were extracted from the photographic records of the tests which would confirm the continued existence of a gas film separating the molten metal from the concrete.

Vigorous though the gas evolution produced in the test was, it did not seem to interfere with the density-driven stratification of the melt into a less dense oxide layer and a dense metallic layer. Such stratification occurred early in the course of a test and remained stable throughout the test. The slag layer produced in these tests had a density of 2.5 ± 0.4 g/cm^3 while the metal

phases had densities of 6.5 to 7.0 g/cm^3 in the liquid state. Such a very large density difference produces rather large rise velocities for particles of the low-density material in the high density melt. Stratification might not be so rapid nor so stable in situations where the slag and metal melts have similar densities.

The poorly thermally-conductive slag layer formed a relatively hard crust that was cool relative to the melt. It is not accurate to say the surface of the slag began to solidify since the slag is a glass. In fact, the crust, while detectable, was simply a very vicious liquid early in the test. During this time it could be readily penetrated by the immersion thermocouple probes. Eventually, the crust thickened and hardened to the point at which it could not be penetrated. Material expelled by gas bubbles escaping from holes in the crust showed that, even after this hardening occurred, oxide melt was still present within the interior of the crucible cavity.

As crust formation and melt solidification developed, small explosions occurred in tests with basaltic concrete. These explosions continued even after melt solidification was complete. In test LSB-2, a particular explosion was sufficiently powerful to elevate the solidified material several inches and turn it on one side within the crucible.

Very early in the tests with virgin concrete the crucibles cracked. In general, the cracks were vertical along the midplane of the walls of the crucibles. The cracks appeared to pass entirely through the body of the test fixture. The fixtures did, however, retain sufficient structural integrity that they could be hoisted and moved about by the support brackets mounted in the concrete. Never was it observed that metal penetrated into these cracks. This was so, even in tests with used crucibles in which the preexisting cracks in these fixtures were opened during the course of the experiments. Posttest examinations showed that the cracks were interaggregate fissures and were probably the result of thermally-induced tensile stresses created in the concrete by the presence of the melt.

Liquid water flowed from the cracks. This flow was particularly voluminous in tests with virgin concrete. In tests with used crucibles, little or no water expulsion was observed. Water migration continued for about 3 hrs. No attempt was made to collect or quantify the amount of water expelled during this period. It was estimated to be in excess of 3 qts in Test LSB-2. Visible emission of water from the fissures ended when the thermal front produced in the concrete by the melt reached the external surfaces of the concrete crucibles.

Flames were associated with all phases of all tests. Early in the tests these flames reached heights up to 6 ft and completely filled the space above the melt in the crucible cavity. The intensity of combustion declined smoothly as the melt cooled. Once solidification was complete, isolated flames up to 6 in. long continued for some time. Of course, such flames were less intense in tests with used crucibles than with virgin crucibles.

Spallation of concrete was a phenomenon associated with tests of virgin crucibles. Spallation events were detected in the high-speed motion picture records of the tests and were particularly common in tests with calcareous concrete crucibles. Spallation events occurred during the most vigorous stage of the melt/concrete interaction. Events near the surface of the molten pool were always associated with the flow and ebb of melt across "fresh" concrete surfaces. The surfaces would then erupt and thin disk-like concrete fragments were ejected at considerable velocities. A photographic sequence of one of these spallation events is shown in Figure B-4. Velocities of concrete fragments in seventeen spallation events are listed in Table B-III. The average velocity was 496±155 cm/s. There was no obvious variation in spall velocity with time during the tests. No spallation event was observed to occur at a position in which a previous spallation event occurred. Spallation rapidly waned as the availability of fresh concrete surfaces declined.

t = 12.155

t = 12.165

t = 12.188

t = 12.210

t = 12.240
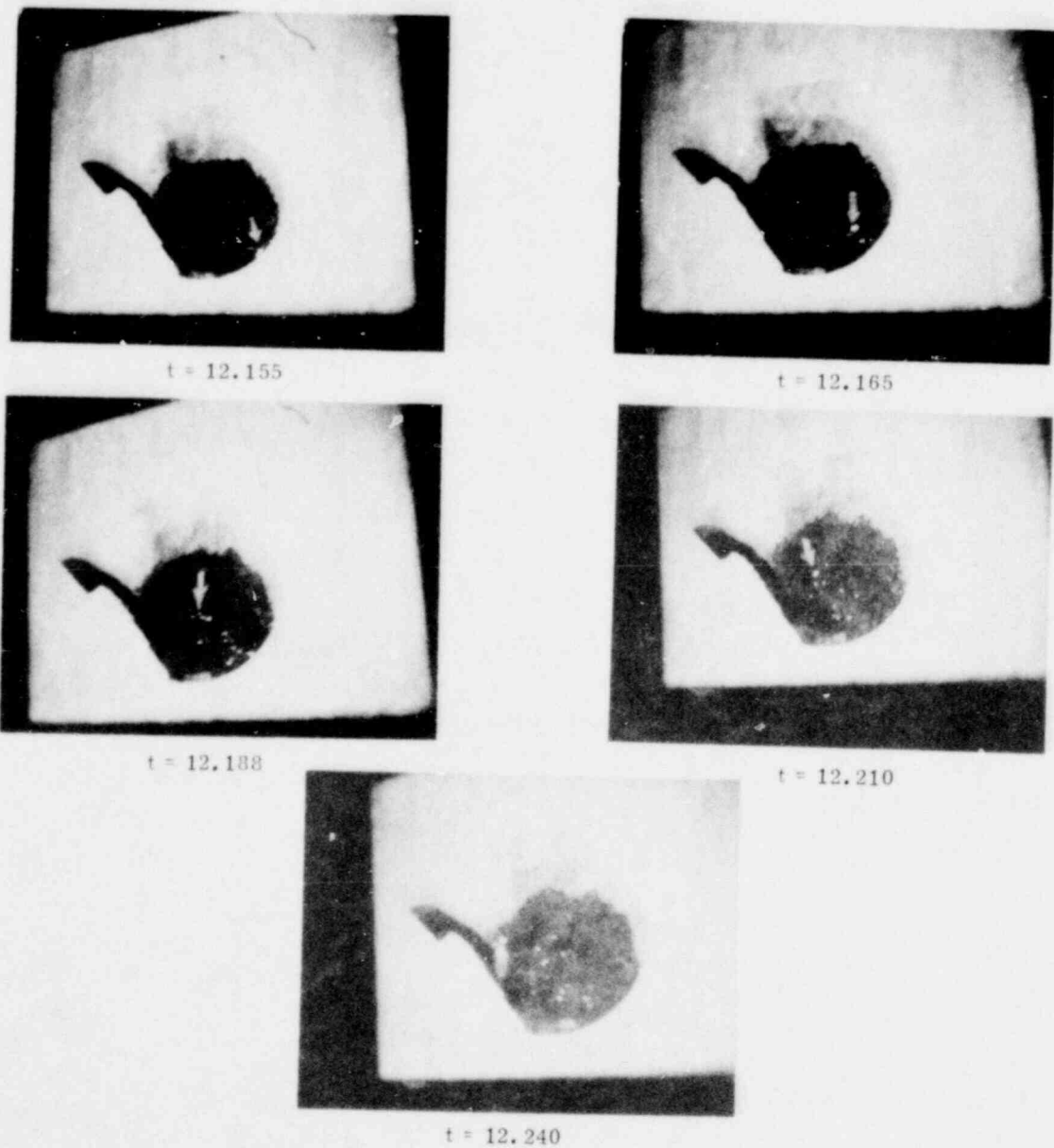
Figure B-4. Spall Event in Test LSL-1 (Times in seconds after start of teem)

TABLE B-III

Velocities of Spall Fragments in Test LSL-1

Spallation Event	Velocity (cm/s)	
1	493	
2	492	
3	562	
4	463	During Teem
5	411	
6	286	
7	774	
8	438	
9	760	
10	381	
11	364	After Teem
12	513	
13	353	
14	748	
15	397	

Mean Velocity = 496±155

Most spallation fragments fell into the melt and were destroyed. A few fragments were collected during the posttest inspection. The fragments were relatively thin plates. The plate diameters were quite variable. The thicknesses, however, were fairly uniform and could be fit to a normal distribution with a mean of 4.1 mm and a standard deviation of 1.3 mm (see Figure B-5). No fragment contained aggregate pieces larger than 1/4 in. in size.

No spallation was observed in tests with used crucibles.
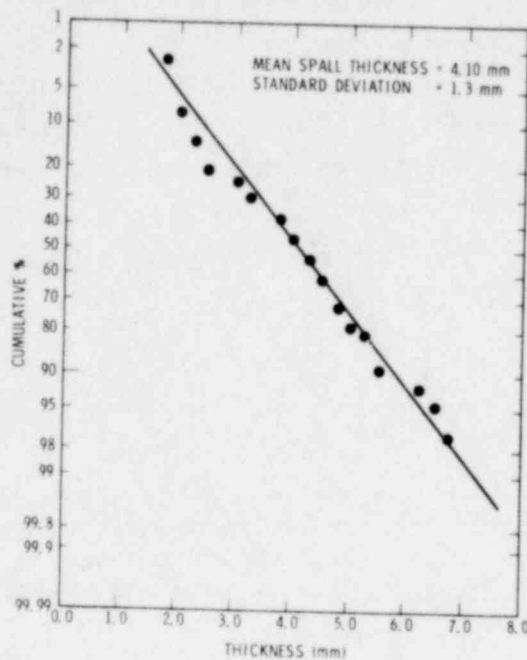
Figure B-5. Normal Probability Plot of Spall Thickness

Spallation seems to be a phenomenon associated with the surface of formed concrete. As such, it will make little contribution to the extent of erosion in a prolonged interaction between a high-temperature melt and concrete. Spallation will, however, be an important feature of transient melt/concrete interaction. Its relative importance will increase as the scale of the interaction decreases. Consequently, the contribution of spallation to observed erosion must be properly evaluated in examining results of small-scale tests.

4. Instrumental Results

Melt temperatures during the course of these tests proved to be extraordinarily difficult measurements to make. Several attempts were made to mount thermocouples at known locations within the crucible cavity. Though these sensors were heavily shielded and protected, the combination of thermal shock, mechanical shock, and the chemical action of molten metal and slag led to sensor failure within seconds of the start of a test.

Immersion thermocouples proved far more useful for determining melt temperatures. These devices were identical to those used to monitor the temperature during formation of the melt. The active length of the thermocouples was about 2 inches. They were manually manipulated. The intensity of flame, heat, and light coming from the site of melt/concrete interactions made reproducible and accurate location of the sensors within the melt impossible.

Temperature data acquired with the immersion thermocouples is shown in Figure B-6. The temperature of the metallic melt fell rapidly for the first 90 to 120 sec of the test. When the temperature reached about 1520°C, solidification of the metallic melt began and heat given off during solidification sharply reduced the rate of cooling. The solidification process lasted 3 to 4 min. Since no similar solidification process occurred in the oxide melt, there was no arrest in the cooling rate of this melt. Slag temperatures were less (sometimes several hundred degrees less) than the metal pool temperatures.
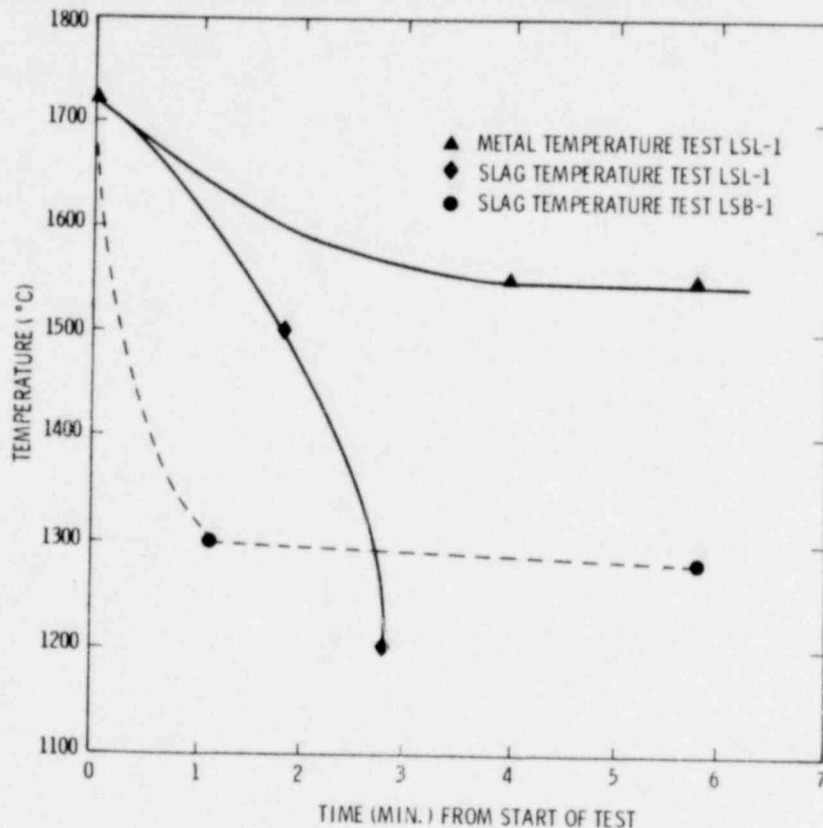
Figure B-6. Melt Temperatures in Large-Scale Tests

Examples of data provided by thermocouples located within the concrete are shown in Figure B-7. Temperature rises recorded by the thermocouples occur sequentially as would befit their various separations from the melt/concrete are marked by several arrests, many of which occur in the vicinity of known concrete decomposition reactions (see Appendix A). The arrests at about 100°C are particularly noticeable. It is tempting to assign this arrest to the loss of evaporable water from the concrete. However, alternate explanations based on the condensation of evaporable water can also be advanced. Such condensation arguments may be particularly useful in explaining data from TC-2 which was most distant of th   .ensors from the melt/concrete interface.
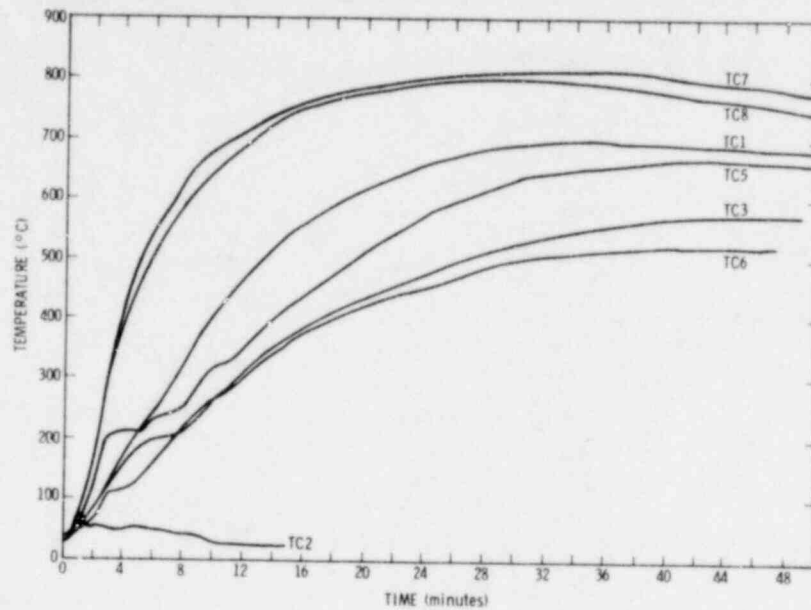
Figure B-7. Readings from Thermocouples Located in Concrete
in Test LSB-1

Useful data concerning the melt/concrete interaction would be available if thermocouple data such as that shown in Figure B-7 could be used to determine the nature of heat transfer in concrete. Early attempts to use the thermocouple data for this purpose have been frustrated by the following facts:

a. Thermocouples, by their very presence, alter the local temperature of the surrounding concrete.

b. Temperature history of concrete is very sensitive to the separation from the melt/concrete interface; locations of the thermocouple cannot be well defined.

c. Concrete is a heterogeneous material. The heterogeneity complicates analysis of heat transfer in concrete sufficiently that it is difficult to establish local temperatures in the cementituous phases where the thermocouples are located.

Data from displacement gauges mounted in the crucibles are shown in Figures B-8 and B-9. When virgin concrete is exposed to the melt, it cracks almost immediately. Growth of the crack width is apparently slow at first, probably because crack formation on other walls of crucible also influences output from the displacement gauges. After about 200 sec, crack growth is smooth and rapid ($\sim 1\text{-}2\times10^{-5}$ in./s). Growth continues even after the melt has solidified. Crack formation appears to begin at the top of the crucible and propogate downward.
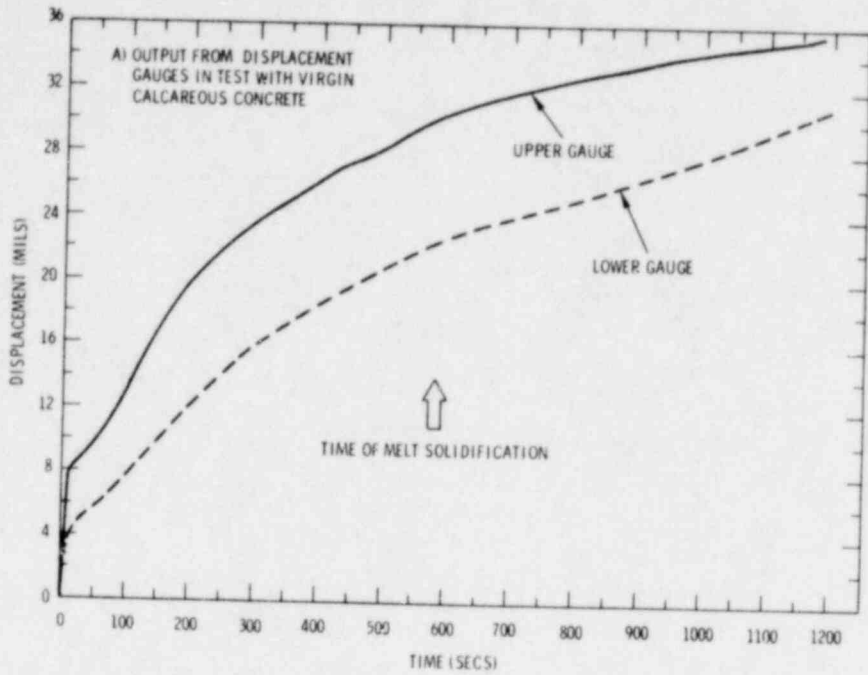
Figure B-8. Output from Displacement in Gest with Virgin Calcareous Concrete
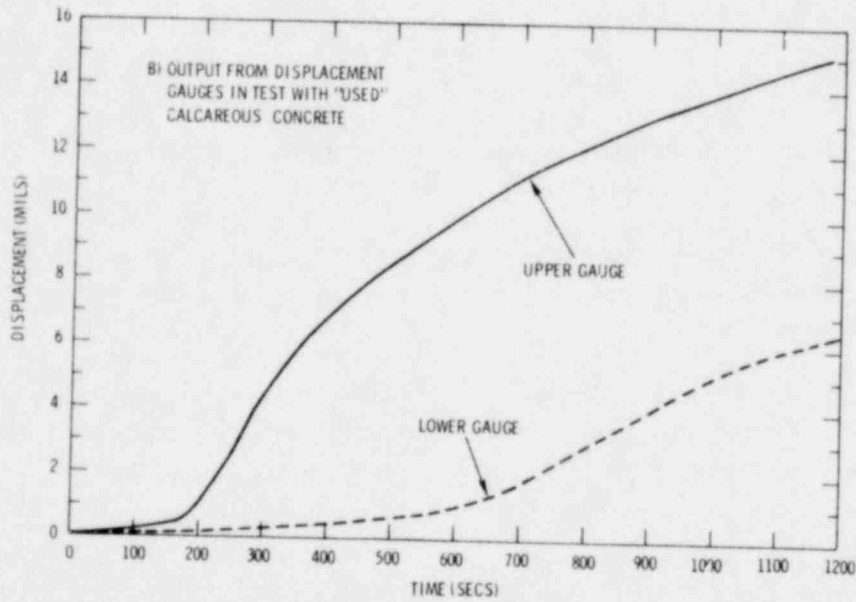
Figure B-9. Output from Displacement Gauges in Gest with "Used" Calcareous Concrete

Some additional cracks are formed in tests with "used" crucibles. But the predominant mechanical behavior of the used concrete is expansion of the preexisting cracks. As with virgin concrete, crack growth is most extensive at the top of the crucible.

Posttest inspection of the crucibles showed that the cracks passed completely through the body of the concrete. No melt, however, could be detected in the fissures. Such penetration is controlled by the melt surface tension and gas pressure in the cracks. The maximum pore size which a melt will not enter may be approximately defined by the equation:

$$d = \frac{4\gamma \cos \theta}{p}$$

where

     d = the diameter of the pore

     γ = surface tension

     θ = contact angle between melt and concrete

     p = ferrostatic pressure of the melt

Typical values for the surface tension of the metal range about 1500 dynes/cm. Since the metal does not wet concrete, θ must be at least 120°. The melt head at the bottom of the pool in these tests never exceeded 30 cm, which would give rise to a maximum pressure of 2.3×10^{5} dynes/cm^{2}. The maximum pore size which metal would not enter is then 0.13 mm. While liquid metal is present within the crucible cavity, crack widths of 0.76 mm were detected on the outside walls of the crucible. Either the cracks were not so wide within the crucible or gas pressure produced by decomposing concrete in the crack prevented the melt from entering. Posttest inspection of the lower surface of the crucible showed that metal seldom entered imperfections in the crucible cavity surface as small as 3 mm in diameter.

Gas data acquired during the tests were not entirely satisfactory. Compositions of gas samples collected in the tests are shown in Tables B-IV and B-V. In addition to gases generated by the melt/concrete interaction, the sampling probe also gathered substantial volumes of atmospheric gases. These gases were drawn in about the probe by the natural gas circulation of the atmosphere produced by the rush of generated gases from the crucible. Laboratory tests have shown that creation of a gas stagnation zone at the probe by placing a conical shield around the probe partially alleviates this sampling difficulty.

TABLE B-IV

Gas Data from Test LSL-2

Sample LSL-2	H$_2$	N$_2$	O$_2$	Ar	CO	CH$_4$	CO$_2$	H$_2$O
			Volume Percent					
V2-4	-	77.0±0.2	20.89±0.09	0.75±0.02	-	-	0.050±0.001	0.59
V2-3	-	73.0±0.5	13.52±0.07	0.72±0.01	-	-	10.27±0.08	2.5±0.7
V2-1	-	76.2(2)±0.1	15.53±0.02	0.73±0.00	-	-	6.49±0.02	0.9(5)±0.2
V1-4	-	71.5±0.4	11.58±0.04	0.74±0.01	0.12±0.002	-	13.92±0.06	2.2±0.5
V1-3	0.062±0.007	75.0±0.4	17.84±0.03	0.50±0.06	0.243±0.003	-	4.85±0.01	1.5±0.4
V1-1	-	72.8±0.7	15.3(3)±0.13	0.76±0.03	-	-	7.86±0.07	3.3±0.9

TABLE B-V

Gas Data from Test LSL-3

Sample LSL-3	H$_2$	N$_2$	O$_2$	Ar	CO	CH$_4$	CO$_2$	H$_2$O
			Volume Percent					
V1-1	0.15	74.0±0.7	11.7(5)±0.1	0.75±0.01	0.44±0.01	-	7.21±0.06	5.7±0.9
V1-3	0.052	78.8±0.1	19.8(8)±0.11	0.74±0.07	-	-	0.42±0.00	0.5(8)±0.11
V1-4	0.25±0.02	76.0±0.5	13.72±0.07	0.75±0.01	1.22±0.01	-	6.65±0.04	1.4±0.6
V2-3	-	76.5±0.4	17.20±0.09	0.75±0.01	-	-	3.42±0.02	2.2±0.5
V2-4	-	75.9±0.6	18.5±0.1	0.73±0.01	0.012	-	2.18±0.02	2.6±0.7
V2-XX	Bad threads on valve leaked, analysis showed major air with CO$_2$							

5. Posttest Examination

Photographs of a test-fixture immediately after the test, a solidified mass of melt material after it was extracted from the crucible cavity, and the melt/concrete interface are shown in Figures B-10, B-11, and B-12 respectively. The pipe shown in the pictures was driven into the melt shortly before solidification was complete.
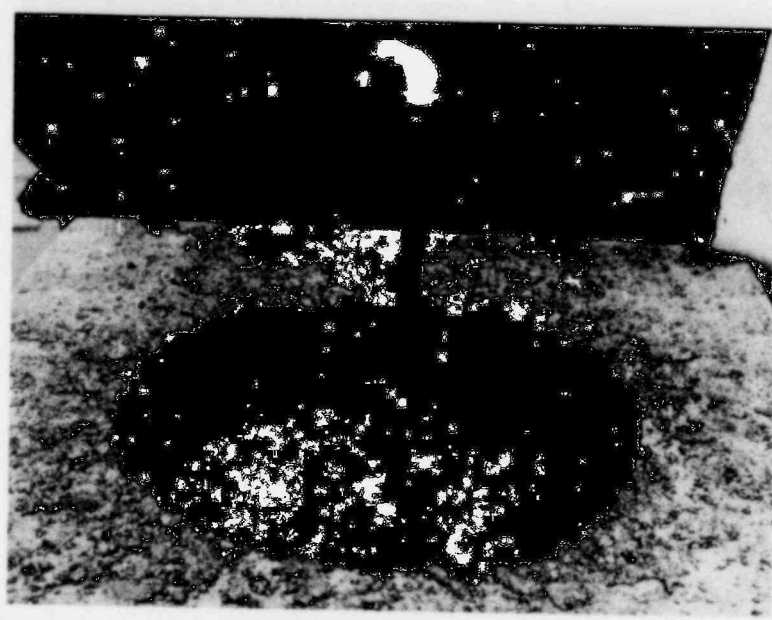
Figure B-10. Crucible and its Contents from Test LSL-1 48 Hours After the Test
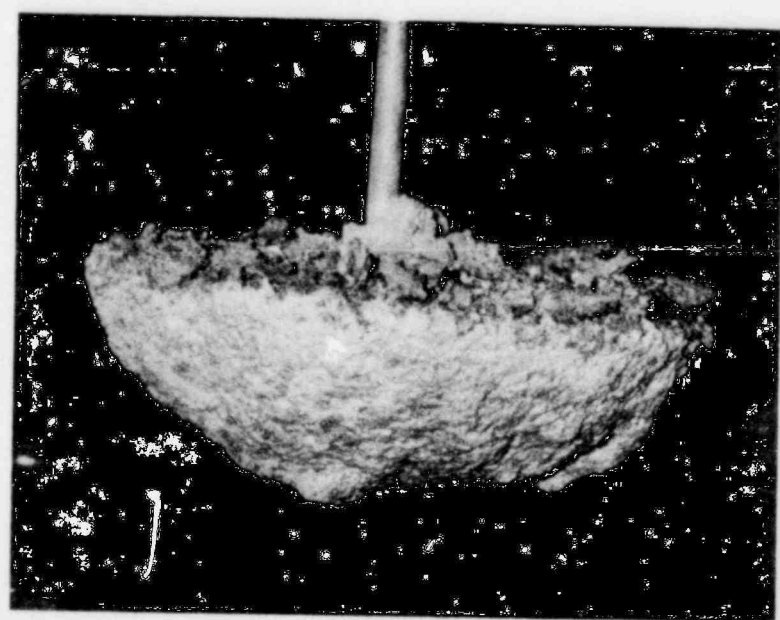
Figure B-11. Metal Slug Removed from Crucible of Test LSL-1. Weight = 142 kg.

1570 159

Figure B-12. Crucible Cavity of Test LSL-1 After Contents Have Been Removed.
Some of the black interfacial material has been removed to reveal
underlying layers.

Slag produced by the melt/concrete interaction had the appearance of fresh lava. Exterior
surfaces were quite gnarled and dark in color. The slag was glassy in nature and x-ray diffraction
seldom yielded more than a single diffuse line indicative of the oxygen lattice in the slag. Gases
escaping up through the slag had produced numerous voids and bubbles. Often the slag was sepa-
rated by these voids from the underlying metallic melt. Interior portions of the slag were often quite
colorful, especially when basaltic concrete crucibles were tested. Chemical compositions of
various slag specimens are listed in Table B-VI. Note the fairly high iron content of all the slags.
Care was taken to separate metallic iron inclusions which were often embedded in the slag prior to
analysis. The iron contents of the slags are therefore the result of melted concrete dissolving
oxidation products of the metallic portion of the melt. Coloration of the slag is obviously due to
the transition elements in the mixture. Whether these colors are indicative of the oxidation
states of manganese and iron in the melt or of the compositions of the melts is uncertain at this
time. In any case the slag is differentiated on cooling. It did not, however, precipitate crystalline
species as it cooled.

The slag adhered strongly to the concrete. The metallic portion of the melt, on the other
hand, was easily removed from the crucible cavity. The surface of the metal was covered with
a steel-blue patina. The surface was warped and pockmarked. Major undulations in the lower sur-
faces of the slags reproduced similar distortions in the melt/concrete interface. When the slag
from test LSB-2 was cut in half, it was found to contain numerous voids (see Figure B-13). The
number, density, and sizes of these voids increased near the upper surface of the slag. Also
near the upper surface were numerous slag inclusions; no slag inclusions were noted 2 in. below
the top surface of the slag. These slag inclusions greatly complicated splitting the metal slag.

Such splitting was necessary since shallow cuts near the surface of the metal would not reveal the intricate interior structure of the solidified metal.
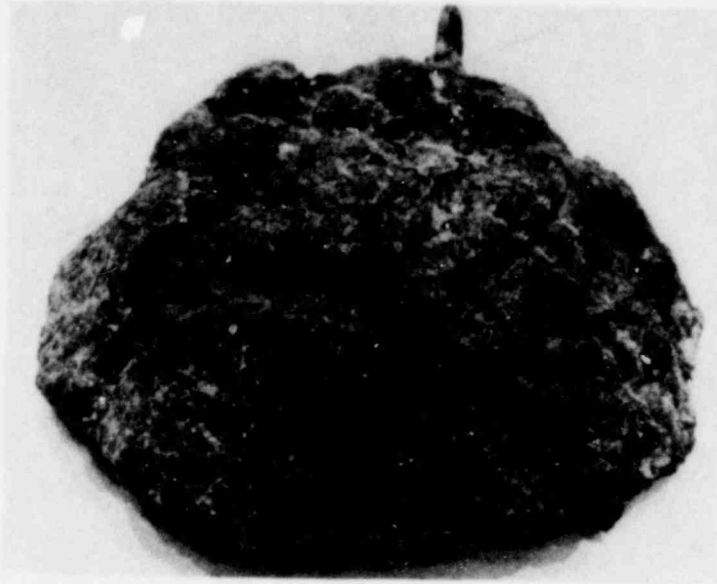
a.
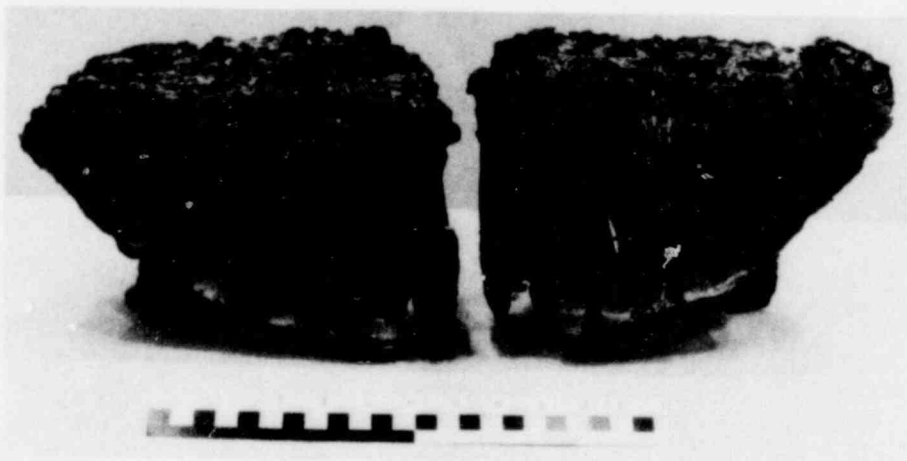
b. Sectioned

Figure B-13. Photograph of Slag Sample from Test LSB-2

The concrete/metal interfaces produced in these tests are complex structures whose essential features are schematically depicted in Figure B-14. Adjacent to the metal is a hard, glassy, dark brown material which had obviously been molten at one time. This layer was 2 to 3 mm thick in tests with both basaltic and calcareous concrete crucibles. Chemical compositions of the incipient melt zones are listed in Table B-VII. These layers were all quite rich in iron relative to virgin concrete. This was especially true in the case of tests with calcareous concrete crucibles.

TABLE B-VI

Chemical Compositions of Slags from Large-Scale Melt/Concrete Interactions Tests

Sample Description	Weight % of Indicated Constituent								
	Na_2O	K_2O	TiO_2	CaO	SiO_2	MnO	Al_2O_3	FeO	MgO
Black glass LSL-1	0.76	0.99	0.30	27.9	38.1	12.82	4.1	12.7	2.08
Slag LSB-2	1.45	2.56	0.70	13.3	52.3	9.12	6.8	10.9	3.23
Slag LSB-3	0.75	1.05	0.14	30.7	41.5	11.88	3.7	8.8	1.54
Green slag LSB-3	1.58	2.58	0.88	17.8	47.5	13.34	7.3	3.4	4.33
Brown slag LSB-3	1.57	2.69	0.92	15.4	51.0	13.08	7.6	3.68	5.47
Crust slag LSB-3 (light brown)	1.61	3.07	0.66	10.8	62.6	8.69	7.1	3.2	3.85
Crust slag LSB-3 (dark brown)	1.64	3.07	1.00	14.0	46.5	0.86	7.6	17.6	4.57
Pale green slag LSB-3, LSB-4	1.08	1.93	0.63	9.4	46.5	22.8	5.4	6.3	5.55
Blue slag LSB-3	1.54	2.68	0.93	14.7	51.1	13.85	7.8	3.8	5.78
Slag LSL-4	1.12	1.01	0.14	32.1	39.0	9.6	4.4	9.2	1.83
Dark blue slag LSB-4	1.66	2.86	0.84	15.8	55.8	8.35	7.7	4.5	4.19
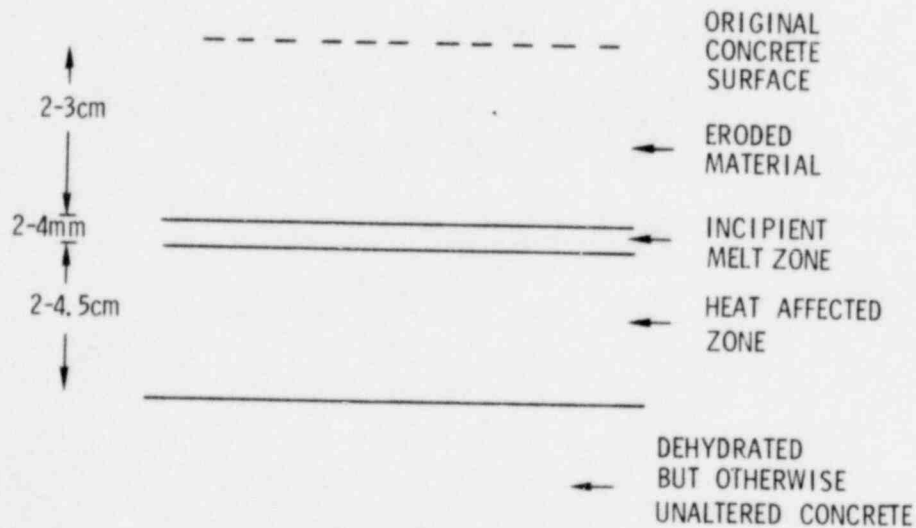
Figure B-14. Schematic Test Structure

TABLE B-VII

Chemical Compositions of Various Elements of the Melt/Concrete Interfacial Structure

Sample	Weight Percent of the Indicated Constituent								
	Na_2O	K_2O	TiO_2	CaO	SiO_2	MnO	Al_2O_3	FeO	MgO
Incipient Melt Zone, LSB-2	1.79	3.31	0.88	13.8	57.4	0.77	8.1	8.7	4.25
Incipient Melt Zones, LSB-4	1.75	3.36	1.61	12.4	60.0	0.17	7.8	9.1	3.04
Incipient Melt Zone, LSL-4	0.82	1.14	0.14	30.3	42.7	3.10	4.1	17.4	0.90
Heat Effected Zone, LSL-1	0.11	0.33	0.05	61.3	7.8	0.09	1.0	0.3	0.80
Heat Effected Zone, LSL-4	0.20	0.42	0.09	60.4	16.5	0.17	2.1	1.65	0.95
Dehydrated Concrete, LSL-1	1.19	1.81	0.15	26.6	54.2	0.43	5.8	2.7	0.71

Below the incipient melt zones were layers of powdery, thermally-altered, but not melted concrete. This material was white and rich in calcium oxide in the case of calcareous concrete. It was a light tan in basaltic concrete crucibles. This material was devoid of structural integrity. It could be easily removed with an air-driven "finger chisel". The heat-affected zone adjoined concrete which had obviously been partially dehydrated, but was structurally sound. The limits of the dehydrated zone were not easily determined and, in fact, may have extended well into the body of the crucible.

Compositions of the heat-affected zones indicate that during the melting process these zones were depleted of iron and alkali metals. Such species are obviously associated with the lowest melting constituents of the concrete.

It is likely that the interfacial structure described above was formed after solidification of the melt since the solidus temperature of the melt exceeds the liquidus temperature of concrete. The solidified melt prevented escape of the incipient melt region as obviously occurred during the melt/concrete interaction. However, it is also likely that the interfacial structure observed in the posttest examination mimics the structure present during the test. If this be so, then gases formed during the melt/concrete interaction are generated at sites well below the melt/concrete interface. These gases must then percolate up through a layer of solid concrete decomposition products to the interface. The solid decomposition products may, therefore, constrain the gases to escape from the interface at localized, albeit transient, sites. This mechanism of gas formation and transport is therefore inherently different than that involved in simulation experiments (such as water on dry-ice) which have been used to study features of the melt/concrete interaction.

Compositional data for elements of the interface structure suggest that concrete/melt formation may also begin at locations displaced from the melt/concrete interface. A reasonable rationalization of the data would hold that melting began in the cementituous phases of the concrete. This melt then dissolves the more refractory phases of concrete.

Maps of a crucible cavity surface before and after a test may be used to produce cross-sectional diagrams of the concrete penetration in terms of vertical penetration (Figure B-15), or penetration normal to the original cavity surface (Figure B-16). In either case, nonuniformities in the attack of the melt on concrete are obvious. Accelerated penetration appears near the steeply sloping sides of the crucible cavities. This phenomenon may be rationalized in terms of gas-induced circulation patterns within the melt such as those schematically diagrammed in Figure B-17. Because gases are liberated at the walls of the crucible cavity as well as at the bottom, the concentration of gas bubbles near the cavity walls is greater than at any other position in the melt. The escaping gas bubbles push liquid upward as they migrate toward the melt surface. Near the cavity walls, make-up liquid is accelerated over the cavity surface. Consequently, there is enhanced, convective heat transfer to regions of concrete near the cavity walls.

Another consequence of the gas concentration near the cavity walls is that the liberated gases partially protect the steeply sloping walls from the erosive action of the melt.

Penetration maps can also be used to calculate the volume of concrete eroded during the tests. Results of such calculations are graphically depicted in Figure B-18. Total concrete erosion in tests with either basaltic or calcareous concrete crucibles is a combination of spallation and melt-erosion. Tests with crucibles which had previously been exposed to a melt were eroded solely by a concrete melting process. As noted above, spall from the concrete had an average thickness of 3 to 5 mm. If it is assumed that spallation occurred uniformly over the virgin cavity surface to this depth, approximately 3 liters of the observed erosion was due to spallation. The balance (noted in Figure B-18 by dashed circles) was due to melting erosion.

Examinations of the data in Figure B-18 show that in tests with both basaltic and calcareous concrete the volume of eroded concrete increased with each test with a given crucible. The increase was much sharper in the test series with the calcareous crucibles than in the test series with basaltic crucibles. Further, it is noted that the melting erosion of virgin basaltic concrete is about 1.8 times more extensive than melting erosion of virgin calcareous concrete. However, the extents of erosion in the two classes of crucibles at the ends of the test series are about equal.
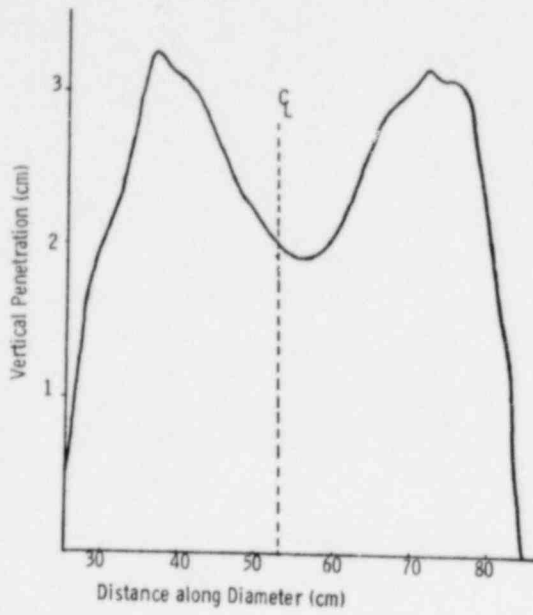
Figure B-15. Vertical Concrete Penetration by a Steel Melt in Test LSL-1.
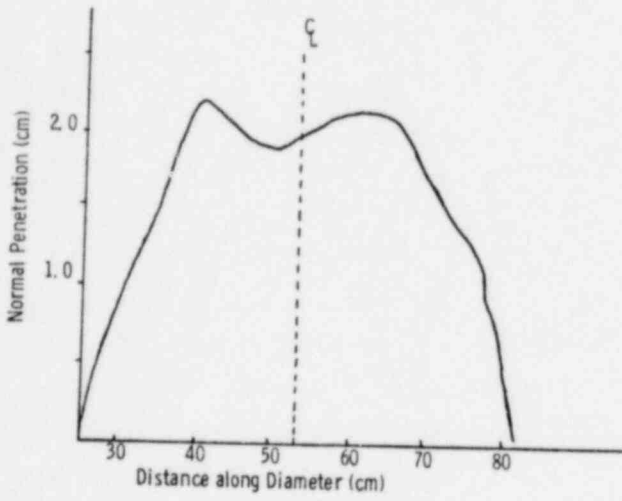

Figure B-16. Penetration Normal to the Original Concrete Surface by a Steel Melt in Test LSL-1.
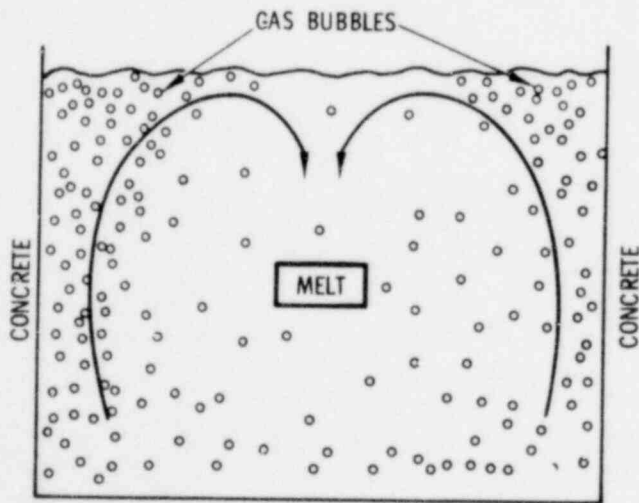

Figure B-17. Diagram of Concrete Penetration (normal to original cavity).
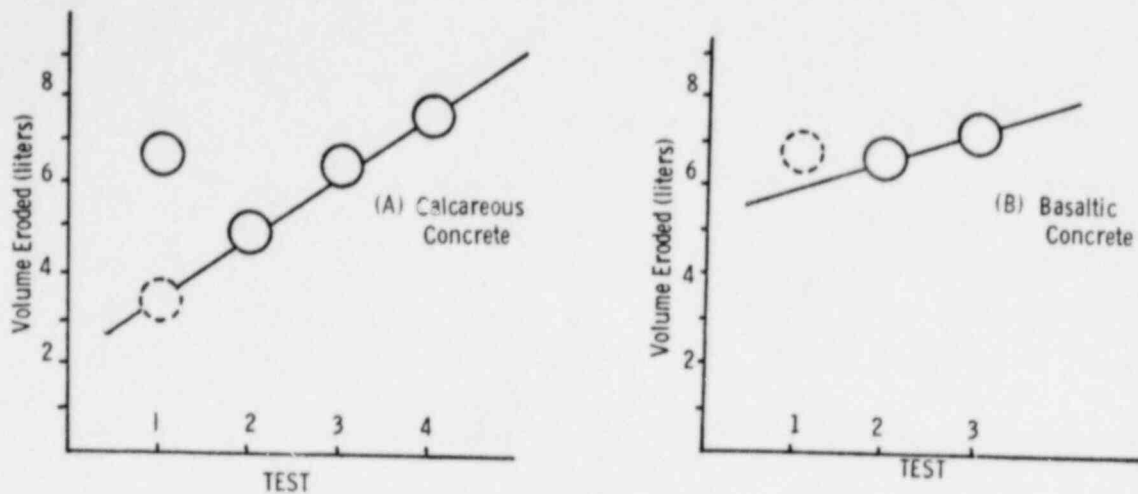
Figure B-18. Concrete Volume Eroded During Large Scale
Melt Concrete Interactions.

The above observations concerning melting erosion of concrete may be rationalized in terms of the alterations produced in the concrete during the tests. Virgin concrete is fully hydrated and carboxylated. The heat treatment received by the concrete during its first exposure to the melt leaves the concrete used in subsequent tests partially dehydrated and decarboxylated. Consequently, the volume of gas produced by the erosion of a unit volume of concrete decreases over the course of a given test series. Absence of these thermally-decomposable species reduces the amount of heat required to raise concrete to its liquidus temperature. Absence of the volatile decomposition products also affects heat transfer into the concrete. Concrete erosion by a metallic melt which does not significantly dissolve nonvolatile concrete decomposition products is due to transfer of heat from the melt into the concrete. Anything that interferes with this transfer of heat will retard the melting erosion of concrete. The rate of heat transfer across a gas bubble formed at the melt/concrete interface will be far lower than the rate of heat transfer when the melt is in intimate contact with the concrete. Thus, as the rate of gas evolution decreases, the rate of heat transfer and, therefore, melting erosion of concrete increases. This, as indicated above, is exactly what happens during the test series with the crucibles. Partial dehydration and decarboxylation of the concrete result in lower gas generation rates and more extensive concrete erosion.

Escaping gases also cause the upper surface of the melt to be disturbed. This causes an effective increase in the surface area of the melt. Thus, increasing gas generation rates also increases the efficiency of heat transfer from the top of the melt to the atmosphere.

74

The above arguments may be quantified and some indication of the disposition of heat from the melt into the concrete gleaned. A first crude attempt to do this was based on the following assumptions:

a. Thermochemical properties of the melt were those of iron.

b. Erosion of concrete was by melting and occurred only as long as liquid metallic melt was present.

c. The enthalpies required to melt virgin calcareous and basaltic concretes were 1380 and 925 cal/cm^3, respectively.

d. Enthalpies required to melt partially-thermally-altered concrete were 1000 and 820 cal/cm^3 for calcareous and basaltic concretes, respectively.

e. Heat passing from the liquid metallic melt into the concrete was totally consumed in melting concrete.

Results of the calculations based on these assumptions are shown in Figure B-19. The fraction of sensible and latent heat available in the molten pool which passed into the concrete increased over the test series. With calcareous concrete, this fraction increased from about 25% in the test with virgin concrete to 40% for the final test with the crucible. Partitioning of heat into basaltic concrete was nearly constant at about 30%.
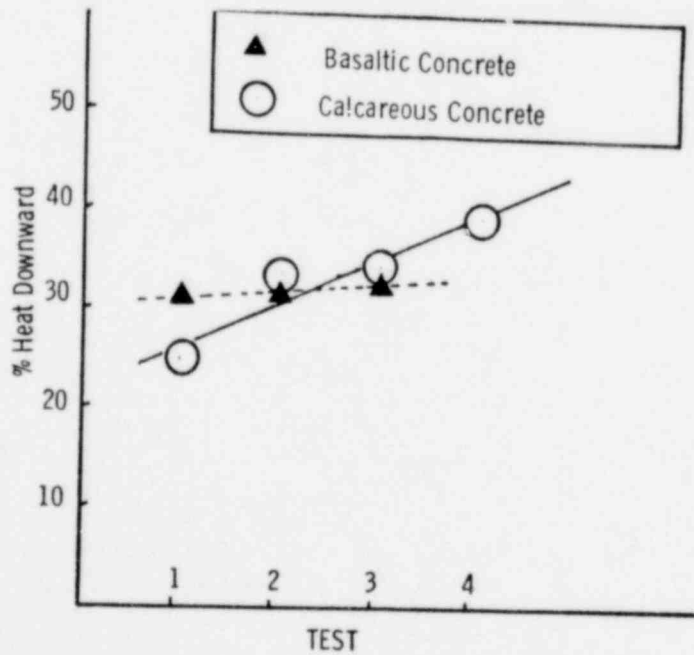
Figure B-19. Percent of the Latent and Sensible Heat in the Steel Melts Eroding Concrete.

The surface area of the molten pool adjacent to the concrete was about 1.6 times the surface area of the pool exposed to the atmosphere in the tests. Consequently, the ratio of heat flux from the melts into concrete to the upward heat flux ranged between 0.21 and 0.42. The rate of heat transfer then can be estimated to be between 2 and 4 $cal/cm^2/s$. The heat transfer coefficient must then be of the order of 10^{-2} $cal/cm^2/°C/s$.

The above estimates are very crude and reflect the need for more refined analyses of the tests. They do indicate the order of magnitude of heat transfer processes occurring in the tests and the phenomena of importance in the melt/concrete system.

References

1. D. A. Dahlgren, Ed., Light Water Reactor Safety Research Program Quarterly Report, January-March 1976, SAND76-0369, Sandia Laboratories, Albuquerque, NM, Sept 1976.

2. D. A. Dahlgren, Ed., Light Water Reactor Safety Research Program Quarterly Report, April-June 1976, SAND76-0677, Sandia Laboratories, Albuquerque, NM, Feb 1977.

APPENDIX C

SMALL-SCALE MELT/CONCRETE INTERACTION TESTS

APPENDIX C

SMALL SCALE MELT/CONCRETE INTERACTION TESTS

1. Introduction

Tests much smaller in scale than those described in Appendix B were conducted to explore the interaction of concrete with melts at temperatures typical of those expected during a light-water reactor core meltdown accident (2600-3000°C). Ultra-high temperature melts for these tests, 10 to 12 kg in size, were generated by metallothermic reactions and placed in contact with concrete of the calcareous or basaltic design (Appendix A). Like the large-scale tests described above, the small-scale tests were transient in nature since no further heating was provided to the melt once the melt-forming reactions were completed.

Objectives of the small-scale tests series were:

a. Determine, in a qualitative sense, those macroscopically observable phenomena associated with the melt/concrete interaction which would be pertinent to questions of nuclear reactor safety.

b. Determine, again qualitatively, which chemical and physical processes operative during the interaction might contribute significantly to the development of the pertinent phenomena.

c. Assess the need and feasibility of quantitatively evaluating observed phenomena or underlying processes occurring during the melt/concrete interaction.

d. Correlate results from the tests with results from the large-scale tests (Appendix B) to determine the effects of melt-size and melt-temperature on the nature of the melt/concrete interaction.

The qualitative nature of the tests planned in this phase of the experimental program precluded absolute determination of the magnitudes of phenomena observed during the melt/concrete inter-action. Instead, the tests were conducted to provide a comparison of the responses of two concrete types which were representative of concrete found in existing light-water reactors. The bases of comparison were chosen to be the rate at which melt penetrated the concrete and the nature of gases evolved during the tests.

The discussion of the small-scale test below shows that the small-scale test program has been quite successful in meeting its objectives. In particular, the feasibility of quantitatively monitoring a wide variety of phenomena occurring during the tests has been demonstrated. As a consequence, the test plans have undergone a considerable evolution toward more quantitative experimentation.

1570 170

2. Experimental Procedures

At the outset of the small-scale test program, absolutely no data were available concerning the magnitude of phenomena that might be associated with the melt/concrete interaction or the experimental procedures that might be employed to efficaciously explore these phenomena. Consequently, a considerable portion of the efforts in this program were directed toward development of experimental methods.

A summary of the small-scale tests conducted to date is presented in Table C-I.

TABLE C-I

Summary of Small-Scale Melt/Concrete Interaction

Test Code Name	Crucible Description	Melt Description	Remarks
SSL-1	Calcareous Concrete Block with a cylindrical cavity 12.4 cm dia. and 44.75 cm long	12.1 kg of iron and aluminum oxide	An unconstrained test in which a brilliant evolution of aerosol and flame occurred. Substantial ejection of melt material (~40 w/o) occurred.[1]
SSB-2	Basaltic concrete block similar in dimensions to that used in test SSL-1	12.4 kg of iron and aluminum oxide	Phenomena occurring in this test were qualitatively indistinguishable from those observed in test SSL-1.[1]
SS-1	Steel crucible; 1.25 cm wall thickness; height: 45.7 cm; diameter: 11.4 cm	10.8 kg of iron and aluminum oxide	Unconstrained test with an inert crucible to demonstrate that little of the phenomena observed in tests SSL-1 and SSB-1 were due solely to the melt-generating reaction.[1]
SS-2	Steel crucible similar to that used in SS-1	10.8 kg of iron and aluminum oxide	A constrained test whose objective was the same as in test SS-1. Only a brief emission of aerosol could be ascribed to the melt-generating reaction during this test.[2]
SSL-2	Similar to that used in test SSL-1	11.5 kg of iron and aluminum oxide and 564-g fission product mock materials	First attempt to constrain melt/concrete interaction. Within 14 sec of the start of the test, the upward heat flux from the melt/concrete interaction pierced 7 cm of steel. Once the test fixture was pierced all instrumentation was destroyed as molten material escaped from the test fixture.[2]

TABLE C-I (cont)

Test Code Name	Crucible Description	Melt Description	Remarks
SSB-2	Similar to that used in test SSL-1	10.8 kg of iron and aluminum oxide	Successful test of melt/concrete interaction with a constraining test fixture. Fixture retained melt within the curcible, channelled gases over diagnostic instrumentation and demonstrated the feasibility of quantifying the phenomena associated with the melt/concrete interaction.[3]

The initial test plan called for the conduct of tests in concrete crucibles equipped with little more than a light cover to constrain the interactions. Only the most modest instrumentation, motion picture records of the test events, and temperature sensors embedded in the concrete were to be applied to the tests. The first two tests conducted in this manner, SSL-1 and SSB-1, demonstrated that the melt/concrete interaction was indeed vigorous. The observed phenomena were more varied, intense, and pertinent than expected during the planning stages of the experiments. These phenomena created a chemical and thermal environment that threatened the integrity of any instrumentation applied to the tests. This obviated chances of acquiring data of use to the pursuit of the test program objectives. A similar test with an inert crucible, SS-1, showed that few of the phenomena were the result of the metallothermic melt-forming technique.

It was apparent that any hope of conducting a useful program of well-conceived tests rested on the ability to design a test fixture which controlled and channeled the phenomena associated with the melt/concrete interaction. Such a test fixture also offered the opportunity to derive from the tests data far in excess of that anticipated at the inception of the program. Therefore, the testing program was deferred in favor of the design, fabrication, and testing of a suitable test fixture (Test SS-2, SSB-2, and SSL-2).

The design of crucibles used in the tests is shown in Figure C-1. The crucibles are concrete blocks with cylindrical cavities 12.4 cm in diameter and 44.75 cm long. The cavity volume is about 5400 cm^3 of which 4790 cm^3 were available for the tests.

In the controlled tests an instrumentation tower was sealed to the crucible by means of a graphite compression seal developed in the course of this work. A schematic drawing of the sealing arrangement is shown in Figure C-2. A number of designs for the instrumentation tower itself were considered and tested. The design which proved most suitable is shown in Figure C-3. It consists of a lower baffle assembly (detailed in Figure C-2) which inserts into the test crucible, a 2.5-cm-thick base plate and an upper assembly of multiple sections of 12.7-cm-dia, 1.25-cm wall thickness steel pipe. The upper assembly is equipped at intervals with 0.32-cm-thick cooling fins. Elements of the assembly are connected with graphite compression seals similar to that used to seal the instrumentation tower to the concrete.
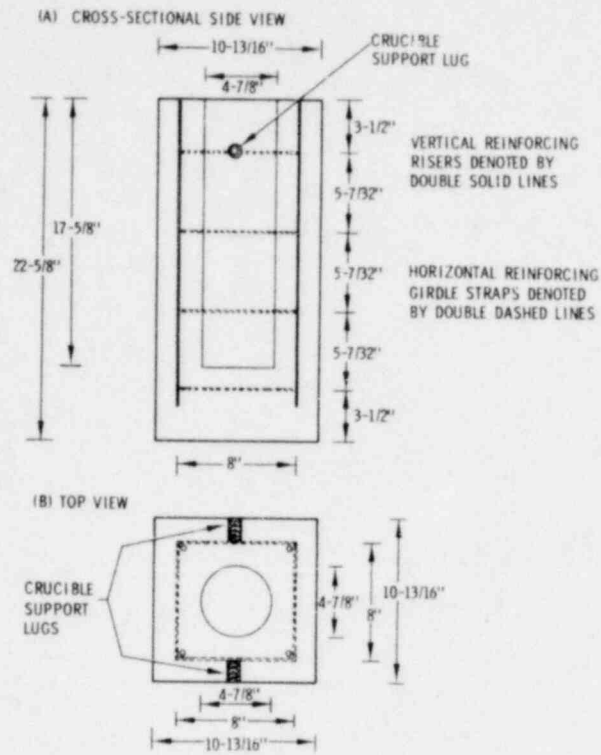
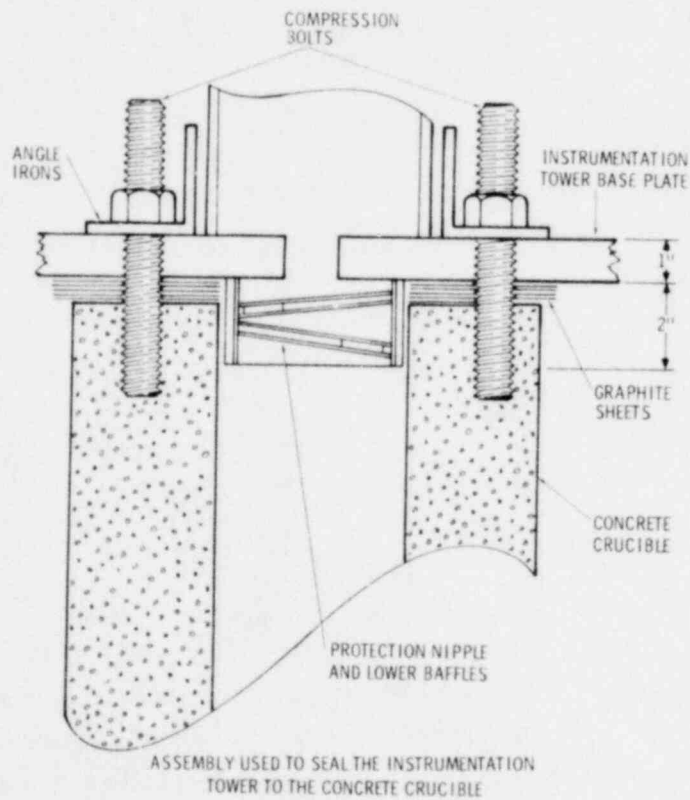Figure C-1. Design of Crucibles Used in Small-Scale Melt/Concrete Interaction Tests

Figure C-2. Assembly Used to Seal the Instrumentation Tower to the Concrete Crucible

OVERALL VIEW OF MODIFIED
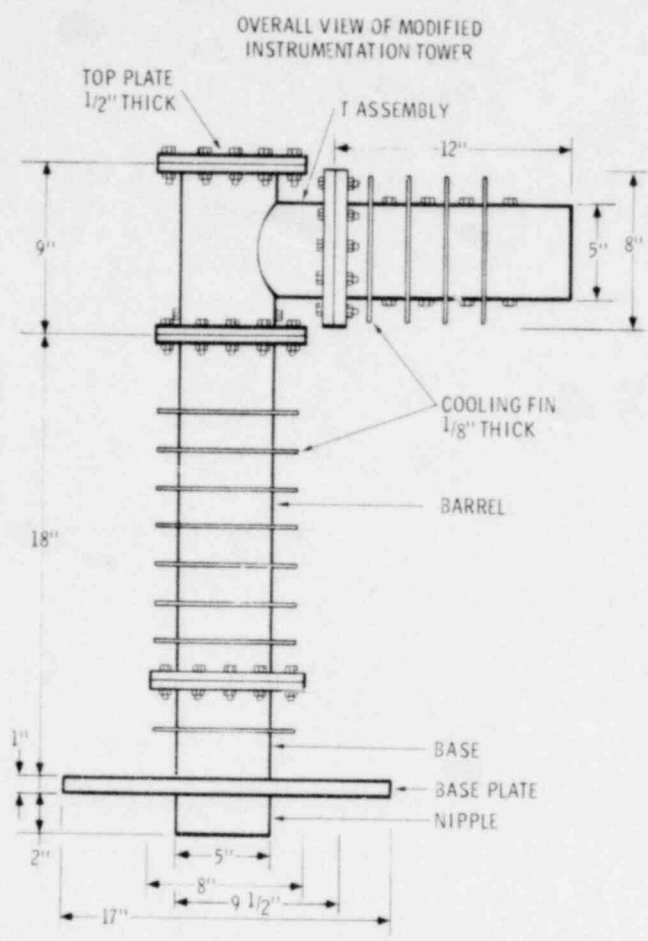INSTRUMENTATION TOWER

Figure C-3. Overall View of Modified Instrumentation Tower

Painful experience from test SSL-2 has shown that the upward heat flux generated during the melt/concrete interaction is sufficient to destroy the crucible capping assembly and instrumentation connected to it. The successful design of the instrumentation tower was therefore equipped with 14 "bristle cone" baffles, configured as shown in Figure C-4. Evolved gases from the site of the melt/concrete interaction are passively cooled by the 27 fingers on each baffle. The walls of the tower are protected by the baffle support rings.

A photograph of the completed test fixture used in test SSB-2 is shown in Figure C-5.

Melts used in the small-scale tests were generated by metallothermic reactions. To date, only iron-based melts have been used in the tests. These melts were prepared by the reaction:

$$3Fe_3O_4 + 8Al \rightarrow 9Fe + 4Al_2O_3$$

1570 174

83
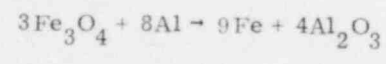
(A) TOP VIEW   BRISTLE CONE BAFFLES
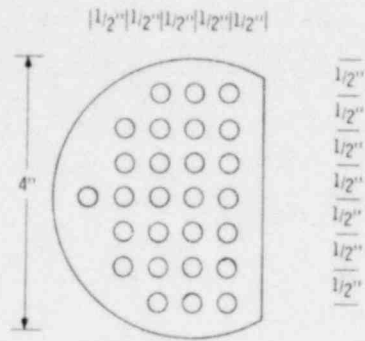
(B) CROSS-SECTION SIDE VIEW OF A BAFFLE ASSEMBLY

DIRECTION OF FLOW
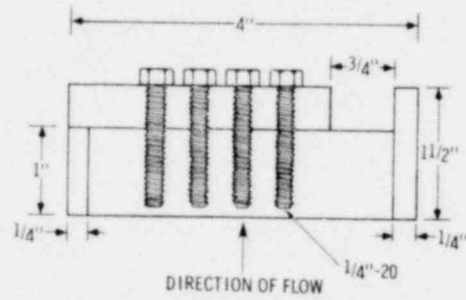
Figure C-4. Bristle Cone Baffles

Figure C-5. Photograph of Test Fixture Used in Test SSB-2

The caloric output of this reaction is 875 cal/g of stoichiometric mixture (76.3 w/o Fe_3O_4, 23.7 w/o Al) which is sufficient to raise products of the reaction to the boiling point of iron. Iron oxide (Chemalloy Grade MS-40) and aluminum powders (Alcoa atomized) used to formulate the reaction mixture are characterized by their particle size distributions determined by mechanical screening. These distributions are shown in Figures C-6 and C-7.

SIZE RANGE (MICRONS)	WT. %
106 - 75	0.021
75 - 53	11.886
53 - 45	27.716
45 - 38	22.600
0 - 38	37.754
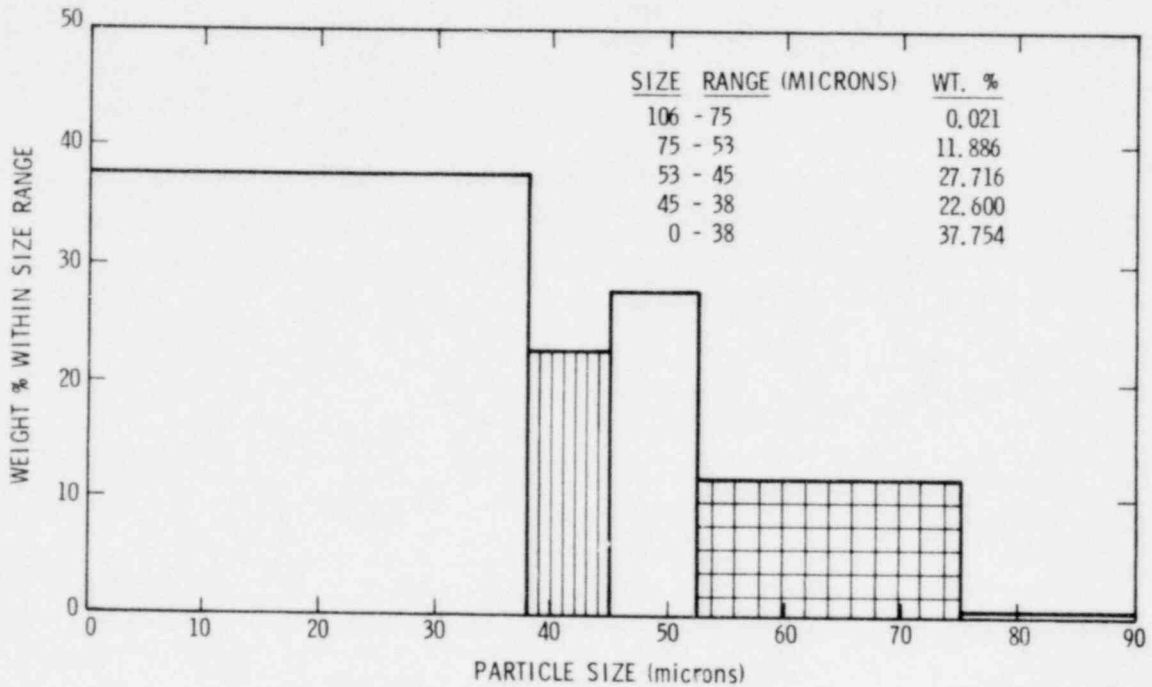
Figure C-6. Histogram of Particle Sizes in Ms-40 Magnetite
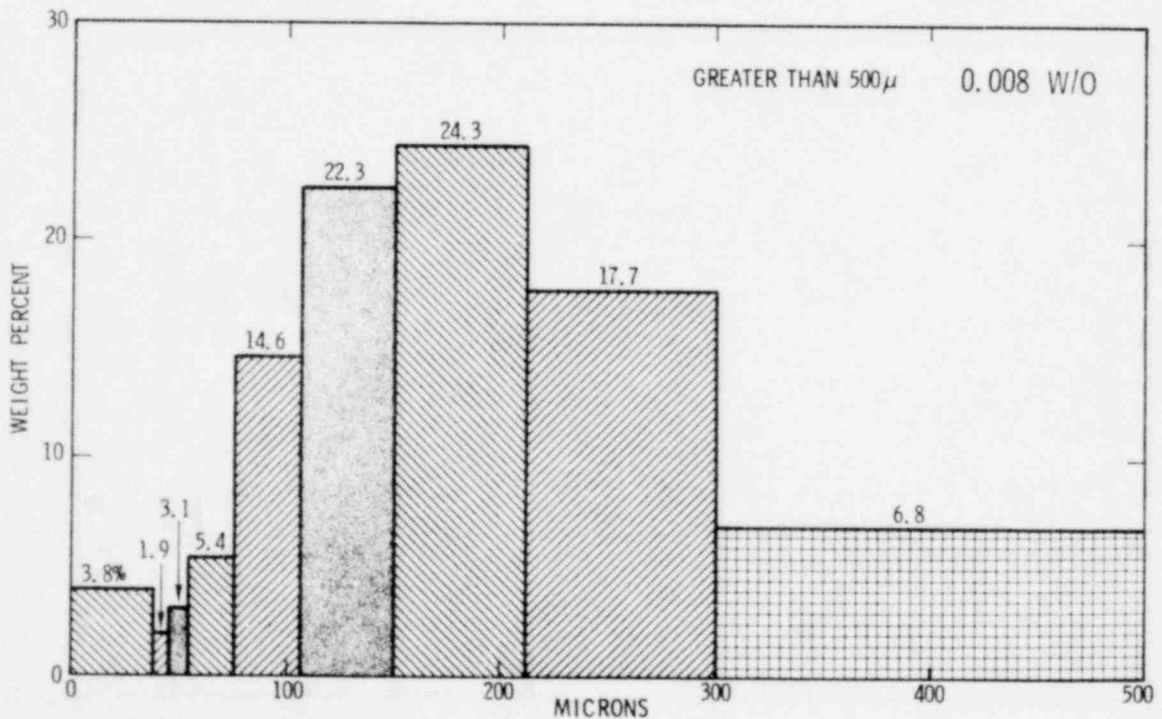
Figure C-7. Particle Size Distribution Histogram Alcoa Atomized Aluminum Powder

Occasionally, fission product mocks such as La_2O_3, CeO_2, ZrO_2, UO_2, MoO_3, and SrO have been added to the reaction mixture. With the exception of SrO, these materials were obtained from commercial suppliers and used in the as-received condition. SrO was prepared by dehydrating commercial $Sr(OH)_2$ at $750^{\circ}C$.

The metallothermic reaction was initiated by an electrically ignited Pyrofuze ignitor.[4] The reaction propagates at a rate of 4 to 5 cm/s. Consequently, melt formation was complete in these tests 8 to 11 sec after ignition.

Instruments incorporated in the tests are described in Table C-II. More detailed descriptions are to be found in Refs. 1 and 2. Results of test SSB-2 have shown that additional instrumentation may be applied to these tests since the baffle system cools the evolved gas stream sufficiently to insure the survivability of delicate sensors.

TABLE C-II

Instrumentation Applied to Small Scale Tests

Instrument	Test	Remarks
Motion Picture Records	All tests	
Displacement gauges	SSL-2	Monitor the mechanical response of concrete.
Thermocouples embedded in the concrete	All tests	Six Type K sensors which monitor both the melt penetration rate and the thermal response of the concrete.
Thermocouples on the external wall of crucible	SS1-2 SS-1 SS-2	Type K
Gas samples	SSL-2 SS-2 SSB-2	Grab samples collected from gas stream analyzed by gas chromotography.
Gas Flow Meter	SSL-2 SS-2	Turbine flow meter orliterated in melt/concrete interaction.
Gas phase temperature sensors	SSB-2	Type S and Type K thermocouples.
Aerosol sampling devices	SS-2 SSL-2	Anderson air samplers[5,6] which allow collection and particle size analysis of particulate material emitted during the test. Samples were located about fixture and consequently yielded only qualitative data concerning emission rates.

3. Results and Discussions

In order to avoid repetition and to maintain context with the wide variety of experimental data derived from the small-scale tests, results and discussions have been intermingled in this section. The results have been grouped according to the method of determination rather than by the test in which the data were gathered. Interested readers are referred to the documents cited in the listing on page 10 for detailed descriptions of specific tests.

a. Qualitative Descriptions of Test Events

The events of test SSL-1 are indicative of the intensity of the interaction between structural concrete and melts at prototypic temperatures. These events in this test are listed in chronological order in Table C-III. Photographs from the motion picture record of the test are shown in Figure C-8.

TABLE C-III

Event Sequence in Test SSL-1

| Time (sec)	Event
-4.08	Ignition of Pyrofuze
0	Ignition of reaction mixture marked by a brief flame and smoke vent through the gaps between the instrumentation tower and the crucible. Smoke begins to escape from ports in the tower.
0.92	Ignition venting completely subsided. Flame appears in one vent port in the tower.
1.08	Flame appears in three of the four venting ports in the tower.
3.46	Flame appears in all four venting ports in the tower.
4.17	First violent ejaculation of material through gaps between instrumentation tower and the crucible. Much smoke begins to form.
4.30	Ejaculation continues. Smoke and fire begin to obscure test cell.
4.37	Second ejaculation occurs. Venting of the material through gaps between tower and crucible takes on a pulsating character.
6.96	Third ejaculation. Test cell completely obscured by flame and smoke.
7.75	Fourth ejaculation.
13.59	Smoke begins to clear from test cell.
31.92	Jetting and smoking from test fixture have largely ceased. Lower portion of instrumentation tower begins to glow red.

t = -4.08
Ignition of Pyrofuze
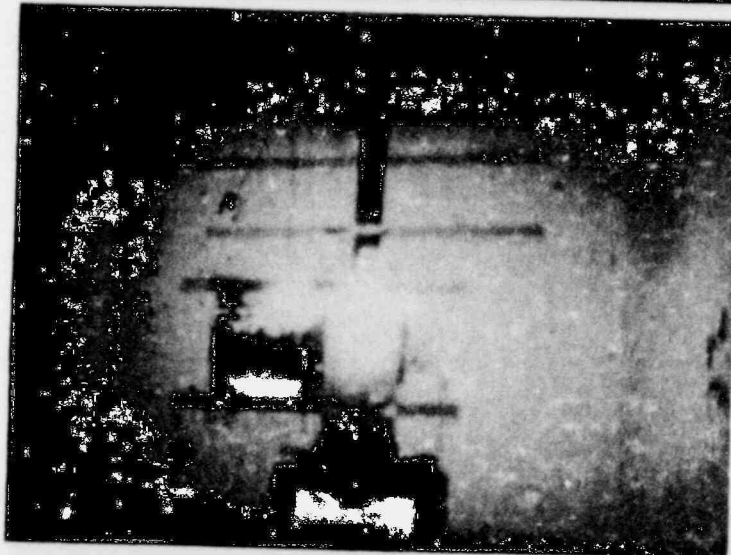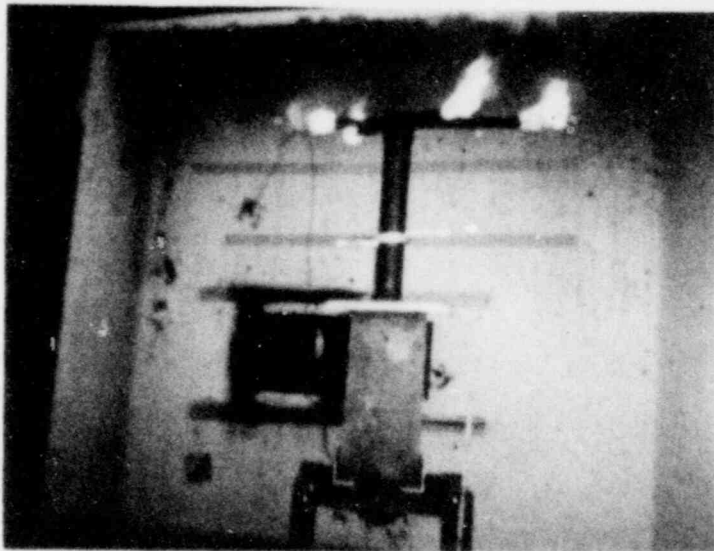
t = 0.34
Shortly after reaction
mixture ignition
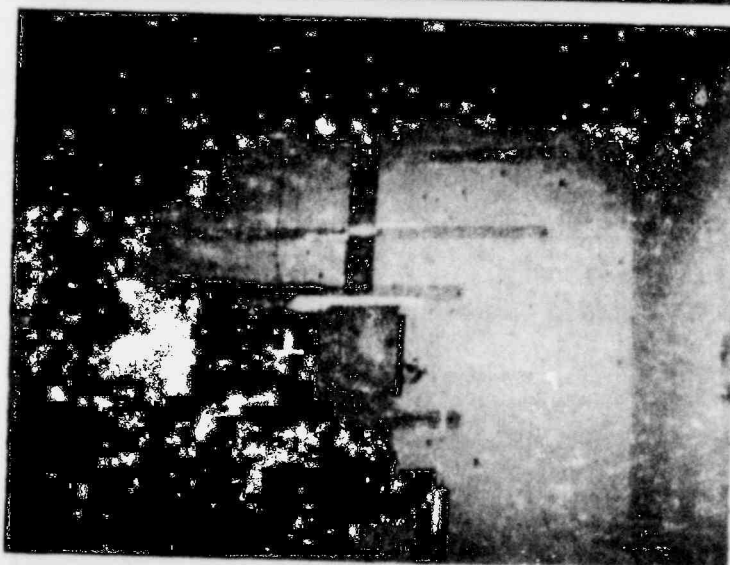
t = 0.92
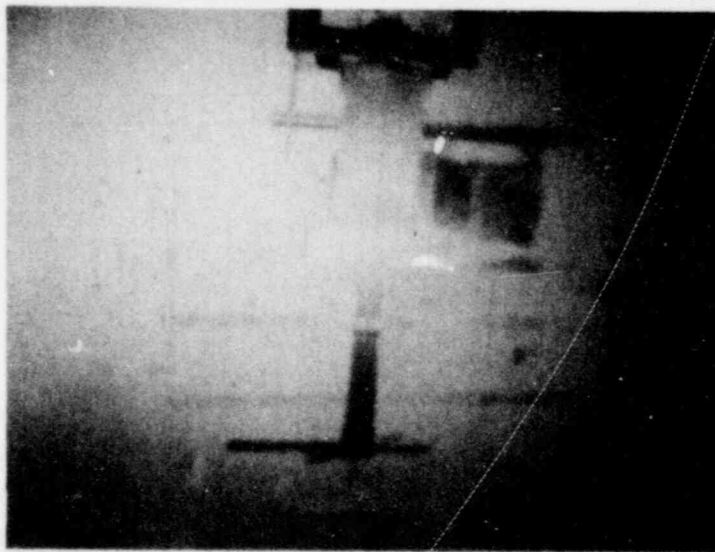Melt impinges on concrete
flame first appears in
vent port.

Figure C-8.   Sequence of Events in Test SSL-1
(Times in seconds after ignition of
reaction mixture)

1570 179
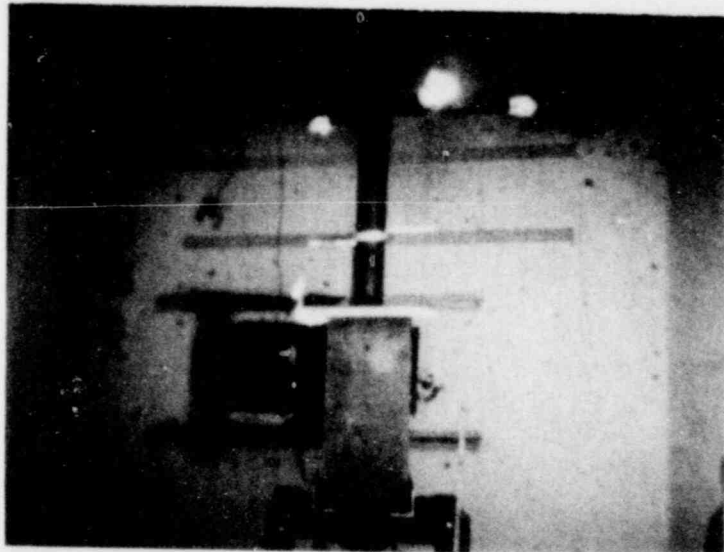
t = **1.08**
More vents ignite and
signs of venting between
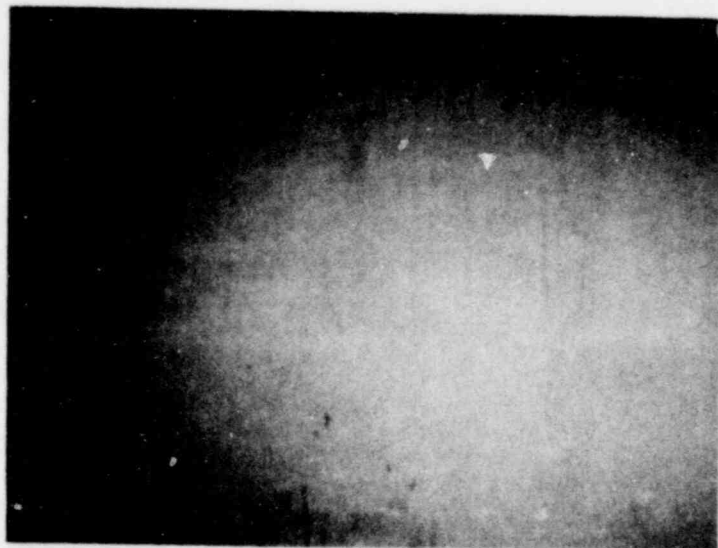instrumentation structure
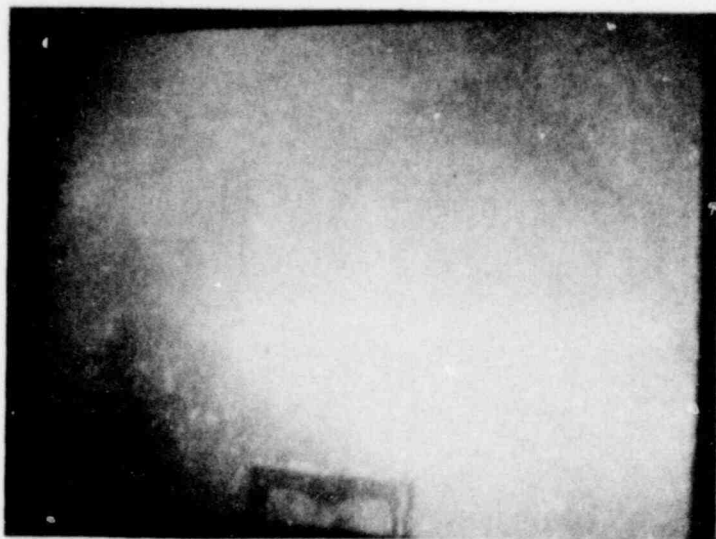and concrete

t = 3.46
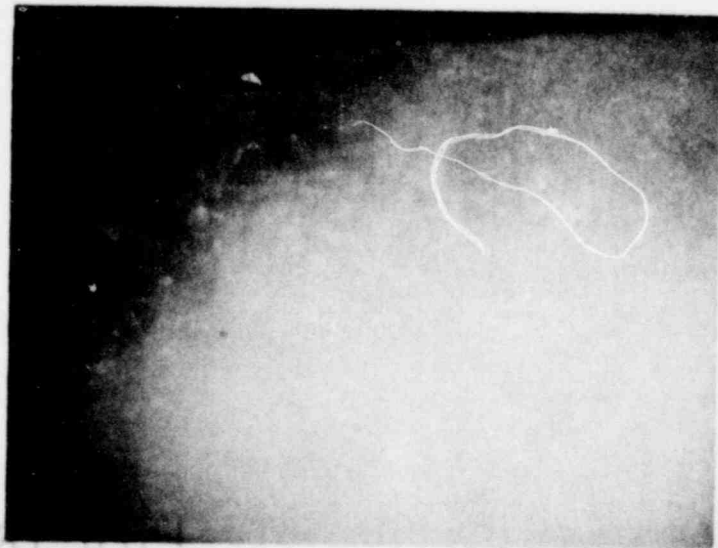
t = 4.17
Start of first ejaculation

Figure C-8 (cont)

89

t = 4.3

t = 6.96

t = 10.00

Figure C-8 (cont)

27-576
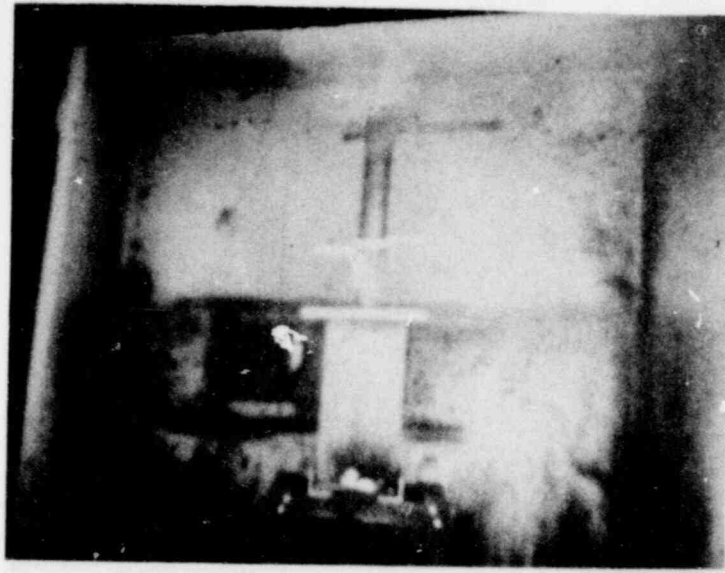

t = 13.59

t = 17.21

t = 25.00

Figure C-8 (cont)

1570 182

t = 31.92

Figure C-8 (cont)

1570 183

Ignition of the melt-forming reaction in test SSL-1 was marked by a brief burst of flame and aerosol through the gaps between the crucible and the unattached cover assembly. Dense aerosol immediately began to issue from vents in the cover assembly. Three to four seconds after ignition this aerosol was replaced by intense flames.

This relatively calm behavior came to an abrupt end when melt formation was complete and the melt impinged on the bottom of the crucible cavity as evidenced by the first response from thermocouples embedded in the concrete below the cavity bottom. The end came with an intense ejaculation of aerosol, flame, and molten material from the crucible body through the gaps between the crucible and the cover assembly. This brilliant ejection of material began 6 sec after ignition of the mixture and continued for fully 20 sec. The ejaculation from the crucible was not continuous. Rather, it was marked by pulsations as though gases evolved from the concrete were periodically interrupting contact between the melt and the concrete. The intensity of emissions from the test fixture was sufficient that the entire 9.7 m^3 test cell was engulfed in flame and smoke which completely obscured the test fixture.

The brilliant and rapid ejections of material in test SSL-1, awesome though they were, bore no resemblance to explosion. No report was heard nor was the test assembly disturbed from its pretest configuration.

Fifty seconds after ignition in test SSL-1, no further signs of active attack by the melt on the concrete could be detected. Twenty minutes after the start of the test, however, solidified melt materials still glowed red hot. Gurgling sounds similar to water boiling could be heard. The crucible body was cracked and liquid water was seeping from these cracks.

The sequence of events occurring in a similar test with a basaltic concrete crucible (SSB-1) is listed in Table C-IV. No significant differences were observed in the qualitative nature of the melt/concrete interaction when basaltic concrete was used in place of the calcareous concrete of test SSL-1.

The brilliant pyrotechnics associated with these "open" tests clearly threatened instrumentation applied to the tests and precluded conduct of useful experiments yielding interpretable data. These perceived threats proved valid when in the first instrumented enclosed test, SSL-2, insufficient cooling of evolved gases led to breaching of the containment and destruction of a majority of the instrumentation.

In test SSB-2, the melt-concrete interaction was successfully contained and the feasibility of obtaining quantitative data from small-scale tests was demonstrated. The sequence of events in this test is listed in Table C-V and photographs from the motion picture record of the test are shown in Figure C-9.
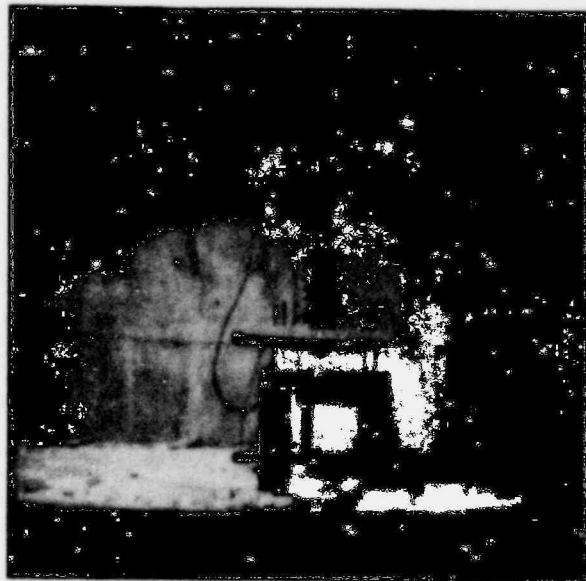
(a) White smoke emissions
    Time = 12.0
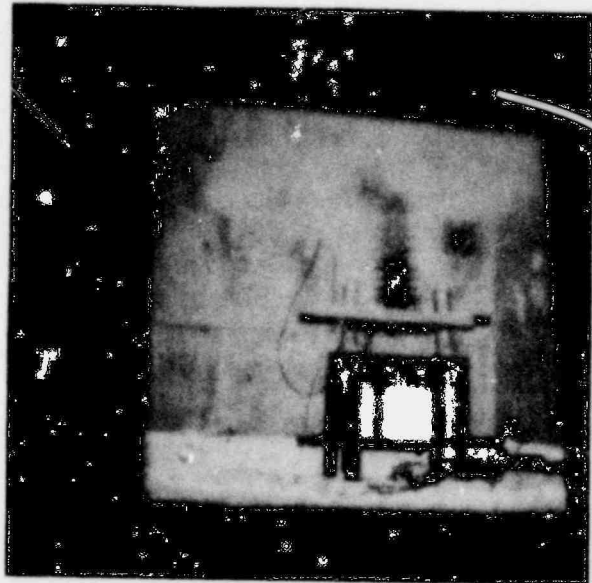
(b) Continued white smoke emissions
    emissions
    Time = 15.0

(c) Dark brown smoke emissions
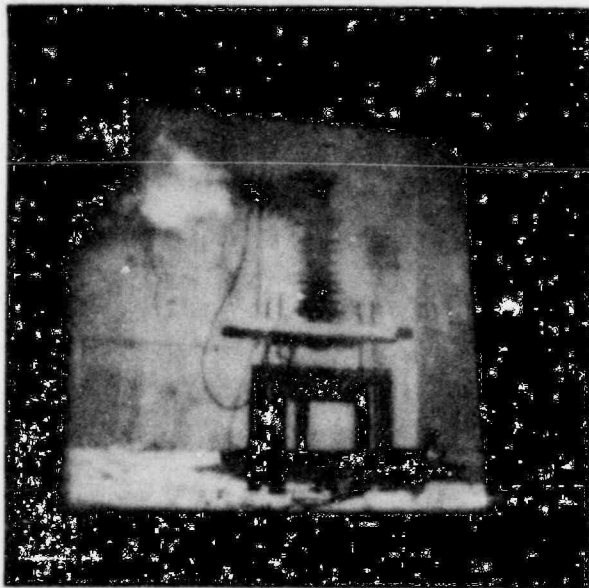   from instrumentation tower
    Time = 22.0

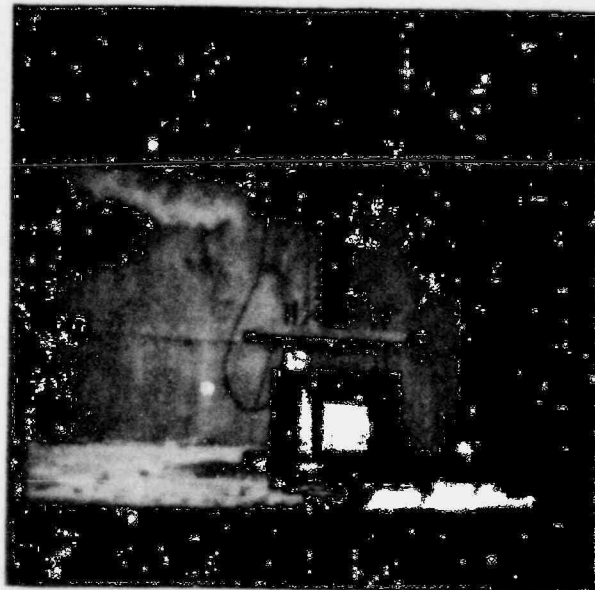(d) Streaming brown smoke
    emitted from tower
    Time = 27.0

Figure C-9. Photographs of Events from Test
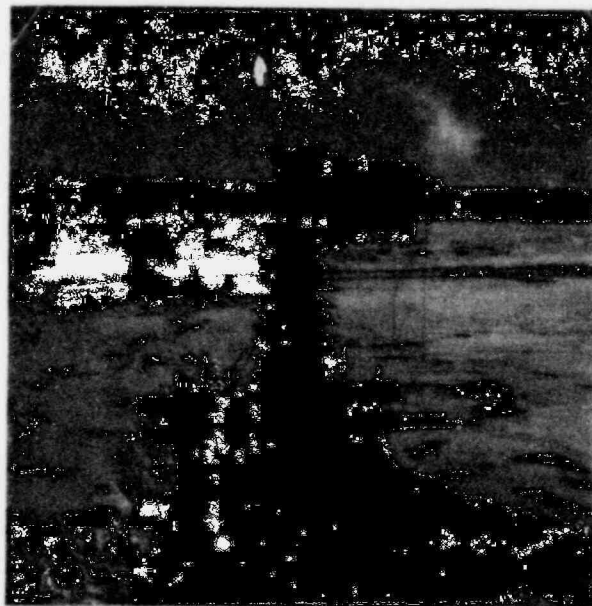(times in seconds after fuse ignition)

1570 185

(e) Flame forms in exit gas stream
Time = 32.0

(f) Well-developed flame stream exiting tower
Time = 38.0

(g) Steam escaping from test fixture
Time = 360.0

AI

Figure C-9 (cont)

TABLE C-IV

Event Sequence in Test SSB-1

Time (sec)	Event
-5.67	Ignition of Pyrofuze
0.00	Ignition of reaction mixture marked by a brief flame and smoke vent between instrumentation tower and crucible. Smoke vents from instrumentation tower ports.
3.79	Flame appears at port in instrumentation tower.
6.00	First signs of ejaculation of material through gaps between instrumentation tower and the crucible.
6.37	Flame escaping from two ports of the tower. Intense and powerful eruption of molten material through gaps between tower and crucible.
6.79	Flame escaping from three ports of the tower.
7.75	Ejaculation of material continues with great intensity. All ports in instrumentation tower are aflame.
9.08	Smoke and particulates as well as intense flame begin to occlude test cell.
11.08	Pulsation in the eruption of material through the gaps between instrumentation tower and the concrete is detectable. Test cell almost completely obscured by smoke and flame.
23.71	Smoke cloud begins to dissipate. Intense flame jets still active at gaps between concrete and the tower. Smoke still escaping from ports.
45.16	Flame jets subside though gas escape is still apparent. Little smoke obvious.

TABLE C-V

Events in the Test SSB-2

Time (sec)	Description of the Event
0.0	Fuse ignition.
6.3	Charge ignition.
11.2	Emission of white aerosol from the instrumentation tower first detected.
22.1	Aerosol emissions darken.
25	First gas sample extracted.
31	TC8 begins to respond.
31.6	Flame ignited at the exit port of the instrumentation tower.
34	Second gas sample extracted.

TABLE C-V
(cont)

| Time (sec)	Description of the Event
40.2	TC8 fails.
41	Third gas sample extracted.
46	TC5 responds.
48	Fourth gas sample extracted.
50.5	Gas stream still ignited. Cameras depleted of film.
51	TC6 responds.
55	Fifth gas sample extracted.

Onset of the interaction between melt and concrete in test SSB-2 was marked by aerosol emissions from the instrumentation tower. These emissions were light in color at the beginning of the test and progressively darkened to brown or black in color just prior to ignition of the gases evolved from the test fixture. The photographic sequence in Figure C-10 suggests that ignition of the gases was caused by hot aerosol particles.

The flame formed in test SSB-2 began as brilliant yellow in color. It rapidly paled to take on an appearance of a classic oxygen-poor hydrogen flame. Flame emissions from the test apparatus began 25 sec after the start of the test and continued for at least 30 sec. Steam emissions from the test fixture continued many minutes after the start of the test.

Concrete cracking, water migration, and sounds heard from the fixture were analogous in test SSB-2 to those observed in the unenclosed tests, SSL-1 and SSB-1.

b. Melt Penetration and Thermal Response of Concrete

Thermocouples embedded in the concrete, below the bottom of the crucible cavity, indicated a melt penetration rate of 2.3 ± 0.6 cm/min for tests SSL-1, SSB-1, SSL-2, and SSB-2. In test SSL-1 there was some indication of an initial, much higher concrete erosion rate which would be consistent with a spallation mechanism similar to that observed in the large-scale tests with limestone concrete crucibles described in Appendix B. However, in the small-scale tests no data have yet been recovered which suggest spallation occurs to depths greater than the 5 mm observed in the large-scale test. Erosion of concrete in the small-scale tests appears to be a process dominated by a melting mechansim. The independence of erosion rate on the type of aggregate used in the concrete together with results from the thermal analysis of the concrete (Appendix A) suggest that melting begins in the cementituous portion of the concrete which is similar in the two concrete types. Liquefaction of the cementituous phase then controls the rate of penetration. Overall penetration must surely be controlled by the thermochemical properties of the concrete. No experimental verification of this overall control has yet been obtained.
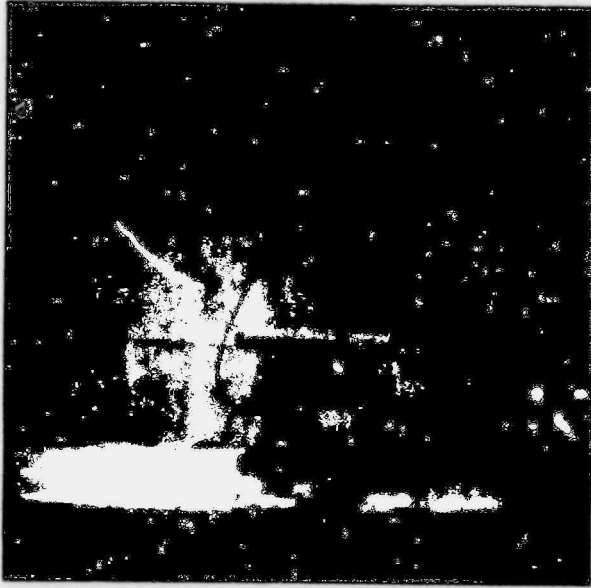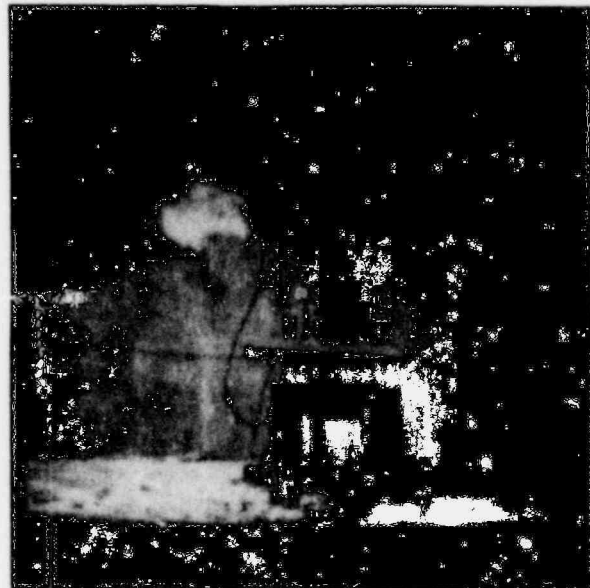
(a) First signs of incandescence
in the gas stream
Time = 31.310

(b) Flame grows
Time = 31.613

(c) Flame not yet in contact with
the exit oriface of tower
Time = 31.616

(d) Flame in contact with
the metal structure
Time = 31.619

Figure C-10.   Flame ignition in the Gas Stream
(Time in seconds after fuse ignition)

1570 189

Penetration by the melt is far from uniform. The metallic portion of the melt attacks the concrete far more aggressively than does the slag phase. Solid, concrete decomposition products are immiscible with liquid iron. Consequently, erosion of concrete by metal must be due strictly to the ability of this phase to transfer its heat to the concrete. Heat transfer from the very thermally-conductive metal phase leads to an erosion rate much greater than can be provided by the poorly conductive oxide melt. This occurs despite the ability of the oxide melt to wet the concrete and dissolve solid concrete decomposition products which should enhance erosion by the oxide melt.

Erosion of the concrete by the metallic phase displays a curious spatial dependence. Erosion near the center of the crucible cavity is less than the erosion near the perimeter of the cavity. This is shown in the cavity contour map (Figure C-11) and even more clearly in the cross-sectional map, Figure C-12. This pattern may be rationalized if it is assumed gases evolved from the concrete create forced convection patterns in the melt similar to those schematically shown in Figure C-13. These patterns would bring hotter, faster moving melt in contact with the concrete near the perimeter of the cavity than the melt in contact with the center of the cavity.
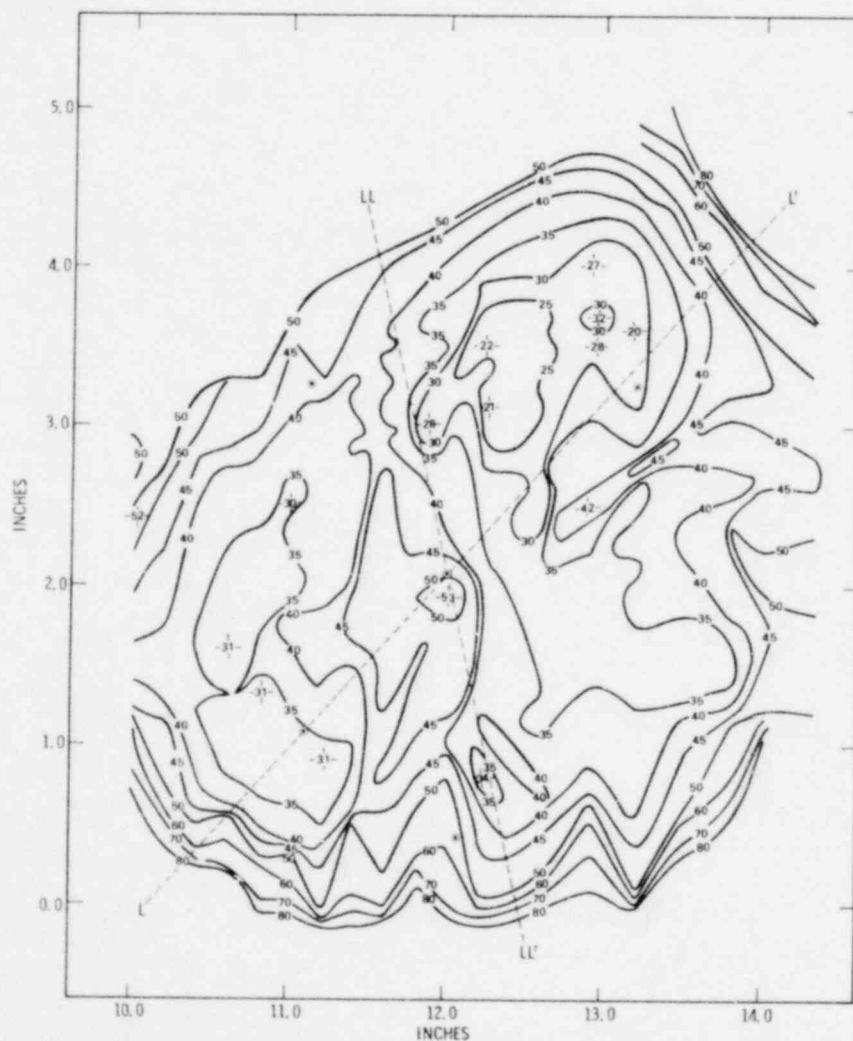

Figure C-11. Contour Map of the Metal/Slag Interface in the SSL-1 Crucible
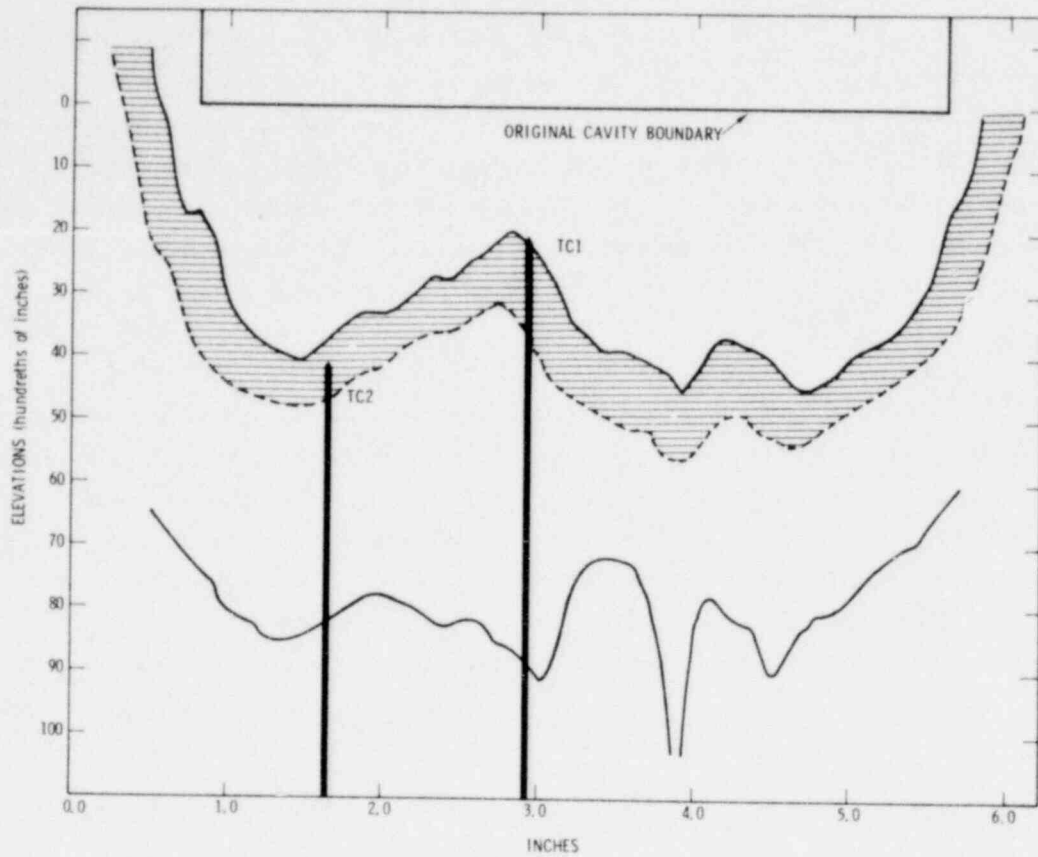
99

Figure C-12. Cross-Sectional Map of the Metal/Slag Interface in
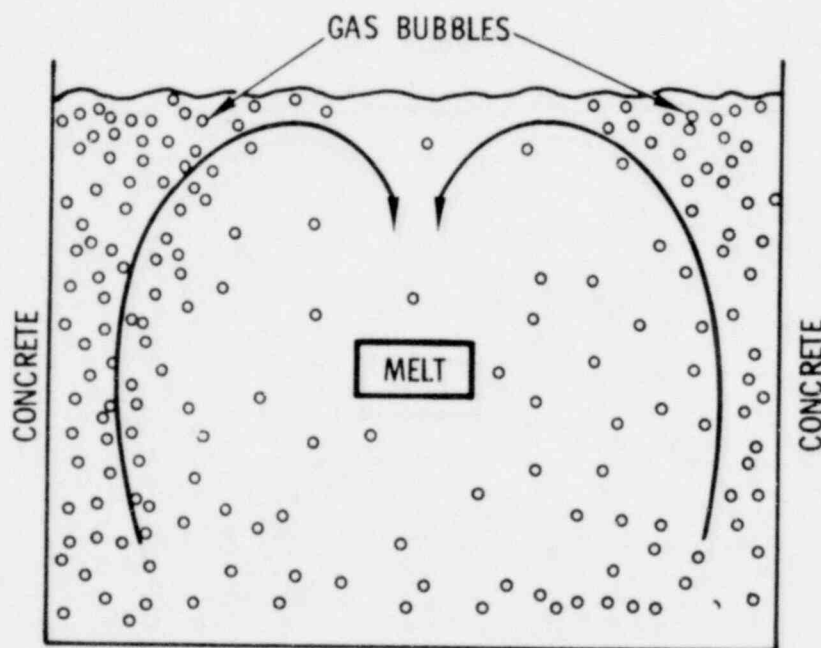the SSL-1 Crucible

Figure C-13. Schematic of Forced Convection Patterns in the Melt

Radial penetration by the metallic portion of the melt is of the same order of magnitude as the downward penetration. (Penetration by the oxide melt is exclusively radial since in the tests to date the oxide melt floats on the more dense metallic melt.) The ratio of radial to downward penetration observed in Test SSL-1 was 0.45 while that in Test SSB-2 was 0.55-0.45.

The erosion of concrete is preceded by the thermal degradation of the concrete. The many available concrete degradation reactions create a complicated melt/concrete interfacial structure (Figure C-12). Adjacent to the melt is a layer 0.2 to 0.3 cm thick of material which is iron rich and, at one point during the interaction, must have been molten. Below this incipient melt region is a layer of thermally-altered but not melted concrete. This heat-affected zone has been completely dehydrated and at least partially decarboxylated. This material is powdery and lacks structural integrity. The heat effected zone extends to a depth at least as great as the depth of erosion.

Thermocouples embedded in the concrete also indicate the thermal response of concrete to the melt. Time-temperature curves produced by thermocouples 0.5 (TC8), 1.78 (TC5), and 2.28 (TC6) cm below the original crucible cavity surface are shown in Figure C-14. The qualitative behavior of the time-temperature curves are quite similar though on different time scales as would befit their varying separations from the heat source. Each curve begins with a sharp rise to a temperature plateau at about $120^{\circ}C$. Temperature increases little for 3 to 10 sec after this plateau is reached. Then the temperature again rises sharply. TC8 is failed due to the penetration of the melt. TC6 and TC5, however, show additional thermal arrests. These arrests may be more clearly seen in plots of the time rate of temperature change versus temperature (Figure C-15). These additional arrests occur at ~450 and ~$660^{\circ}C$.
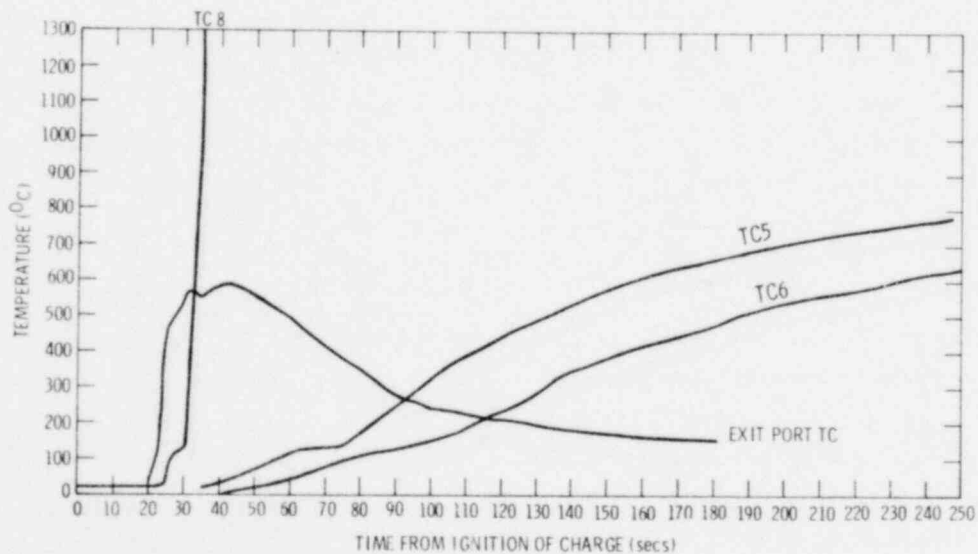

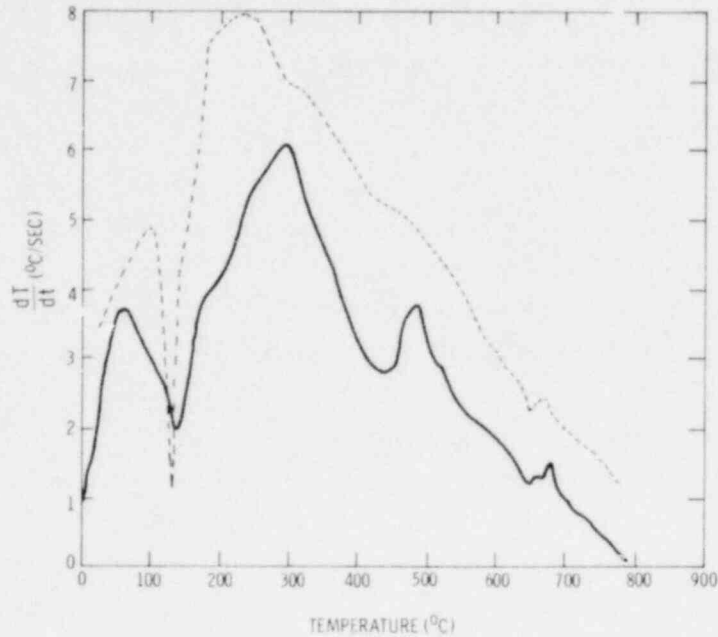Figure C-14. Temperature-Time Traces for Sensor Used in Test SSB-2

Figure C-15. Time Derivative of Temperature versus Temperature
Recorded by Sensors TC6 and TC5 in Test SSB-2

Arrests will occur in time-temperature curves when endothermic reactions are initiated. The intensities of the arrests will be dependent on the heating rate, the mass of reactive material adjacent to the temperature sensor, and the enthalpy change associated with the reaction. The thermal arrests observed in the time-temperature traces of Figure C-14 occur at locations very similar to the locations of thermal reactions in concrete (see Appendix A). Arrests at 120, 450, and 660°C may then be assigned to loss of evaporable water, loss of chemically-constituted water, and the loss of carbon dioxide from the concrete, respectively. The weak intensity of the decarboxylation arrest may be readily explained by the low heating rate at this point in the time-temperature history and the fact that the embedded thermocouples are located in cementituous material which contains only 1 to 2 w/o $CaCO_3$ rather than 20 to 25 w/o $CaCO_3$ characteristic of the bulk concrete composition.

d. Mechanical Response of Concrete

In all small-scale tests, the concrete crucibles were cracked during exposure of the crucible to the high-temperature melt. Cracking patterns developed in the crucible used in test SSB-1 are shown in Figure C-16. The cracking patterns were remarkably consistent from test to test and fairly independent of aggregate type. The patterns usually consisted of a vertical crack running the length of the crucible along the approximate midline of the face of the crucible blocks. Horizontal cracks frequently appear along the positions of girdle straps of the reinforcing steel in the crucible. The top of the molten pool may also be responsible for some horizontal cracks. In all cases the cracks are strictly interaggregate ruptures.
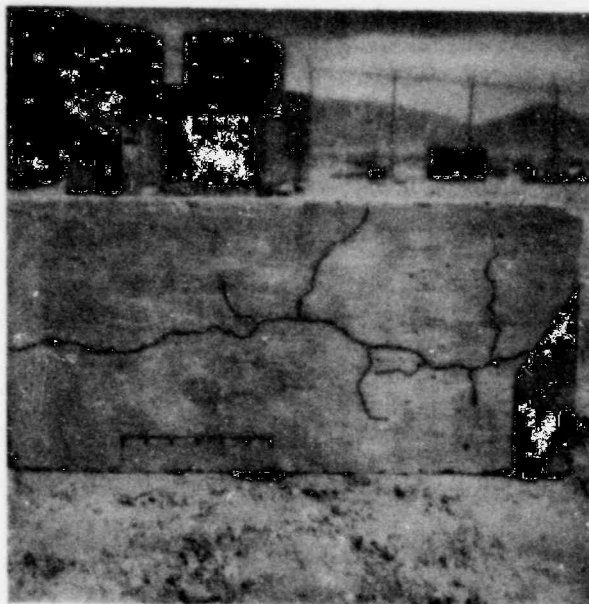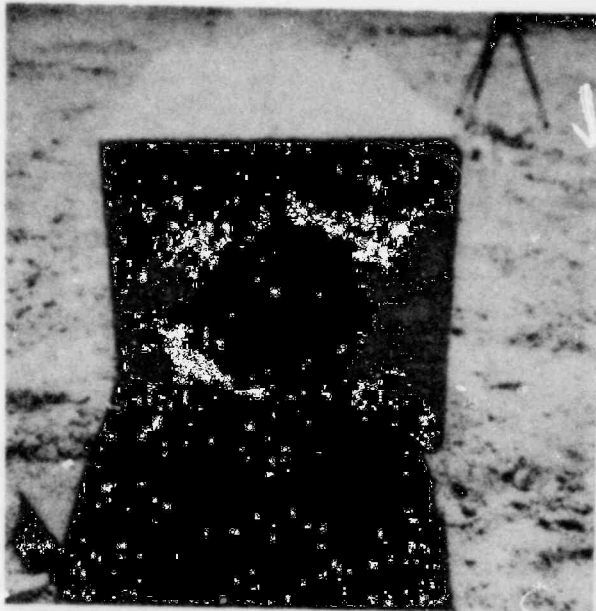
Figure C-16. Crack Patterns in the Crucible.
Patterns have been accentuated in black
visibility. The scale drawn on the side
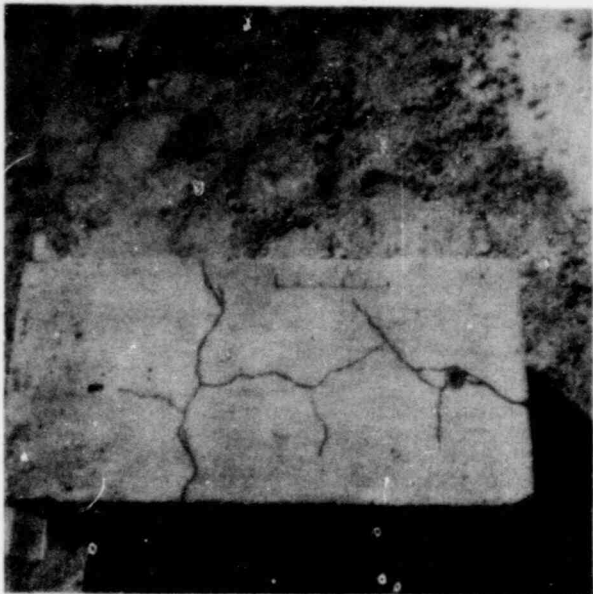of each crucible is in inches.

1570 194

103

Figure C-16 (cont)

104

1570 195

Output from displacement gauges located on one face of the test crucible indicate the cracking occurs quite early in the test (Figure C-17). The cracks begin at the top of the crucible and propagate downward at a rate of ~0.5 cm/s.
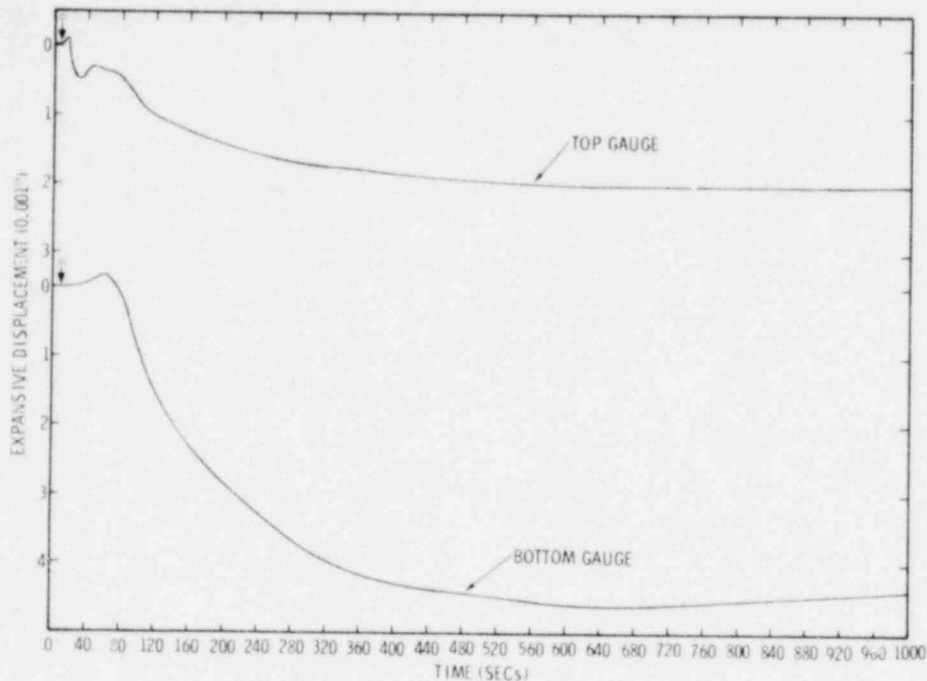

Figure C-17.   Mechanical Displacement Data from Test SSL-2 (Charge Ignition Time Indicated by the Symbol ⟊)

All data presently available indicate that the cracking is due to thermally-induced stresses within the concrete.

e.   Aerosol Emissions

Every small-scale melt/concrete interaction test has been marked by copious emissions of aerosols. These emissions are particularly dense at the beginning of the tests. There is an apparent decline in aerosol emissions when gases evolved by the concrete/melt interaction are ignited. The ability to visually detect aerosols when flames are present, however, is quite poor.

Instrumental detection of aerosol emissions was demonstrated in Test SSL-2. Anderson air samplers,[5,6] which allow collection and particle-size segregation of aerosols, were located about the test fixture. These samplers collected 2×10^{-5} to 6×10^{-5} grams of aerosol per liter of air ($2 - 6 \times 10^{-2}$ g/m^3) within the 9700-liter test cell. These values, of course, represent a lower limit to the aerosol density generated by the melt/concrete interaction.

The collected aerosols were extremely fine particulate matter. Though the collectors were not well-calibrated for the aerosol encountered in the test, they did yield data which qualitatively demonstrated that a substantial fraction of the aerosol had particle sizes less than 10μ and that the distribution of particle sizes was multimodal in nature (Figure C-18).
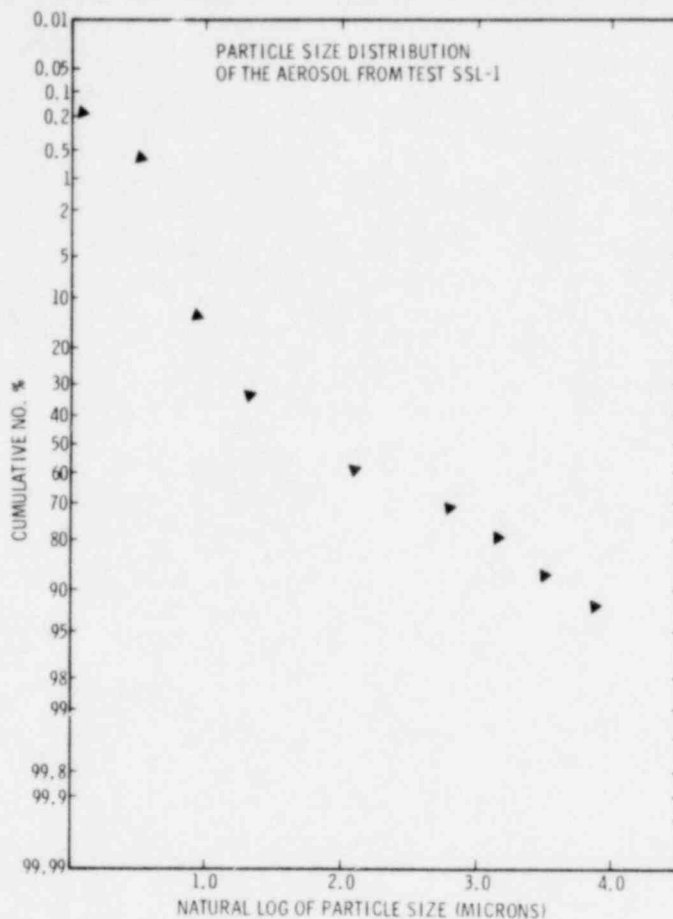
Figure C-18. Particle Size Distribution of the Aerosol from Test SSL-1

The aerosol was composed primarily of silicon oxides, iron oxides, aluminum oxides, and carbon. The carbon emissions may have been due to degradation of seals in the test fixture. However, thermodynamic analysis of gases evolved during the test show that the carbon aerosol may have precipitated from the gas phase. None of the fission products added to the melt charge (UO_2 - 0.85 w/o, ZrO_2 - 0.85 w/o, La_2O_3 - 0.85 w/o, MoO_3 - 0.85 w/o, CeO_2 - 0.85 w/o, SrO - 0.55 w/o) were detected in the aerosol. The analytic method applied to the aerosol may not have been suitable for detection of such dilute melt constituents.

106

f. Nature of Evolved Gases

The extensive baffle system built into the instrumentation tower in Test SSB-2 permitted acquisition of high quality "grab" samples from the gas stream evolved during the melt concrete interaction. These gas samples were analyzed by gas chromatography, using a Poropak Q column temperature programmed from -50 to +220°C. Results of the analysis along with the analysis of a local air sample are shown in Table C-VI. The samples listed in this table are identified by the time in seconds after the start of the test at which they were acquired.

TABLE C-VI

Gas Analysis From Test SSB-2
Volume %

Time (sec)	H_2	N_2	O_2	Ar	CO	CH_4	CO_2	C_2H_4	H_2O
25	31.8	3.20	0.68	0.011	43.84	0.007	19.86	ND	0.6
34	34.4	0.61	0.105	Tr	28.84	0.044	35.25	ND	0.8
41	32.8	0.71	0.145	Tr	51.0	0.009	14.86	0.005	0.52
48	35.4	3.91	0.97	0.015	49.27	0.028	9.71	0.023	0.65
55	38.0	16.95	4.24	0.060	38.3	0.025	2.19	0.015	0.2
"air"	ND	76.7	22.07	0.64	ND	ND	0.024	ND	0.2

Time in seconds after fuse ignition

ND = none detected

Tr = trace

The gas composition results demonstrate the highly reduced nature of gases evolved when molten steel interacts with concrete. The small amounts of nitrogen, argon, and oxygen present in the first three gas samples undoubtedly came from air trapped in the "dead" volume of the sampling apparatus. Similar gases in the fourth and fifth samples probably came from atmospheric gases diffusing back into the instrumentation tower at the low gas evolution rates near the end of the test. The O_2/N_2 ratio of the atmospheric impurities is low relative to that in the local air (see Table C-VII). This suggests that the atmospheric oxygen impurity may have reacted either with metals in the test fixtures or with the evolved gases.

TABLE C-VII

Oxygen/Nitrogen Ratios in the Gas Samples

Sample	O_2/N_2 by Volume Ratio
"air"	0.2877
25	0.2128
34	0.1721
41	0.2042
48	0.2481
55	0.2501

The results of recomputing the composition of the gas samples neglecting the above impurities are shown in Table C-VIII. The source of these gases is, of course, the thermally-induced liberation of water and carbon dioxide from the concrete. These liberated gases percolate through the melt and are clearly reduced in the process. It is of interest, therefore, to compare the ratio of hydrogen and carbon in the gases to that present in the virgin concrete. The molar ratio H_2/C is plotted versus sampling time in Figure C-19. The H_2/C ratio increases during the test. Forty seconds after the start of the test this ratio deviates substantially from that of the present in the original concrete ($H_2/C = 0.510$). It is probable that, as heat is transferred into the concrete, a point is reached at which the temperature rise created by this heat is sufficient to liberate water from the concrete but is not sufficient to decompose the more refractory limestone aggregate. Such a phenomenon would account for the increasing H_2/C ratio.

TABLE C-VIII

Gas Sample Compositions After Removal of Air Impurities

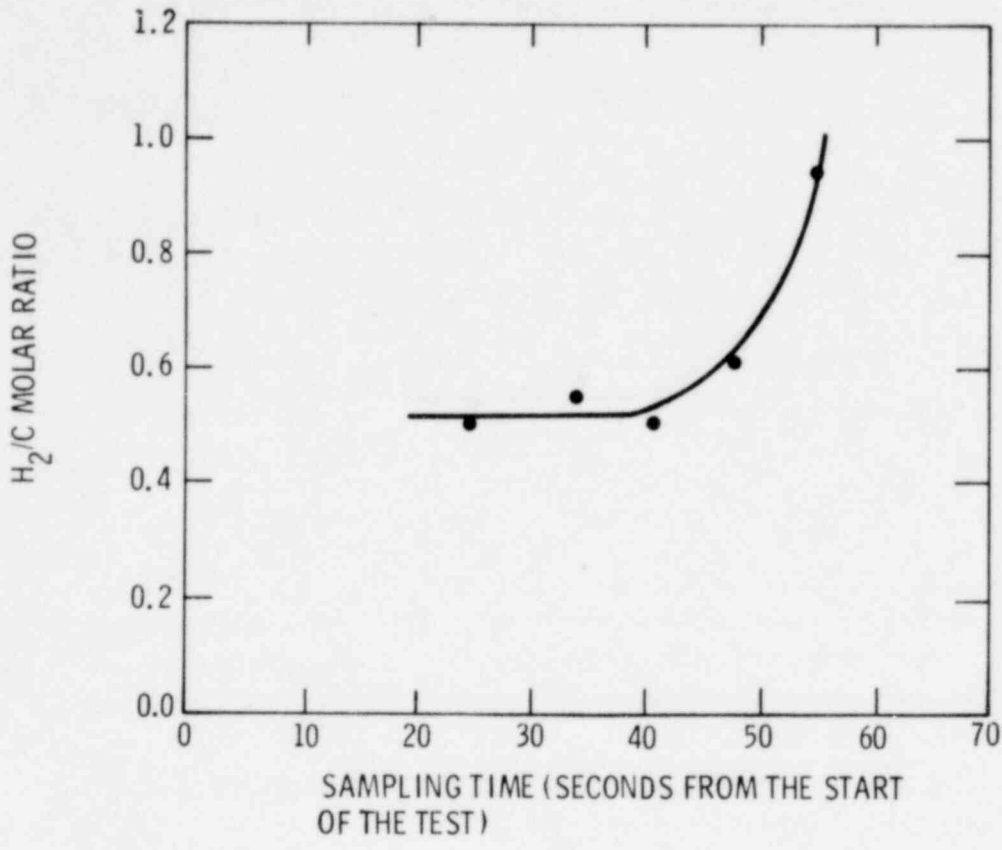| Sample Time (sec)	Volume (Percent)					
	H_2	CO	CH_4	CO_2	C_2H_4	H_2O
25	33.09	46.62	0.007	20.66	ND	0.62
34	34.63	29.03	0.044	35.49	ND	0.81
41	33.07	51.41	0.009	14.98	0.005	0.52
48	37.23	51.82	0.029	10.21	0.024	0.68
55	48.27	48.65	0.032	2.78	0.019	0.25

Figure C-19. H_2/C Ratio of Gas Samples Acquired in Test SSB-2 versus the Time of Sample Acquisition

When gases are sampled at elevated temperatures, the possibility that these gases may react with the sampling apparatus exists. Further, if the temperature at which the gases are sampled is not the same as the temperature of the gases at the source, the measured gas compositions may not reflect the source gas composition accurately. The gas samples obtained in Test SSB-2 have therefore been subjected to extensive thermodynamic analysis.[7,8] This analysis has been conducted in an effort to reconstruct the true gas compositions and derive the compositional history of the gases. Results of this analysis are briefly described below.

The computer code SPEDIS (8) was used to determine the "correspondence" temperature of each species in the five gas samples. The "correspondence" temperature is the temperature at which the calculated equilibrium concentration of a particular species in the mixture equals the observed concentration. "Correspondence" temperatures for the gas samples are shown in Table C-IX. No "correspondence" temperature could be found for the hydrogen in the gas samples over the range of 100 to $1700^\circ C$. This fact and the extreme variability of the correspondence temperatures for other constituents of the gas samples indicate that the mixtures are not at equilibrium.

1570 200

109

TABLE IX

Correspondence Temperatures (^{o}C) for Gas Samples Constituents

Sample Time (sec)	Correspondence Temperatures (^{o}C)					
	H_2	CO	CH_4	CO_2	C_2H_4	H_2O
25	-	645	905	660	ND	440
34	-	600	780	610	ND	-
41	-	675	920	680	205	470
48	-	700	905	710	150	460
55	-	775	1000	780	400	275

The gas samples extracted from the test fixture 25 and 34 sec after the start of the test have been subjected to further analysis in an effort to reconstitute the compositions of these samples when they were last at equilibrium. Inspection of the correspondence temperatures of the species in these two samples shows that CO_2 and CO must be very nearly at mutual equilibirum, whereas H_2, H_2O, and CH_4 are severely disequilibrated. Likely reactions which could lead to this disequilibrium:

Metal - Water -

$$Fe + H_2O \rightleftarrows FeO + H_2$$

Carbon deposition -

$$CH_4(g) \rightleftarrows C(s) + 2H_2(g)$$
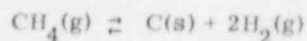
Carbon and oxygen were therefore mathematically added to the gas mixture to form H_2O and CH_4 until a uniform correspondence temperature was found for the species in each mixture. The resulting compositions of the gas alequots and their correspondence temperatures, which are also the temperatures at which the species in the samples were last at equilibrium, are shown in Table C-X. The equilibrium temperatures are entirely consistent with the circumstances of Test SSB-2. It is noteworthy that the carbon additions necessary to reconstitute the sample acquired at 25 sec and, by implication, the amount of carbon that must have been lost by the gas as it cooled are of the same order of magnitude as aerosol emissions observed in Test SSL-2.

TABLE C-X

Last Equilibrium Composition of the Gas Mixtures

Time = 25 sec sample

Species	Volume %	Correspondence Temp. (^{o}C)
H_2	23.44	810
CO	45.65	810
CH_4	0.031	810
CO_2	20.68	810
H_2O	10.20	810

O_2 added = 0.7592 g/L   C added = 0.0012 g/L

Time = 34 sec sample

Species	Volume %	Correspondence Temp. (^{o}C)
H_2	19.13	727
CO	29.03	727
CH_4	0.044	730
CO_2	35.49	727
H_2O	16.31	727

O_2 added = 1.17 g/L   C added = < 0.0001 g/L

The consistent nature of the preceding analysis may be demonstrated by examining the appropriate fugacity-temperature relationships. The oxygen fugacity-temperature curve for the assemblage Wustite (W) - Iron (I) is shown in Figure C-20. Curves (a) and (b) in this figure indicate the oxygen fugacity in the samples acquired at 25 and 34 sec, respectively. Below ~ 600°C, both curves (a) and (b) pass into the Wustite stability field. Either equilibrium cooling of the gases to room temperature or quenching the gases from their correspondence temperatures along paths Q_{25} or Q_{34} brings the gases into the Wustite stability field. Once there, the gases would oxidize available iron, as hypothesized above, provided kinetic factors were favorable.
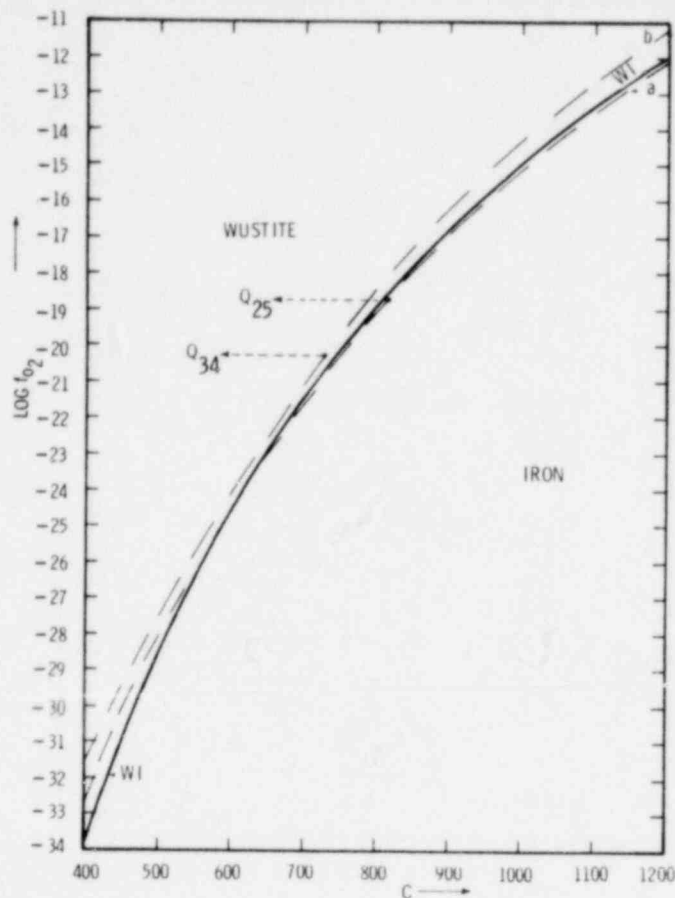
Figure C-20. Oxygen Fugacity vs Temperature for Wustite in Equilibrium with Iron

The carbon fugacity-temperature relationship for graphite in equilibrium with a carbonaceous gas is shown in Figure C-21. Again, curves (a) and (b) denote the fugacity of carbon in the gas samples acquired 25 and 34 sec after the start of the test, respectively. Below ~ $600^{\circ}C$, the curves (a) and (b) pass into the graphite stability field. Consequently, either equilibrium cooling of the gas mixtures or quenching the gas mixtures from their respective correspondence temperatures (paths Q_{25} and Q_{34}) would place the gas samples in a situation where they would have to deposit solid carbon.

The closeness with which the oxygen fugacities of the two gas samples follow the oxygen fugacity over Wustite in equilibrium with iron suggests that the compositional histories of the gas samples may be estimated from the behavior of the W-I oxygen fugacity-temperature curve. Results of such extrapolations to temperatures of 900 to $1700^{\circ}C$ are shown in Table C-XI.
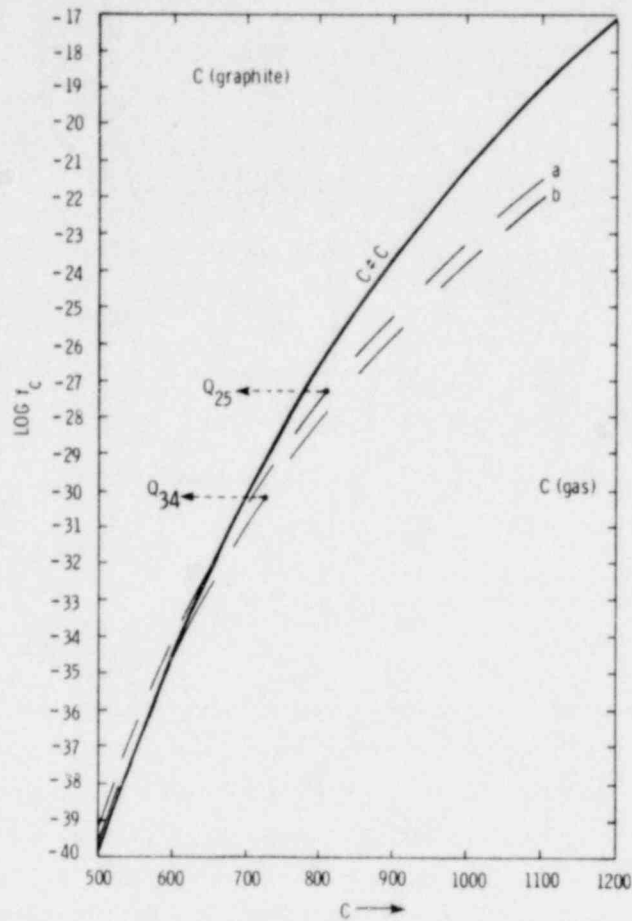
112

Figure C-21. Fugacity of Carbon in a System of Graphite in Equilibrium with a Carbonaceous Gas vs Temperature

TABLE C-XI

Estimated Gas Compositions at Elevated Temperatures

Time = 25 sec sample

Species	Gas Composition in Volume % at the Indicated Temperature				
	900	1100	1300	1500	1700
H_2	22.15	19.79	18.12	16.91	16.01
CO	47.01	49.38	51.05	52.24	53.11
CH_4	0.003	-	-	-	-
CO_2	19.31	16.94	15.27	14.07	13.18
H_2O	11.53	13.90	15.56	16.76	17.64
H	-	-	-	0.01	0.05

1570 204

113

TABLE C-XI (cont)

Time = 34 sec sample

| | Gas Composition in Volume % at the Indicated Temperature | | | | |
Species	900	1100	1300	1500	1700
H_2	15.79	13.11	11.31	10.06	9.14
CO	32.50	35.18	36.98	38.23	39.12
CH_4	-	-	-	-	-
CO_2	32.0	29.32	27.53	26.27	25.37
H_2O	19.70	22.38	24.18	25.43	26.31
H	-	-	0.001	0.009	0.04

4. Conclusions

Testing in this program is far from complete. Nevertheless, a remarkable amount of insight into the qualitative nature of the melt/concrete interactions at prototypic temperatures has been gleaned. It is quite clear that the melt/concrete interaction is a vigorous phenomenon. Concrete is rapidly eroded and substantial volumes of noncondensable gases are released. Concrete is eroded by a melting mechanism. Spallation contributes little to the erosion. Penetration is consequently strongly dependent on the ability of the melt to impart heat to the concrete. Metallic melts, therefore, attack the concrete more aggressively than oxide melts. The rate of concrete erosion is fairly independent of the aggregate used in the concrete, at least insofar as the concrete types used in this study. Gases thermally released from the concrete are reduced as they percolate through the melt, and are readily ignited when oxidizing conditions are again available. These gases are released from the concrete in sufficient volume to obviate the need to consider natural convection in analysis of the melt/concrete system. Density-driven stratification of the melt, however, does seem to be an operative phenomenon in the system and should be considered. Finally, the environment created during the melt/concrete interaction is conducive to the formation of a multicomponent, fine particulate aerosol.

In addition to these irrefutable conclusions, the test data also lead to a wide variety of more or less speculative inferences. These inferences, some of which are listed below, will merit close attention in future, more fully instrumented tests:

a. Steel melts erode concrete at a rate of 1.7 to 2.8 cm/min. This certainly must represent a lower limit since, in these transient tests, prototypic temperatures are not maintained for substantial lengths of time.

b. Radial and vertical penetrations by steel melts are not equal in magnitude.

114

c. The rate of melt penetration is controlled by melting in the cementitious portion of the concrete while overall erosion must be limited eventually by thermodynamic considerations.

d. Forced convection currents in the melt influence the spatial dependence of melt penetration.

e. Gases evolved from the concrete interfere with heat transfer from the melt to the concrete.

f. Heat transfer into the concrete can be explained adequately only when thermally-initiated decomposition reactions are taken into account.

g. Evolved gases, after chemical alteration during their passage up through the melt, remain in thermodynamic equilibrium at temperatures as low as $700^{\circ}C$.

h. CO/CO_2 equilibrium can alter the H_2/H_2O equilibrium in the gas stream toward reduced hydrogen content.

i. Atomic hydrogen makes a significant contribution to the composition of the gases evolved during the melt interaction.

j. Evolved gases make a significant contribution to the upward heat flux from the melt/concrete interaction which in turn is a significant portion of heat loss from the system.

k. Gas equilibrium processes can lead to the formation of aerosols just as gas sparging can.

l. The composition of the evolved gas stream is quite dependent on the heat transfer into the concrete and may deviate substantially from that calculated from the bulk composition of the concrete.

m. Concrete cracking is the result of thermally-induced tensile stresses generated by the presence of the melt.

n. Water in the concrete may migrate both toward and away from the hot zone in the concrete. Water migration from the hot zone is accelerated when crack paths are available.

It may be seen that the physical and chemical processes which merit the most attention in attempts to predict phenomena associated with the melt/concrete interaction are:

a. Heat transfer to the concrete including the effects of melt properties such as viscosity and surface tension, gas films, liquid films, liquid films, and melt velocity.

b. Thermophysical properties of concrete as a function of temperature and heating rate (see Appendix A).

c. Chemical reduction of gases as they pass through the melt with particular attention to carbon dioxide reduction.

d. Aerosol formation mechanisms whether by vaporization, sparging, or chemical transport.

e. Upward heat flux by radiation and mass transport.

Thus far the experimental program has demonstrated the feasibility of monitoring a variety of aspects of the melt/concrete system. Among these are:

a. Thermal response of the concrete

b. Mechanical response of the concrete

c. Aerosol discharges from the melt/concrete system

d. Nature of gases evolved during interaction

e. Rate of melt penetration into the concrete

The success achieved in controlling the phenomena occurring during the melt/concrete interaction suggests that the above list may be expanded to include:

f. Volume rate of gas evolution

g. Upward heat transfer from the system

Comparison of the results obtained in the small-scale tests with those from the large-scale tests shows that the observed phenomena are largely the same. Differences occur in the magnitude and intensities of the phenomena. These differences are almost exclusively attributed to differences in the melt temperature. Obviously melt volume ($\sim$ 30.75 L in the large-scale tests and 0.644 L in the small-scale tests) and the ratio of the surface area of melt in contact with the concrete to the volume of the melt ($\sim$ 0.126 cm^{-1} for the large-scale tests and 0.51 cm^{-1} for the small-scale tests) have an important bearing on the total volume of gas released and the total extent of melt penetration. Melt temperature, however, is the most important parameter for determining the rate of gas evolution, rate of melt penetration, and the formation of aerosols.

116

1570 207

References

1. Light Water Reactor Safety Research Program, Quarterly Report January - March 1976, SAND76-0369, D. A. Dahlgren, Editor, Sandia Laboratories, Albuquerque, NM, Sept 1976.

2. Light Water Reactor Safety Research Program, Quarterly Report April - June 1976, SAND76-0677, D. A. Dahlgren, Editor, Sandia Laboratories, Albuquerque, NM, Feb 1977.

3. Light Water Reactor Safety Research Program, Quarterly Report October - December 1976, SAND77-0944, D. A. Dahlgren, Editor, Sandia Laboratories, Albuquerque, NM, July 1977.

4. Pyrofuze Corp., Division Sigmund Cohen Corp., now defunct.

5. A. A. Anderson, J. Bacteriology 76, 471 (1958).

6. A. A. Anderson, Amer. Ind. Hyg. Assoc. J. 27, 160 (1966).

7. T. Gerlach, Sandia Laboratories, unpublished results.

8. T. Gerlach, Code A-078, reported in '76 Cube Symposium--Code Lists, A. R. Iacoletti, SAND76-0246, Sandia Laboratories, Albuquerque, NM, Oct 1976.

APPENDIX D

RESPONSE OF CONCRETE TO HIGH-HEAT FLUXES

APPENDIX D

RESPONSE OF CONCRETE TO HIGH-HEAT FLUXES

1. Introduction

The objective of this phase of the study is to investigate the response of concrete exposed to a high-heat flux on one surface in the absence of chemical interactions with molten-core materials. Primary emphasis is on determining the dominant surface erosion mechanism (violent spallation versus quiescent melting) including the importance of thermal shock; the surface erosion rates; and the effects on erosion of aggregate material and size, surface heat flux, material removal mechanism, and conduction of heat into the concrete through exposed reinforcing rods. Such information is important for defining the response of concrete to severe thermal attack, for uncoupling the purely thermal phenomena from the overall results of the molten-core/concrete-interaction experiments, and for developing improved phenomenological models suitable for inclusion in a coupled model for predicting molten-core/concrete interactions.

Estimates in the literature of the heat flux from molten-core materials to the concrete floor of the containment building during a reactor meltdown range over two orders of magnitude, between approximately 3 and 300 W/cm^2.[1-4] The present study is concerned only with the higher order of magnitude range, from 30 to 300 W/cm^2. A search of the literature revealed a dearth of information on the response of concrete to such heat fluxes. In the absence of definitive experimental data, the only available information on concrete erosion or penetration rates is based on theoretical models and estimates. Values were found which also span two orders of magnitude: from roughly 8 to 44 cm/hr for decay heat-controlled erosion to from 4.6 to 9.1 m/hr for spallation.[4]

2. Experiments

In order to cover the desired range of heat fluxes and to assess the effects of different material removal mechanisms, experiments were conducted in two Sandia facilities: the 2-MW Plasmajet and the Radiant Heat Facility. The test setups in these facilities are shown in Figures D-1 and D-2, respectively. Parameters varied during the experiments included: aggregate material (limestone and basalt), aggregate size (0.95 and 2.54 cm maximum), and surface heat flux ("cold wall" fluxes of approx. 30, 60, 120, and 280 W/cm^2) and pressure (approx. 0.18, 0.63, and 0.83 atm). A matrix of 31 tests was conducted encompassing the above ranges in the variable parameters (see Table D-I).
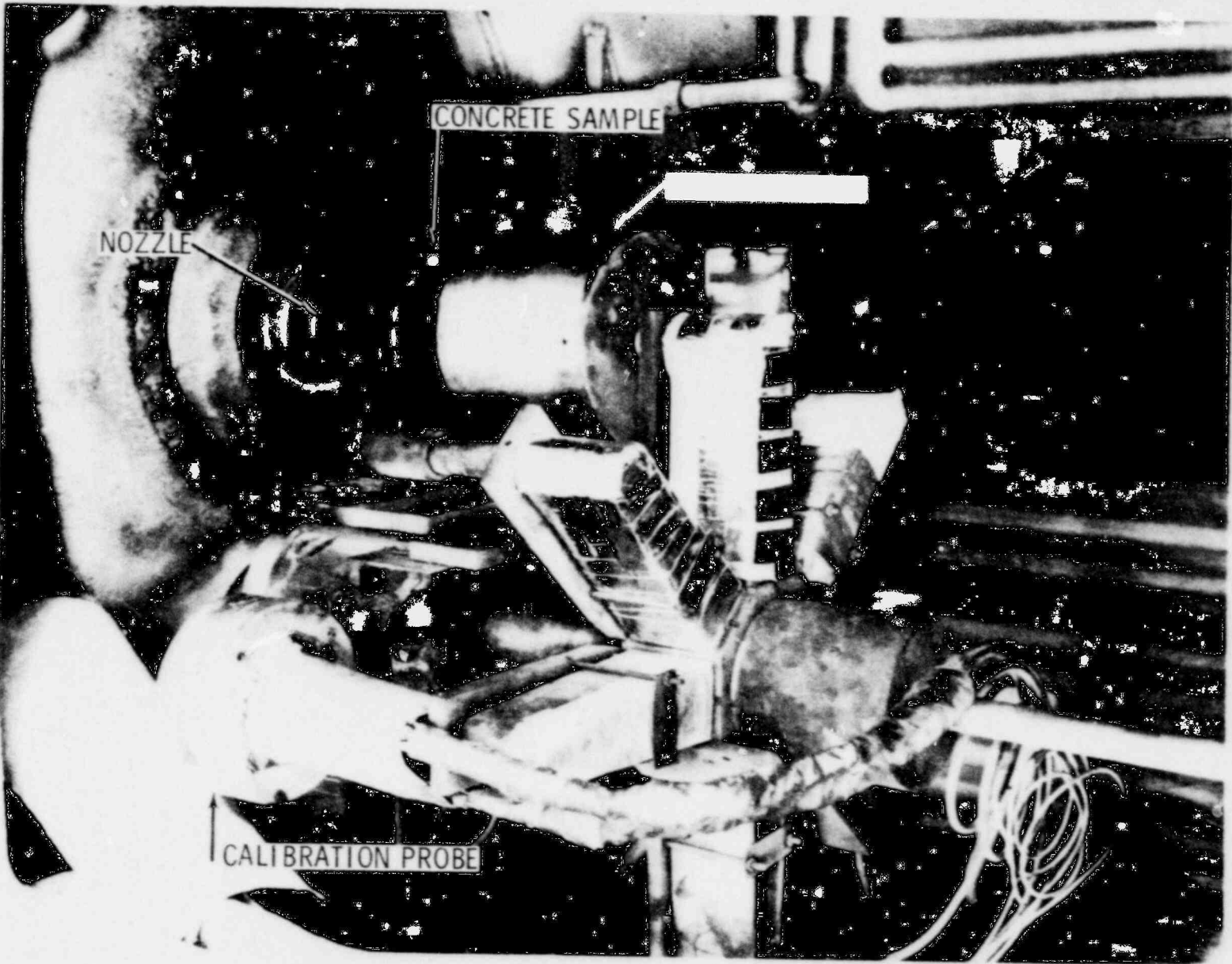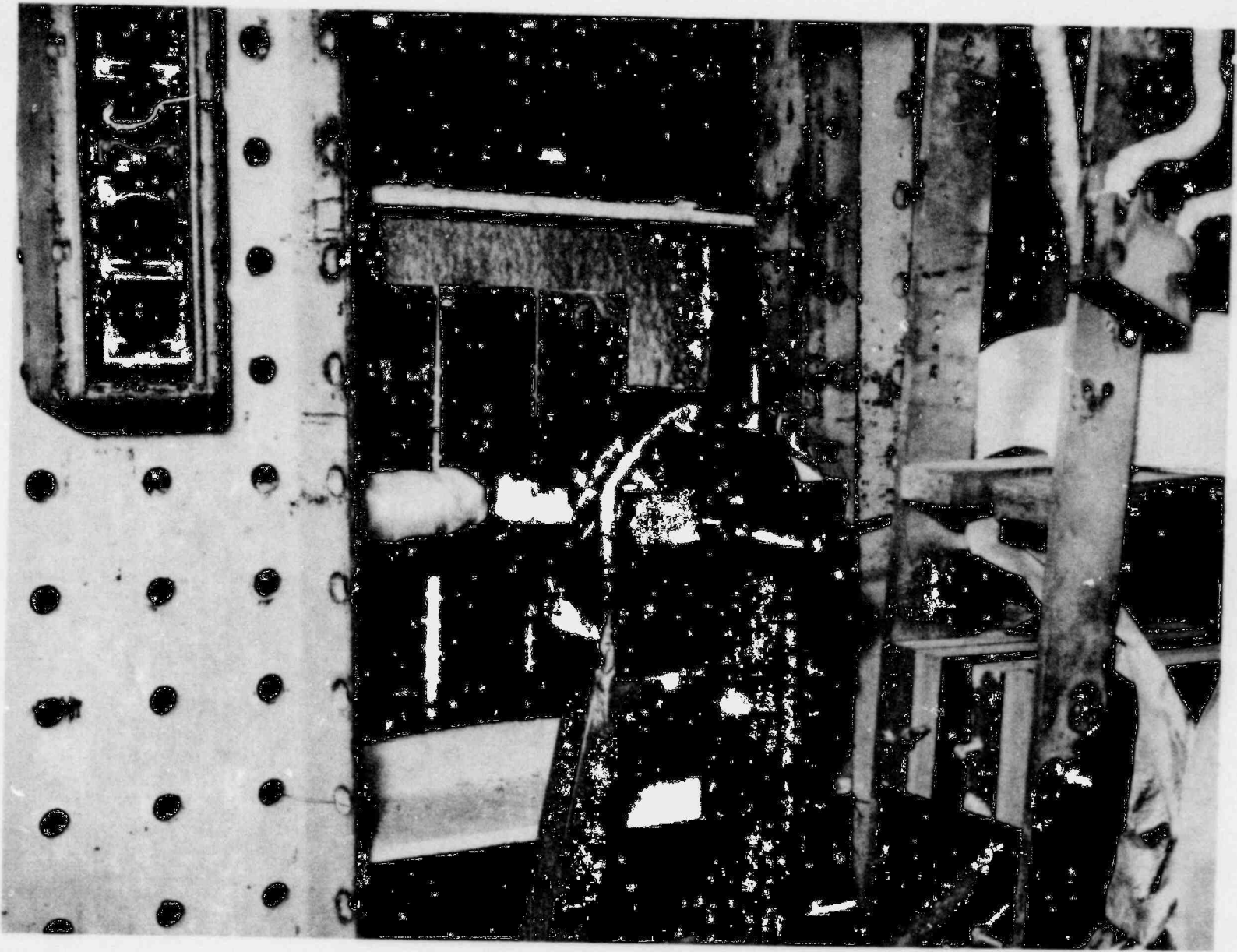
121

Figure D-1. Plasmajet Experimental Setup

Figure D-2. Radiant Heat Experimental Setup with Sample at Test Location

1570 212

123

Aggregate Material and Size	Plasmajet — Nitrogen, P = 0.18, Q = 120, t = 3.5	Plasmajet — Nitrogen, P = 0.18, Q = 280, t = 1.75	Plasmajet — Nitrogen, P = 0.63, Q = 280, t = 1.75	Plasmajet — Air, P = 0.18, Q = 280, t = 1.75	Radiant Heat — Air, P = 0.83, Q = 30, t = 60	Radiant Heat — Air, Q = 60, t = 30	Radiant Heat — Air, Q = 120, t = 10
Limestone: 2.54 cm maximum (L, C)	A / X	A / X	R / X	–	–	–	X X X / R / X
Limestone: 0.95 cm maximum (L, F)	A / X	A R / X	A R / X X	–	–	X	X X
Basalt: 2.54 cm maximum (B, C)	A / X	A / X	–	–	–	–	X X
Basalt: 0.95 cm maximum (B, F)	A / X	A / X	A R / X	X	–	X	X

L - Limestone   X - Test Performed   Nominal Test Conditions:
B - Basalt   A - Acoustic Measurements   P - atm
C - Coarse Aggregate   R - Reinforcing Rod Q - W/cm^2
F - Fine Aggregate   t - min

The concrete test samples consisted of a flat-faced cylinder, approximately 14-1/2 cm in diameter by 8 cm deep, encased in a 15-1/4-cm OD steel liner (Figure D-3). Chromel-alumel thermocouples were embedded in the concrete parallel to the sample centerline at various depths from the exposed surface as shown in Figure D-4. The influence of reinforcing rods was studied by embedding a single 1.27-cm-dia rebar along the centerline of some of the samples with one end flush with the heated surface.

Measurements made during the tests included: surface erosion characteristics, as recorded by regular- and high-speed motion pictures; in-depth temperatures, using the imbedded thermo-couples; surface temperature, by means of an optical pyrometer; initial surface pressure and cold wall heat flux distributions, using a specially designed calibration model; and surface erosion histories, by an acoustic imaging technique.[5] The radiant heat tests were restricted to the first two types of measurements, while all the above measurements were made in the plasmajet tests. In addition, time-integrated spectroscopic measurements were made during the plasmajet experiments in an attempt to identify gaseous concrete constituents evolved during the tests.[6]
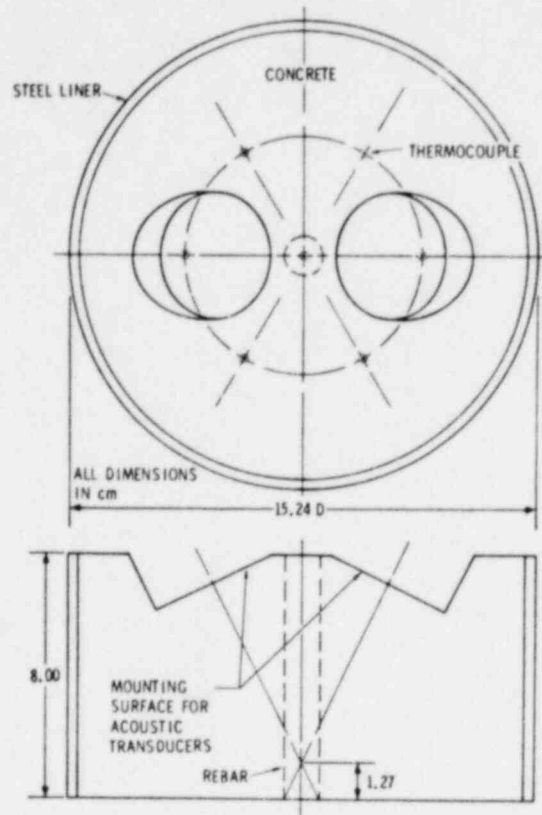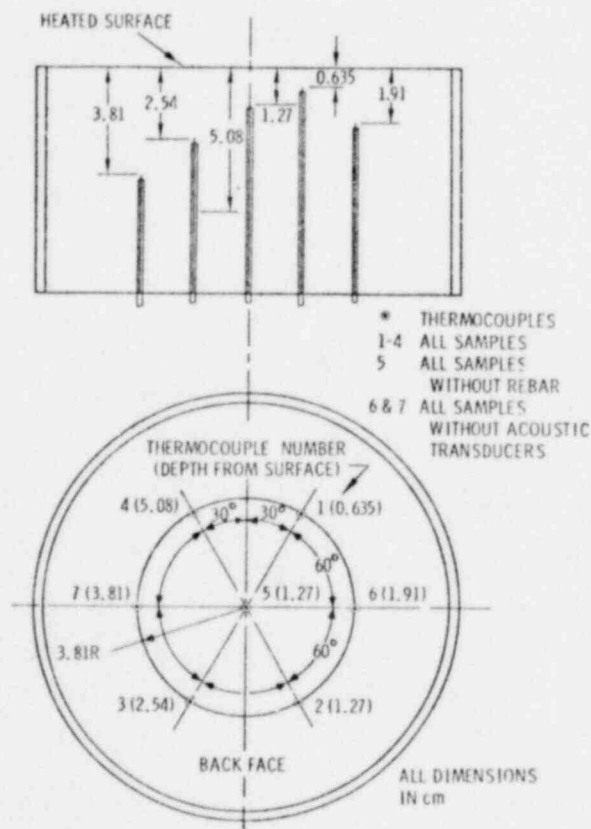
Figure D-3. Sketch of Basic Concrete Test Sample

Figure D-4. Diagram of Thermocouple Locations

Additional information about the experiments and results is available in quarterly progress reports[7-10] and in the two facility test reports[11,12]. Finally, a topical report on the concrete heat-transfer study is currently in preparation.[13]

3. Results and Conclusions

Analysis of the motion pictures and the quantitative results provides the following observations. The dominant erosion mechanism for both calcareous and basaltic concrete appeared to be the melting of the cementitious material in the matrix accompanied by dehydration and decomposition of the underlying concrete and periodic removal of the larger aggregate. The erosion was a quiescent process with negligible spallation. Violent erosion, characterized by the removal of concrete in large chunks and controlled by thermal shock, was not observed.

Following a sudden exposure to high-heat flux, the erosion of both types of concrete became a steady process, with essentially constant erosion rate, within minutes after the initiation of heating. The material removal mechanism differed considerably between the two facilities. In the radiant heat experiments, the melt formed a layer over the exposed vertical surface as it flowed down the surface and off the sample under the action of gravity. In the plasmajet tests, however, the melt was driven out from around the aggregate by the action of the jet and flowed radially outward from the center of the surface. Presented in Figures D-5 and D-6 are representative posttest photographs illustrating the essential features of samples of the two aggregate materials tested in the two different environments at approximately the same level of heating.

Average overall erosion depths determined from posttest micrometer measurements of the eroded surfaces are given in Figure D-7. The corresponding average overall erosion rates computed from these data range from approximately 6 to 70 cm/hr and, as might be expected, increase with increasing heat flux. The general trend with heat flux is illustrated in Figure D-8 where the experimental erosion rates are presented versus estimated net heat fluxes to the melting concrete surfaces. The nature of the increase, as well as the effects of aggregate material and size, appear to depend on the heating environment and the material removal mechanism. The effect of exposed reinforcing rods on the erosion process is negligible. The dashed lines enclosing the data indicate an overall scatter of approximately 20 cm/hr.

Typical in-depth temperature data obtained during the radiant heat tests are presented in Figure D-9. These data were found to collapse into a single curve when plotted against a simple similarity variable: instantaneous thermocouple depth beneath the eroded surface divided by the square root of time. This is illustrated by the results presented in Figure D-10. This similarity of behavior implies that the surface temperature during erosion is constant, while the surface heat flux and in-depth isotherm propagation rates are proportional to the surface erosion rate and the inverse square root of time.
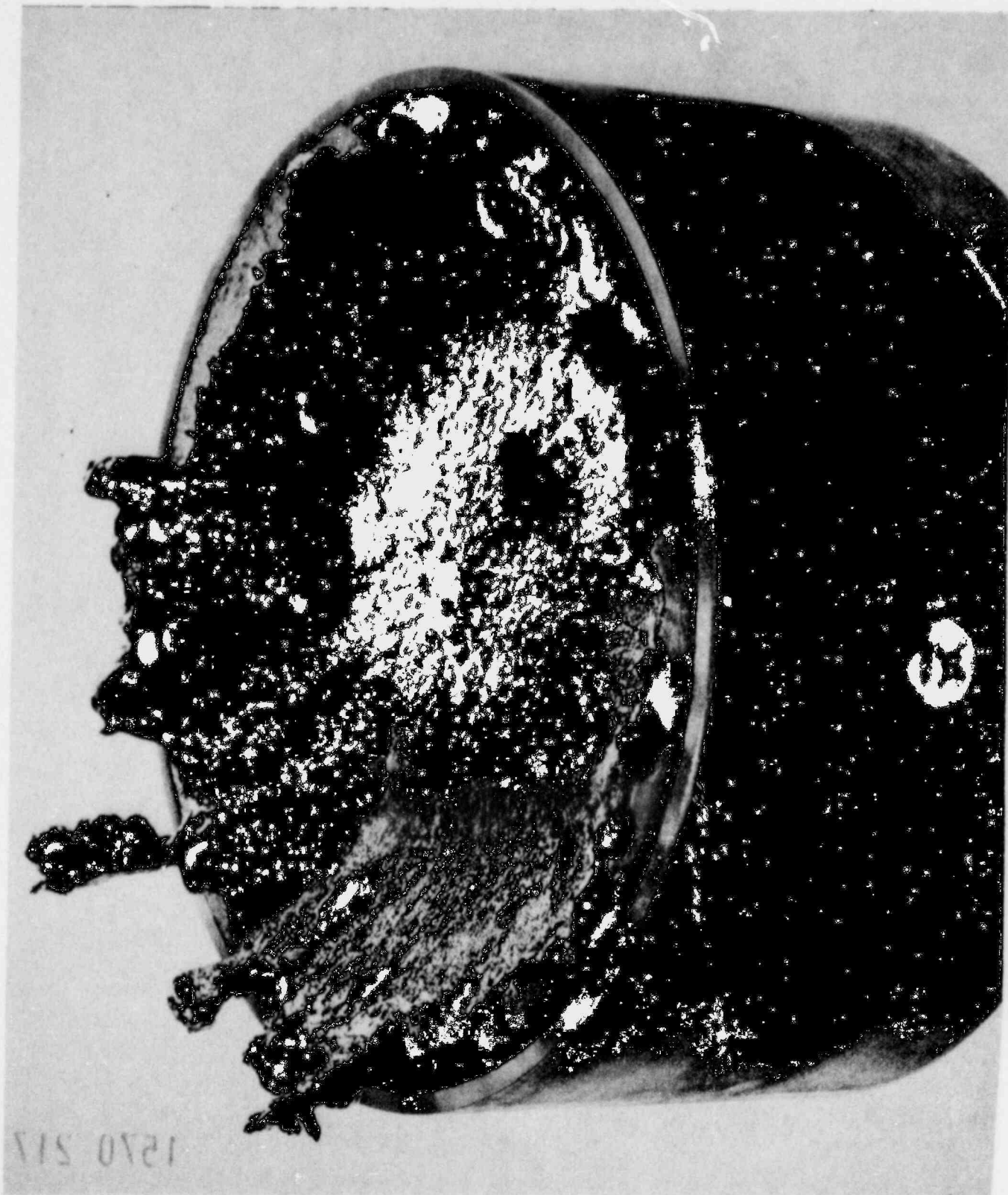
Figure D-5. Eroded Surface of Plasmajet Test Sample P7-28:B, C: 121 W/cm^2; 0.18 atm; 3.80 min.

1570 216

127

Figure D-6. Eroded Surface of Radiant Heat Test Sample RH7-4; L. C; 105 W/cm²; 0.83 atm; 8.56 min.
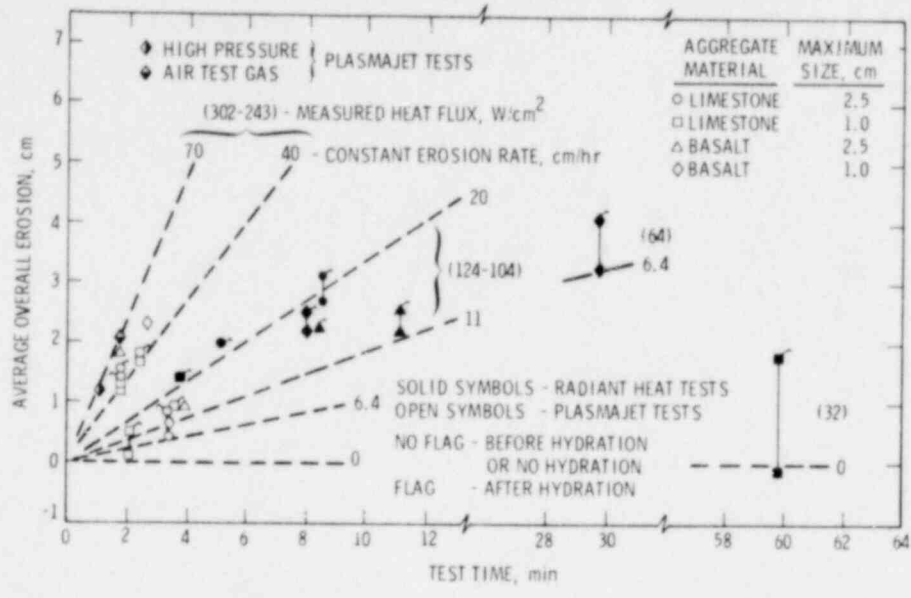
1570 217

128

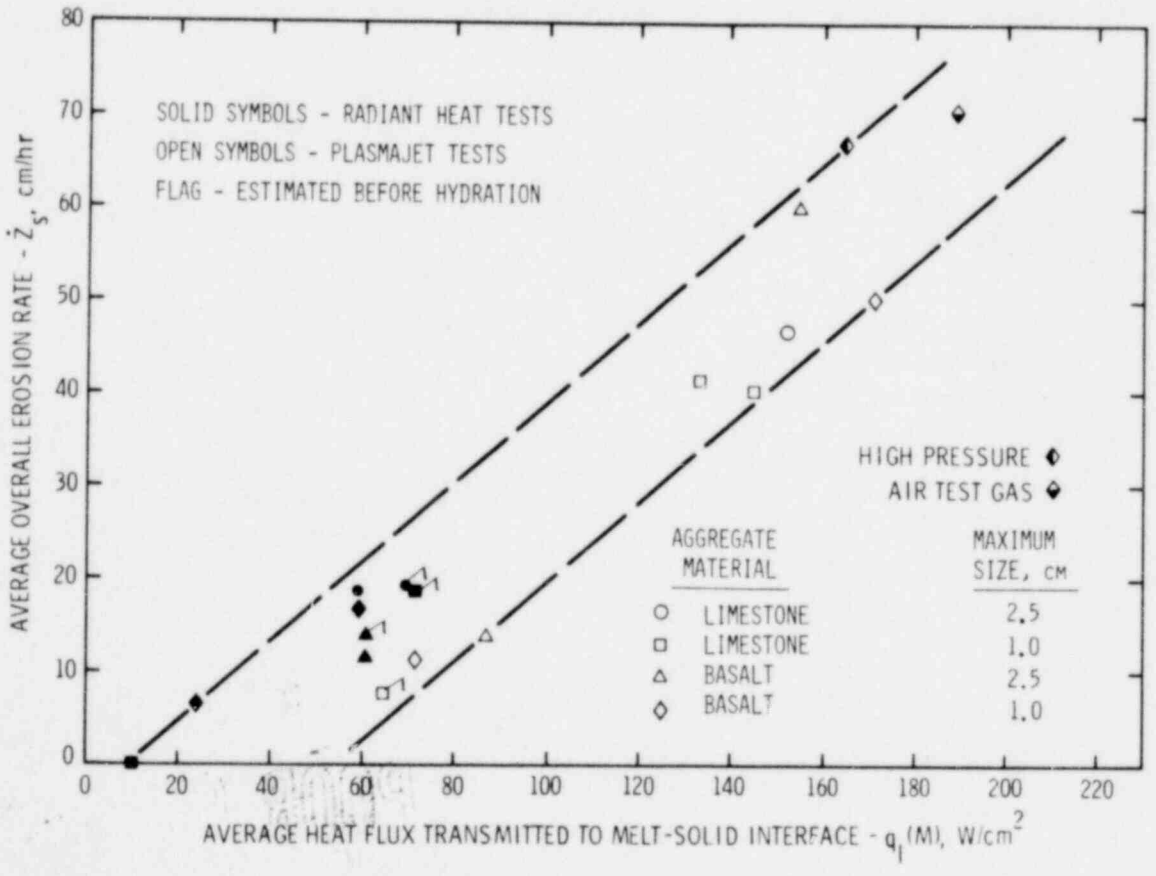Figure D-7. Summary of Average Overall Erosion Results

Figure D-8. Variation of Average Overall Erosion Rates with Net Heat Flux
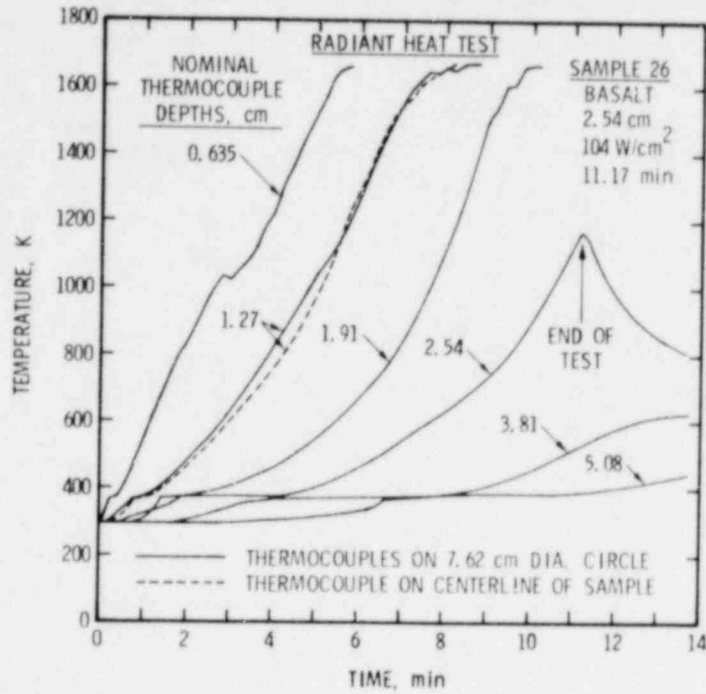
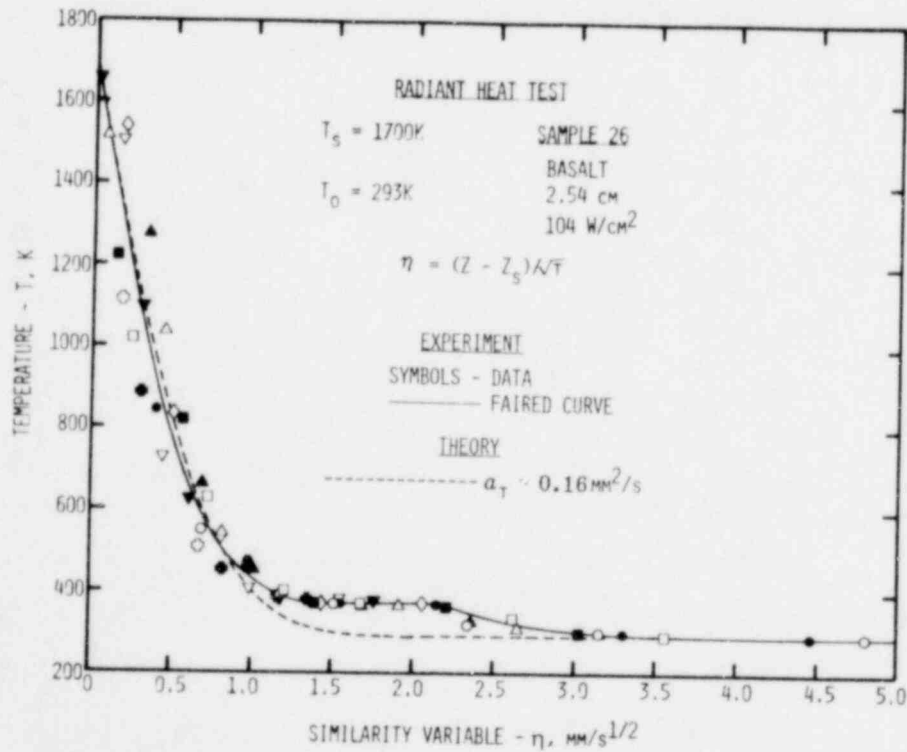Figure D-9. In-Depth Temperature Data for Radiant Heat Test
Sample RH10-26

Figure D-10. Collapsed Temperature Data for Radiant Heat Test
Sample RH10-26

Evaporation of free water within the concrete produces a significant thermal plateau that increases in size with heat flux. Finally, comparison of the experimental variations with the analytical solution for pure conduction in a nonablating, semi-infinite solid suggests that the thermal diffusivity of concrete is quite low at elevated temperatures, ranging from approximately 0.02 to 0.16 mm^2/s for temperatures from roughly 600 to 1700 K.

Estimates of the net heat flux to the melting concrete surface for the present experiments reveal the following. The net heat fluxes, $\dot{q}_\ell(M)$, are significantly lower than the corresponding incident heat fluxes, $\dot{q}_o$ (which would be transmitted to the surface in the absence of ablation and reflected and emitted radiation), ranging from approximately 30 to 80% of $\dot{q}_o$. In general, the emitted radiation, $\dot{q}_E$, is by far the largest contributor to reducing the incident heat flux, varying from approximately 13 to 53% of $\dot{q}_o$. This is true for all but the highest heat flux plasmajet (convective heating) tests of limestone aggregate concrete which resulted in the highest gas generation rates and hence the greatest convective blockage fluxes, 18 to 24% of $\dot{q}_o$. Otherwise, the blockage flux ranges from only about 1 to 9% of $\dot{q}_o$. The energy absorbed by the gas and melt flows contributes the least to reducing the heat flux, varying from 0 to about 2% of $\dot{q}_o$.

The significance of the emitted radiation becomes more apparent when it is considered that an uncertainty in surface temperature results in more than a four-fold uncertainty in $\dot{q}_E$. Thus, over the range of surface temperatures suggested by the experimental results (from roughly 1400 to 1700 K), the value of $\dot{q}_E$ varies by more than a factor of two. The surface temperature, therefore, is the single most important parameter affecting the net surface heat flux.

Finally, the net heat transmitted to the melting surface is partitioned among several energy sinks including the sensible or stored energy and the energies of vaporization, decomposition, and fusion as the concrete heats up, decomposes, and melts. By far the greatest fraction, from approximately 45 to 70% of the net flux, goes into sensible energy. The smallest fraction, roughly 4 to 6%, is absorbed during evaporation of the free water.

The "heat of ablation," H, is a useful parameter for evaluating the performance of concrete as an energy absorber and for extrapolating the concrete behavior to full scale reactor situations. This parameter originated in the aerospace industry and is defined most generally as the incident heat dissipated per unit mass of material removed during a steady-state erosion process.[14] The most suitable form of this parameter for the present application is an "effective heat of ablation," H_{eff}, defined as the quotient of the net heat flux to the molten concrete surface divided by the product of the concrete density and the surface erosion rate:

$$H_{eff} = \frac{\dot{q}_\ell(M)}{\rho_c \left(\frac{dz}{dt}\right)_s} \quad .$$

Using the results presented in Figure D-8 and measured concrete densities, values of H_{eff} were found to range from approximately 4 to 13 MJ/kg with an average value of roughly 6 ± 3 MJ/kg.

To put these values in perspective, they are compared below with heat of ablation values for other materials obtained from the literature.[15-19] Since virtually all ablation data come from the aerospace industry, heats of ablation are available only for those materials considered for heat shield applications. Similar data for more common construction materials do not exist. Furthermore, the heats of ablation that are available are, for the most part, defined in terms of the incident nonablating heat flux, $\dot{q}_o$, and designated Q^*_{eff} i.e.:

$$Q^*_{eff} = \frac{\dot{q}_o}{\rho_c \left(\frac{dz}{dt}\right)_s} .$$

Material	Q^*_{eff} (MJ/kg)
Concrete	5 - 18
Teflon	3 - 5
Phenolic Nylon	3 - 9
Carbon Phenolic	11 - 24
Carbon-Carbon and Graphite	22 - 31

The comparisons are made for the same range of incident heat fluxes as obtained in the experiments. For further comparison, the decomposition energy of concrete is estimated to range from approximately 1.4 to 2.4 MJ/kg for representative limestone and basaltic concretes.[20]

132

References

1. M. H. Fontana and L. F. Parsly, Estimates of Behavior of a Molten Core on Concrete and Attendant Fission Product Release, Draft, Oak Ridge National Laboratory, Oak Ridge, TN, (1973).

2. M. H. Fontana, An Estimate of the Enhancement of Fission Product Release from Molten Fuel by Thermally Induced Internal Circulation, Nucl. Appl. Tech. 9, 364 (1970).

3. G. Jansen and D. D. Stepnewski, Fast Reactor Fuel Interactions with Floor Material after a Hypothetical Core Meltdown, Nucl. Tech. 17, 85 (1973).

4. W. A. Carbiener et al, Physical Processes in Reactor Meltdown Accidents, Appendix VIII to Reactor Safety Study, WASH-1400 (NUREG 75/014), U. S. Nuclear Regulatory Commission (1975).

5. H. J. Sutherl and L. A. Kent, Erosion Rate Measurements Using an Acoustic Technique, Review of Scientific Instruments, 48, 110 (1977).

6. A. J. Mulac and R. A. Hill, Visible Emission Spectra of Ablating Concrete, SAND76-0565, Sandia Laboratories, Albuquerque, NM, Sept 1976.

7. B. M. Butcher, Ed., Light Water Reactor Safety Research Program Quarterly Report, July-September, 1975, SAND75-0632, Sandia Laboratories, Albuquerque, NM, Dec 1975.

8. D. A. Dahlgren, Ed., Light Water Reactor Safety Research Program Quarterly Report, October-December 1975, SAND76-0163, Sandia Laboratories, Albuquerque, NM, April 1976.

9. D. A. Dahlgren, Ed., Light Water Reactor Safety Research Program Quarterly Report, January-March, 1976, SAND76-0369, Sandia Laboratories, Albuquerque, NM, Sept 1976.

10. D. A. Dahlgren, Ed., Light Water Reactor Safety Research Program Quarterly Report, April-June, 1976, SAND76-0677, Sandia Laboratories, Albuquerque, NM, Feb 1977.

11. K. L. Goin, 2-MW Plasmajet Facility Thermal Tests of Concrete, SAND77-0952, Sandia Laboratories, Albuquerque, NM, July 1977.

12. T. Y. Chu, Radiant Heat Evaluation of Concrete - A Study of the Erosion of Concrete Due to Surface Heating, SAND77-0922, Sandia Laboratories, Albuquerque, NM, to be published.

13. J. F. Muir, Response of Concrete Exposed to a High Heat Flux on One Surface, SAND77-1467, Sandia Laboratories, Albuquerque, NM, to be published.

14. ASTM Standard Method of Test for Heat of Ablation, ASTM E 458-72, Nov 1972.

15. A. J. Chapman, An Experimental Investigation of Several Ablation Materials in an Electric-Arc-Heated Air Jet, NASA TN D-1520, Langley Research Center, April 1963.

16. C. L. Arne, Ablative Materials Subject to Combustion and Thermal Radiation Phenomena, Douglas Paper 185, Douglas Missile and Space Systems Division, Jan 1964.

17. G. F. Wright, Jr., Materials Tests in a High-Presssure Hyperthermal Tunnel (High-Pressure Series VI-A), SC-TM-68-44, Sandia Laboratories, Albuquerque, NM, June 1968.

18. G. F. Wright, Jr., Materials Tests in a High-Pressure Hyperthermal Tunnel (High Pressure Series VI-C), SC-TM-69-208, Sandia Laboratories, Albuquerque, NM, Aug 1969.

19. R. E. Sheldahl and G. F. Wright, Jr., Effect of Fabric Orientation on the Ablation Performance of Carbon Phenolic, ISA Preprint No. 76214, presented at the 22nd International Instrumentation Symposium held May 25-27, 1976, San Diego, California.

References (cont)

20. H. S. Levine, Comparative Kinetics of Concrete-Melt Interaction, Internal memo to D. A. Dahlgren, Org 5411, Sandia Laboratories, Albuquerque, NM, Sept 4, 1975.

1570 223

APPENDIX E

A PRELIMINARY MODEL FOR CORE/CONCRETE INTERACTIONS

APPENDIX E

A PRELIMINARY MODEL FOR CORE/CONCRETE INTERACTIONS

1. Background

The Nuclear Regulatory Commission requested Sandia Laboratories to formulate a mathematical model of the melt/concrete interaction. This work has been divided into two phases:

a. A preliminary, approximate model to be based on the earliest experimental results.

b. A more detailed and refined model to be formulated when more data become available.

This appendix describes the first phase of the modeling project. Because a usable model was desired at the earliest possible time, many important and interesting phenomena could only be approximated. The model is therefore not predictive in the sense that fidelity to an actual core meltdown can be confidently expected. However, it is believed that the model can be used to describe qualitatively major phenomena and to determine the relative importance of many effects.

Summary of Experimental Data

Dahlgren[1] has described the experimental progress through March 1976. The phases of the program of most interest to the modeling effort are the deposition of corium type melts onto concrete and the response of concrete to high-heat fluxes. The data from an additional study on the kinetics and stoichiometry of the thermal decomposition of concrete had not been reduced at the time of the modeling and have not yet been integrated into the model.

Significant data from the deposition of steel melts onto concrete were:

a. High gas-blowing rates were observed.

b. There was an immediate, clear-cut separation of metallic and oxide constituents.

c. Only minor spallation was observed ($\sim$ 5 mm).

d. The gases evolved burned readily.

e. The cooling rate of the metal was measured in one test.

f. The cooling rate of the oxide, although less accurately known, was also measured.

1570 225

g. The oxide slag rapidly crusted, but the gases readily broke through the crust.

h. The final recession of the concrete was measured.

i. An initially flat cavity base became rounded.

j. The metal did not wet the concrete, whereas the slag layer did.

Experiments on the response of concrete to high-heat fluxes showed that:

a. The recession rate varied with the incident flux.

b. The recession rate was not strongly dependent on composition.

In addition, simulant experiments[2] showed that pure conduction across a vapor boundary might be a reasonable description of the heat-transfer process.

Insights from Experimental Program

The information obtained from the early phases of the experimental program was necessarily largely qualitative. However, some important insights were gleaned:

a. Gas-induced circulation cells are the primary mechanism for convection.

b. Density-driven separation of immiscible layers is rapid.

c. Each layer is probably nearly isothermal, except for the boundary.

d. The recession rate is not constant.

e. The gases from decomposing concrete (H_2O and CO_2) have ample time to react with iron.

f. The metal does not wet the concrete, whereas the oxide readily does; hence, the heat-transfer coefficient for the oxide/concrete interface should be higher than for the metal.

g. Although the geometry of the cavity is complex, the bottom is generally rounded so that a hemisphere is a reasonable first approximation.

The model has been largely based on these general insights, with the addition of the existing quantitative data.

2. Conceptual Description of Model

A schematic conceptualization of the two layers is shown in Figure E-1. Each layer (metal and oxide) is considered to be well-mixed and isothermal in its interior as long as the layer is molten. Heat transfer from layer to layer takes place across a boundary layer or film whose thickness varies with the violence of mixing. The two main layers are assumed to be in intimate contact with each other, but there can be a vapor layer at the interface with the decomposing concrete. The thickness of the boundary layer can be different for each main layer; however, in each layer, it is uniform around the periphery of the layer. Heat is radiated to the containment, conducted into the concrete, and interchanged between layers.

A hemispherical segment, possibly intersected by a cylinder, is assumed. Figure E-2 shows the possible geometric regimes and also indicates how the geometry can change as the problem advances.
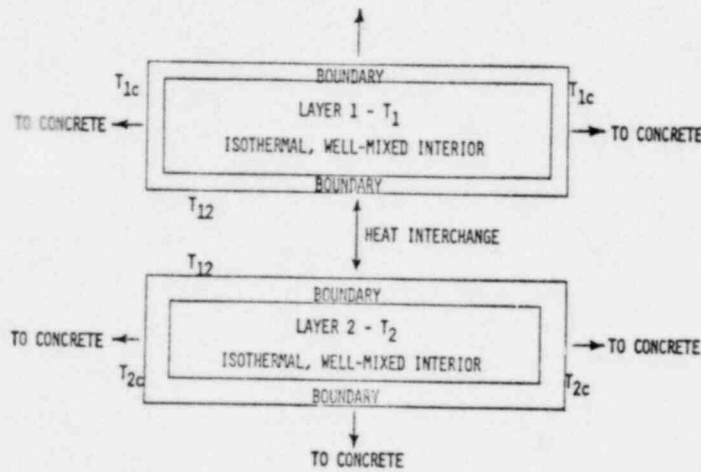

Figure E-1. Schematic Conceptualization

a. HEMISPHERICAL SEGMENT, POSSIBLY INTERSECTED BY CYLINDER

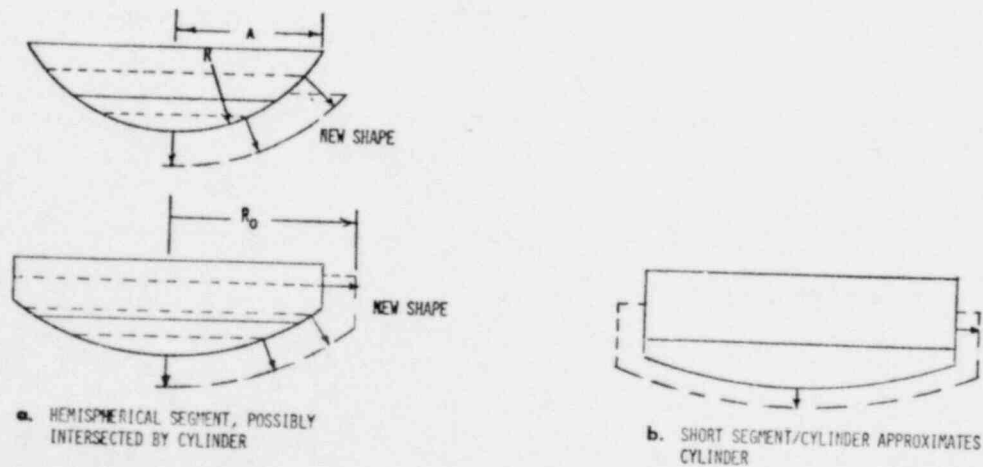b. SHORT SEGMENT/CYLINDER APPROXIMATES CYLINDER

Figure E-2. Geometry

Flows of material are shown in Figure E-3. Material can be interchanged between layers. For example, iron oxides created by reaction of the steam with iron in the metallic part of the melt are assumed to be rapidly incorporated into the oxide layer. Solid or liquid decomposition products are assumed always to go promptly to the appropriate melt layer. However, gaseous products will not pass through the melt if the interface with the concrete is vertical.
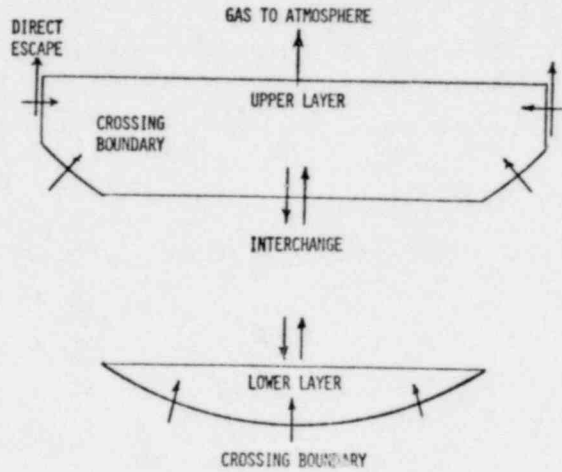

Figure E-3. Flow of Material

Gas-induced circulation cells are shown in Figure E-4. In a normal cell, more gas passes through the outside of the melt and circulation follows the top drawing. However, if the lower layer is hotter than the upper layer, more gas flows through the center and the circulation direction can be reversed. Even if one layer is frozen, as shown in the right-hand sketches, a circulation cell would be expected in the other molten layer. As a general rule, it is to be expected that a circulation cell will be set up if the material is molten and there is appreciable gas flow. The intensity of the circulation (and hence the thickness of the boundary layer) will depend on the rate of gas flow. Other factors influencing the boundary-layer thickness include melt viscosity and gas-flow path; these factors are not dealt with in this simple model.

NORMAL CELLS

BOTTOM LAYER FROZEN

REVERSED CELLS

TOP LAYER FROZEN
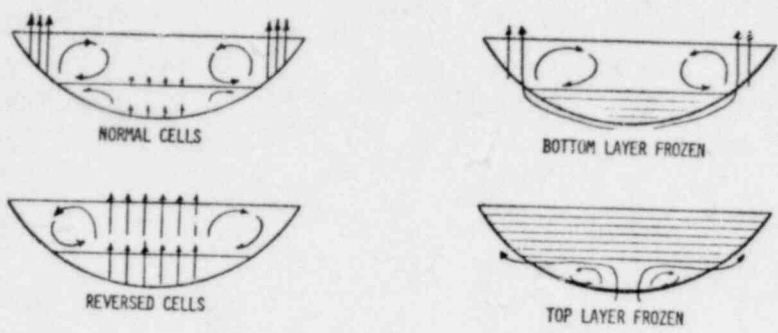
NOTE: For a detailed description of the model, see reference 3.

Figure E-4. Gas-Induced Circulation Cells

3. Experimentally Derived Constants

The key to making this model function reasonably is the determination of the interface heat-transfer coefficients. These coefficients have been chosen to match, as nearly as possible, the metal and oxide cooling curves and total recession in test LSL-1.[4] The boundary layer thicknesses (Figure E-1) have been chosen to allow oxide and metal temperatures to differ by a few hundred degrees when both materials are molten, as has been experimentally observed.

Choice of Interface Coefficients

The interface coefficients have been chosen so that, in a computer simulation of test LSL-1,

a. Metal temperatures drop to the freezing point in 220 sec or less.

b. Slag temperature drops to 1300°C in 160 sec.

c. Recession is approximately 1.5 cm.

An additional consideration is that the heat-transfer coefficient for the oxide should be several times that for the metal because the oxide is in intimate contact with the concrete.

Figure E-5 shows metal temperatures as a function of time for several values of the metal interface coefficient. The oxide coefficient was 0.05 for all trials. Clearly, a value of $0.006 \ W/cm^2/K$ matches the experiment well. At this pair of values (0.006, 0.05), the oxide temperature at 160 sec was 1350°C, the metal was frozen at 210 sec. and the total recession was 1.3 cm at 10 min. After 10 min, the heat transfer to the concrete is so low that ablation essentially ceases.
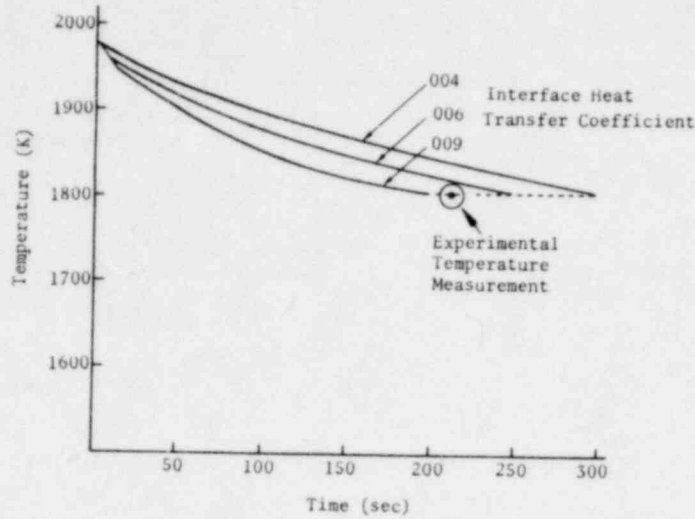
Figure E-5. Simulation of Test - LSL-1

4. Sample Problem Results

The results for a hypothetical PWR core on basalt concrete are shown in Figures E-6, E-7, and E-8. For this problem, it was assumed that the core contacted the concrete one hour after accident initiation, at which time 60% of the fission product decay power had been volatilized and lost from the core.* The remaining decay power was distributed 30% in the oxide and 10% in the metal.
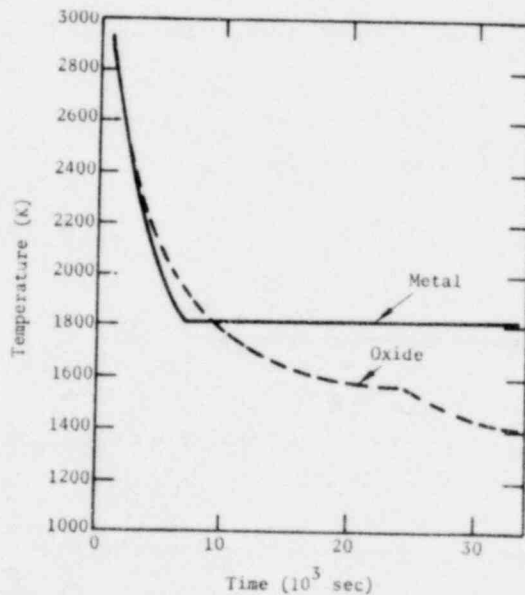

Figure E-6. Metal and Oxide Temperatures, Basalt Concrete

---

*The decay power remaining, and all other parameters of this problem, are intended to be illustrative only and are not intended to represent supposed conditions for any specific core-melt-down accident.
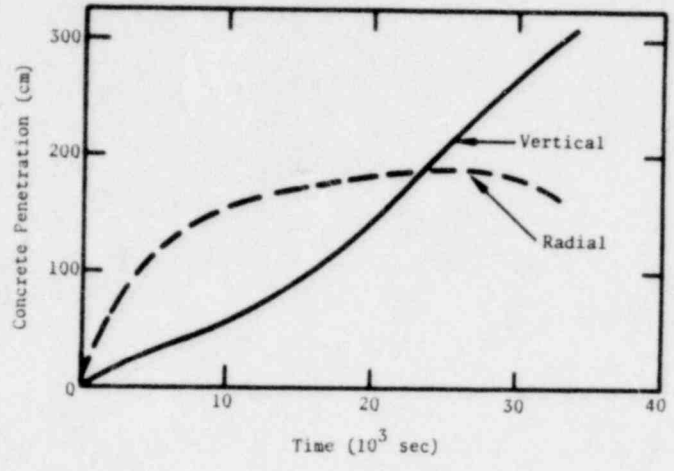
142

Figure E-7. Vertical and Radial Penetration, Basalt Concrete
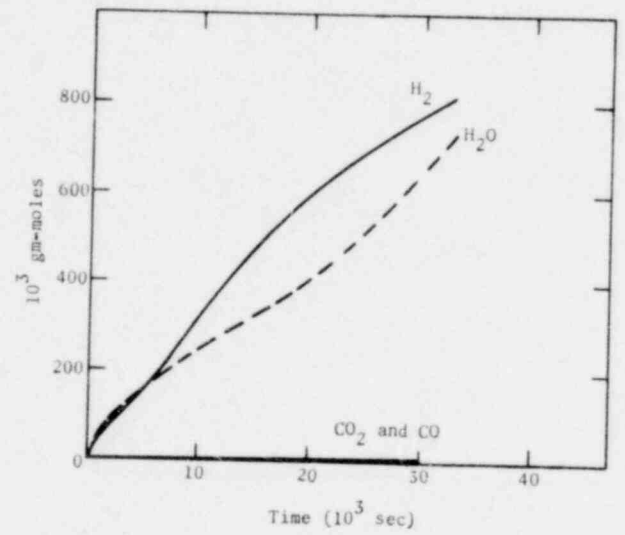

Figure E-8. Gases Added to Atmosphere, Basalt Concrete

Figure E-6 shows metal and oxide temperatures. Figure E-7 shows vertical and radial penetration. Figure E-8 shows gases added to the atmosphere. Figures E-9, E-10, and E-11 show the corresponding results for a limestone concrete. The containment atmosphere could vary from the gas ratios shown, because of later reactions.
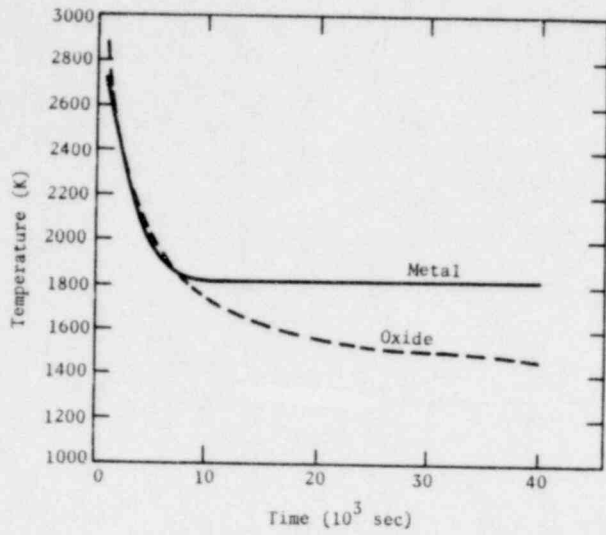
1570 231

Figure E-9. Metal and Oxide Temperatures, Limestone Concrete

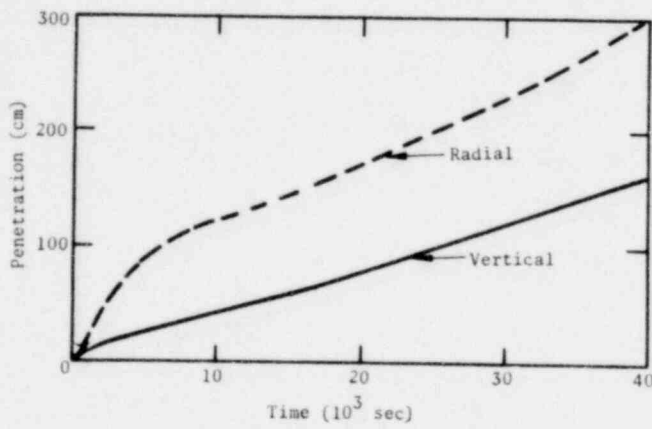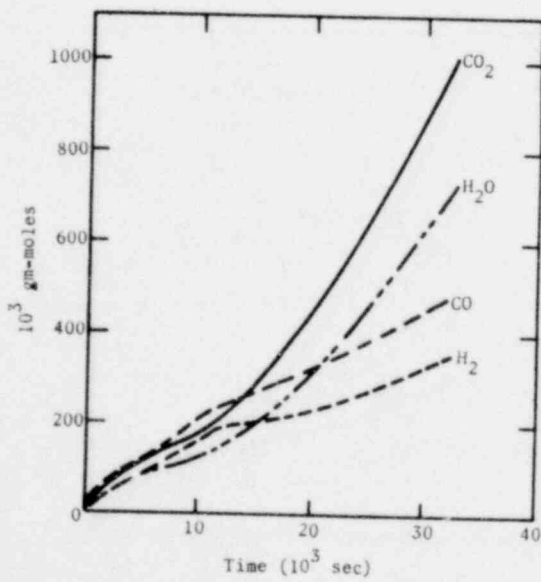Figure E-10. Vertical and Radial Penetration, Limestone Concrete

Figure E-11. Gases Added to Atmosphere, Limestone Concrete

144

5. General Discussion

The model presented is to some extent based on conjecture. It is the author's opinion that the assumptions are reasonable, but certainly there is no proof of completeness or accuracy. It is also believed that little can be done to improve these conditions until more experimental evidence is received. It is heartening to note, however, that the most realistic experiments can be reasonably well simulated.

Because of the number of assumptions and estimates, it should not be supposed that the model can "predict" such critical variables as the time of containment melt-through. The model can best be utilized to determine the general effect of changing parameters on the outcome of the meltdown process. For example, the effect of changing concrete composition on the gases evolved can be estimated, but one should not suppose that the model will accurately predict the time of containment overpressure failure for any specific set of circumstances. The model could be a useful tool in a sensitivity study to explore the importance of various parameters.
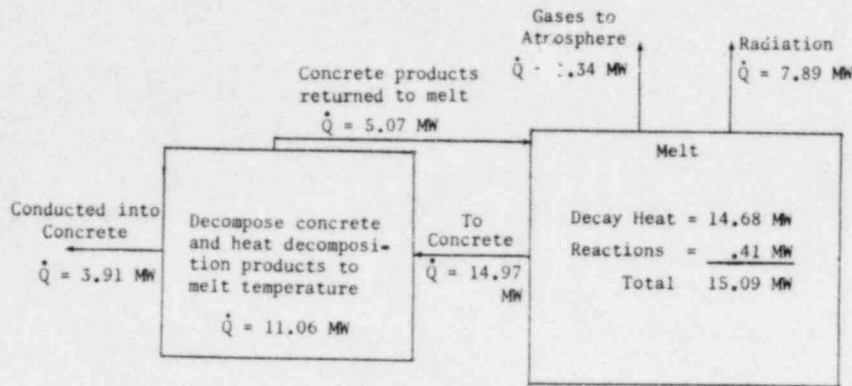
6. Variation of Coefficients

The most important experimentally derived parameters are the interface heat-transfer coefficients. Factors affecting the accuracy of these coefficients are:

a. The accuracy of experimental measurement.

b. The approximate nature of the model.

c. The accuracy with which physical properties are known.

d. Scaling of the small experiments (with times measured in minutes) to a very large core melt (with times measured in hours).

e. Different materials in experiment and core melt.

The net result of these factors is that the interface heat-transfer coefficients cannot be known with any accuracy. Based on intuition and engineering judgement, it is believed that 50% higher interface coefficients are as credible as the nominal values.

7. Accuracy of Computations

The possible accuracy of the computations may be observed by reference to Figure E-12, which shows a heat balance for a typical problem at a time when the melt temperature is approximately the freezing temperature of the metallic layer.

1570 233

Gases to
Atmosphere
$\dot{Q} = 1.34$ MW

Radiation
$\dot{Q} = 7.89$ MW

Concrete products
returned to melt
$\dot{Q} = 5.07$ MW

Conducted into Concrete	Decompose concrete and heat decomposition products to melt temperature	To Concrete	Melt
$\dot{Q} = 3.91$ MW	$\dot{Q} = 11.06$ MW	$\dot{Q} = 14.97$ MW	Decay Heat = 14.68 MW Reactions = .41 MW Total 15.09 MW

Net Rate of Decrease of Sensible Heat = 4.04 MW

Figure E-12. Schematic Heat Balance

It will be noted that relatively minor changes in the radiation component, in the conduction into the concrete, in the concrete decomposition energy, or in the decay heat could significantly affect the rate of change of the sensible heat of the melt. For example, a 10% change in decay heat would make a 36% change in the sensible heat rate. In fact, changes in decay heat, radiation, heat transfer to the concrete, and conduction into the concrete (which are well within the precision with which these quantities can be known) could change the melt from decreasing to increasing temperature. It has been experimentally observed that penetration almost ceases after solidification; this is also shown in the calculations. In the problem shown in Figure E-12, the melt is cooling and will shortly freeze, at which time penetration will be radically slowed. However, the possible parameter changes mentioned above would forestall freezing and even increase the temperature of the melt, thus accelerating the penetration.

It is obvious that computed temperature histories and penetration rates should not be considered indicative of any specific case. The model can, however, be utilized to display a spectrum of possible results.

8. Applicability of the Model

The experiments on which the model is based have been conducted with melts having high metallic content. In these experiments the principal attack on concrete was from the metallic phase. Because the metal layer did not wet the concrete, the attack must be entirely thermal. This is not necessarily the case with the oxide layer. The concrete is wet by the oxide, and the attack could be chemical, diffusive, or simple solution of the concrete by the molten oxide.

Until the method of attack has been more thoroughly explored, the model should be considered of unknown applicability for melts consisting principally of oxides. This may even be so for melts that initially have a reasonable metallic fraction, because the metals are normally burned out by the evolved gases.

1570 234

References

1. D. A. Dahlgren, Light Water Reactor Safety Research Program Quarterly Report, January-March 1976, SAND76-0369 (NUREG-76/6506), Sandia Laboratories, 1976.

2. D. W. Larson and D. O. Lee, Fluid-Mechanic/Thermal Interactions of a Molten Material and a Decomposing Solid, SAND76-0240, Sandia Laboratories, 1976.

3. W. B Murfin, A Preliminary Model for Core/Concrete Interactions, SAND77-0370, Sandia Laboratories, Aug 1975.

4. D. A Powers, Molten Core/Concrete Interactions Project Description, 189 No. A-1019, Sandia Laboratories, 1975.

U. S. Nuclear Regulatory Commission
(244 copies for NRC-7)
Division of Document Control
Distribution Services Branch
7920 Norfolk Avenue
Bethesda, MD 20014

U. S. Nuclear Regulatory Commission
(295 copies for NRC-3)
Division of Document Control
Distribution Services Branch
7920 Norfolk Avenue
Bethesda, MD 20014

Gesellschaft für Kernforschung
75 Karlsruhe
Postfach 3640
Federal Republic of Germany
Attn: W. B. Murfin, PNS/IRB

Dr. M. Fisher
Gesellschaft für Kernforschung
Project Nuclear Safety (PNS)
75 Karlsruhe
Postfach 3640
Federal Republic of Germany

Dr. H. Holleck
Gesellschaft für Kernforschung
PNS/IMF
75 Karlsruhe
Postfach 3640
Federal Republic of Germany

Dr. H. Albrecht
Gesellschaft für Kernforschung
PNS/IRCH
75 Karlsruhe
Postfach 3640
Federal Republic of Germany

Dr. J. P. Hosemann
Gesellschaft für Kernforschung
Project Nuclear Safety
75 Karlsruhe
Postfach 3640
Federal Republic of Germany

Professor F. Mayinger
Lehrstuhl und Institut für
  Verfahrenstechnik
T. U. Hannover
3000 Hannover 1
Callinstr. 15 F
Federal Republic of Germany
Attn: R. Schramm

Gesellschaft für Kernforschung (2)
PNS/RBT
75 Karlsruhe
Postfach 3640
Federal Republic of Germany
Attn: Dr. S. Hagen
      D. Perinic

Dr. Ulrich Müller
Gesellschaft für Kernforschung
Institute für Reukforbauelemente
75 Karlsruhe
Leop ldshafen
Federal Republic of Germany

H. Seipel
BMFT
Federal Ministry for Research
  and Technology
53 Bonn
Federal Republic of Germany

Dr. E. Herkommer
Institute for Reactor Safety
5000 Koln 1
Gloschengasse 2
Federal Repulbic of Germany

Professor Dr. H. Unger
IKE
University of Stuttgart
7 Stuttgart - Vaihingen
Pfaffenwaldring 31
Federal Republic of Germany

G. H. Kinchin
Safety & Reliability Directorate
Wigshaw Lane
Culcheth
NR Warrington, Cheshire
England

Dr. M. Peehs
KWU Abt. Rb. 3
852 Erlangen
Postfach 325
Federal Republic of Germany

Dr. M. Dalle Donne (2)
Kernforschungszentrum Karlsruhe
Institut für Neutronenphysik
  und Reaktortechnik
75 Karlsruhe 1
Postfach 3640
Federal Republic of Germany

Dr. H. Kottowski
c/o - Euratom Ispra
21020 Centro Euratom di Ispra
(Varese) Italy

1570 236

DISTRIBUTION (cont):

Milad Matthias
Dept. of Nuclear Studies and Safety
Ontario Hydro
700 University Ave. (H-16)
Toronto, Ontario
Canada M5G1X6

Dr. M. Reimann
Gesellschaft für Kernforschung
PNS/IRB
75 Karlsruhe
Postfach 3640
Federal Republic of Germany

Division of Reactor Safety Research (52)
Office of Nuclear Regulatory Research
U. S. Nuclear Regulatory Commission
Mail Station: G158
Washington, DC 20555
Attn: M. Silberberg, Chief,
      Experimental Fast Reactor Safety Branch

      R. W. Wright, Experimental Fast
      Reactor Safety Branch

      R. DiSalvo, Fuel Behavior Branch (50)

U. S. Department of Energy (4)
Reactor Safety Research Coordination
Washington, DC 20545
Attn: R. W. Barber, Actg. Director (3)
      T. E. McSpadden, Project Manager

U. S. Department of Energy
Operational Safety Division
Albuquerque Operations Office
P. O. Box 5400
Albuquerque, NM 87115
Attn: J. R. Roeder, Director

Argonne National Laboratory
9700 South Cass Avenue
Argonne, IL 60439
Attn: H. H. Hummel

Oak Ridge National Laboratory
Box Y, Bldg. 9201-3
Oak Ridge, TN 37830
Attn: M. H. Fontana

Brookhaven National Laboratory
Upton, LI, NY 11973
Attn: W. Y. Kato, Head,
      Fast Reactor Safety Division

University of California (2)
Energy and Kinetics Department
5530 Boelter Hall
Los Angeles, CA 90024
Attn: W. E. Kastenberg
      N. Ostrander

EG&G Idaho, Inc.
P. O. Box 1625
Idaho Falls, ID 83401
Attn: A. W. Cronenberg

University of Arizona (2)
Department of Nuclear Engineering
Tucson, AZ 85721
Attn: R. L. Seale
      R. L. Brehm

Westinghouse Hanford Company
P. O. Box 1970
Richland, WA 99352
Attn: L. Munlestein, Manager
      Safety Systems Development

Offshore Power Systems
8000 Arlington Expressway
P. O. Box 8000
Jacksonville, FL 32211
Attn: D. H. Walker, Manager
      Nuclear Safety and Licensing

Ohio State University
Department of Mechanical Engineering
206 W. 18th Avenue
Columbus, OH 43210
Attn: F. A. Kulacki

Michigan State University
Mechanical Engineering Department
East Lansing, MI 48824
Attn: J. V. Beck

400	C. Winter	
1200	L. D. Smith	
	Attn: K. J. Touryar, 1260	
	T. B. Lane, 1280	
1261	D. F. McVey	
	Attn: D. O. Lee, 1261	
1262	H. C. Hardee	
1262	D. W. Larson	
5000	A. Narath	
5160	W. Herrmann	
5167	B. M. Butcher	
	Attn: H. J. Sutherland, 5167	
	J. E. Smaardyk, 5167	
5217	K. L. Goin	
5400	A. W. Snyder	
5410	D. J. McCloskey	
5411	D. A. Dahlgren (10)	
5411	A. S. Benjamin	
5411	R. L. Knight	
5412	J. F. Muir	
5420	J. V. Walker	
5422	R. L. Coats	
5422	H. G. Plein	
5430	R. M. Jefferson	
5450	J. A. Reuscher	

DISTRIBUTION (cont):

5713   B. W. Marshall
       Attn: L. K. Matthews, 5713
5830   M. J. Davis
5831   N. J. Magnani
5831   D. A. Powers (10)
5831   R. A. Sallach
5846   E. K. Beauchamp
9330   A. J. Clark, Jr.
9337   N. R. Keltner
9337   T. Y. Chu
8266   E. A. Aas
3141   C. A. Pepmueller (Actg.) (5)
3151   W. L. Garner (3)
       For DOE/TIC (Unlimited Release)
DOE/TIC (25)
  (R. P. Campbell, 3172-3)

28-607